

CCMR REU 2014



Research Experience for Undergraduates

Support for the REU program is provided by the NSF MRSEC program (DMR-1120296) and the REU Site program (DMR-1063059).

TABLE OF CONTENTS

REU	FACULTY ADVISOR	PG
BOEDEKER, RACHEL	PROFESSOR LARRY BONASSAR	3
CHESNEY, KYLE	PROFESSOR HECTOR ABRUÑA	11
CONTRERAS, JERRY	PROFESSOR LENA KOURKOUTIS	17
CRUZ, ALEXANDRIA	PROFESSOR RICHARD ROBINSON	23
JAHN, DAVID	PROFESSOR BEN WIDOM	29
KIDD, JESSE	PROFESSOR MEREDITH SILBERSTEIN	36
MILOSEVIC, ERIK	PROFESSOR ALAN ZEHNDER	46
NISSEN, ERIN	PROFESSOR PENG CHEN	50
PEREZ, KAITLYN	PROFESSOR FRANK WISE	56
RICE, ERIC	PROFESSOR CARL FRANCK	62
SANCHEZ, CARLOS	PROFESSOR PAUL McEUEEN	67
ZERGER, CALEB	PROFESSOR GREG FUCHS	72

Cell Viability in the Presence of Poly(aspartic acid) and CaCl₂ for Tissue Engineered Meniscal Enteses

Rachel Boedeker¹, Mary Clare McCory², Alexander Boys^{2,3}, Lawrence Bonassar²

¹Biomedical Engineering, University of Delaware, Newark, DE; ²Biomedical Engineering, Cornell University, Ithaca, N.Y.; ³Materials Science and Engineering, Cornell University, Ithaca, N.Y.

Meniscal tears are some of the most common knee injuries, but because partial and total meniscectomy often lead to osteoarthritis (OA)¹, researchers have been exploring tissue-engineered menisci as a solution to this problem. Although the field of tissue engineering has greatly progressed in attempting to create a tissue-engineered meniscus, there has been significantly less research done in investigating tissue-engineered enteses. Meniscal enteses are essential to fixing the meniscus to the tibial plateau, and that proper fixation is paramount to implant success. However, these enteses have a complex structure including a unique mineralization gradient that is difficult to reproduce. Scientific investigations have recently developed a method for producing intrafibrillar mineralization in collagen by using poly(aspartic acid) (pAsp)², but this method has never been tested in the presence of fibrochondrocytes (FCCs). In this paper, we investigate how cells respond to the mineralizing solution known to cause the intrafibrillar mineralization found in native meniscal enteses by exposing FCCs to various concentrations of both pAsp and calcium chloride (CaCl₂). Our results indicate that between levels of 1.5625 and 18.75 mM CaCl₂, cells do not show a negative reaction to the calcium. Similarly, the FCCs did not exhibit a decrease in viability when cultured in solutions containing concentrations of pAsp ranging from 15.75 to 125 µg/mL.

I. Introduction

Each knee has two menisci, a lateral meniscus and a medial meniscus. These menisci are attached to the top of the tibia by enteses, which are about 1 cm long structures composed of a gradient of cartilage to bone, going from about 59 MPa³ to 10.4 GPa⁴. Without these enteses, the meniscus is unable to properly distribute an applied load. In a firmly attached meniscus, when pressure is applied to the joint, the joint load is evenly distributed across the entire surface of the joint. However, when the menisci are not firmly attached and pressure is applied, the menisci extrude from the joint, and the joint load is centered onto a small surface area¹, causing the bones to rub together, which can lead to OA. Because meniscal replacement is often recommended as treatment for severe meniscal injuries¹, and the meniscus is not able to perform satisfactorily without proper attachment, this presents a need for tissue-engineered enteses. The majority of the previous work done in this field has been in an attempt to recreate the CaP-mineralized collagen found in native entese². Researchers were able to easily mineralize the collagen, but the mineralization occurred on the outside of the collagen fibers instead of intrafibrillarly, as is found in native enteses. However, Olstzta et al. (2007) was able to successfully achieve intrafibrillar mineralization by using pAsp. The mechanism by which this occurs is still highly contested⁵. Although intrafibrillar mineralization is now attainable, the process has never been tested with fibrochondrocytes (the cells found in menisci). Consequently,

the purpose of this paper is to study how the mineralizing solution known to cause intrafibrillar mineralization affects cell viability.

II. Methods

Cell Isolation

Fibrochondrocytes were extracted from bovine menisci by cutting the menisci into 2 mm cubes and digesting the tissue for ~18 hours in 0.3% collagenase in Dulbecco's modified Eagle's medium (DMEM) with 5% antibiotics (ABAM). The digested tissue was then filtered through 100 μ m cell strainers. The cells were spun down and washed twice with Dulbecco's Phosphate Buffered Saline (DPBS) + 1% ABAM, counted, and resuspended at the desired concentration.

Collagen Gel Formation

Collagen type I was extracted from Sprague Dawley® rat tails and reconstituted in 0.1% acetic acid at a concentration of 30 mg/mL. A working solution (WS) was made with 2.04 mL of 1x DPBS, 2.5 mL of 10x DPBS, and 0.46 mL of 1N NaOH. Three syringes were filled with each component: one with 0.5 mL of WS, one with 0.5 mL of cells+media (at desired cell concentration), and one with 2 mL of 30 mg/mL collagen. Using a three-way stopcock, the collagen and WS were first combined to neutralize the collagen and attain the correct osmolarity, and then this solution was combined with the cell-media solution and ejected to create a collagen sheet gel at a final concentration of 20 mg/mL.

Culturing the Cells

Twelve samples per experimental group (3 for Day 1 staining, 3 for final day staining, and 6 for biochemical analysis) were taken from the gels with a 4mm biopsy punch and placed in 24-well plates for culture. Each sample was given 2 mL of either FCC media or modified DMEM (mDMEM) media and placed in an incubator for a day. The mDMEM was made from a DMEM powder that did not contain calcium and phosphate. We were then able to add in the desired concentrations of calcium chosen for our experiments. On Day 1, the samples were placed in mineralization solutions containing various concentrations of either CaCl₂ or pAsp. The control samples were simply given new media. The samples were then returned to the incubator for five days. On Day 6, the samples were again placed in 2 mL of plain media (either FCC or mDMEM media) until they were taken for imaging.

Live/Dead Assay

Three samples were taken from each experimental group on both Day 1 and on the final day in culture for live/dead assay. Each sample was placed in a 1.5 mL centrifuge with 500 μ L of 2 μ M ethidium homodimer-1 (EthD-1) in DPBS and 2.5 μ L of 40 μ M Calcein AM in DPBS. Samples were allowed to stain for ~45 minutes and then viewed with a fluorescent-light microscope. Two images (one under green fluorescent light and one under red fluorescent light) were taken at five different areas of each sample.

Image Analysis

Each image was analyzed using the cell counter tool in the ImageJ image-processing program. The number of cells in each of the five images of a sample was averaged for each sample, and then those three values were averaged to give the total average number of cells in each experimental group. The total percentage of both live and dead cells was then found for each experimental group.

III. Results and Discussion

Experiment 1

Samples were tested in 0.7812, 1.5625, 3.125, 6.25, 12.5, 18.75, and 25 mM Ca^{2+} in mDMEM. As seen in Figure 1 below, the samples at very low and very high concentrations of calcium were unable to maintain viability. This is to be expected as cells need a certain amount of calcium to live, but they also should not have too much. The samples that were exposed to the middle range of calcium concentrations maintained viability fairly well, increasing in viability in most cases.

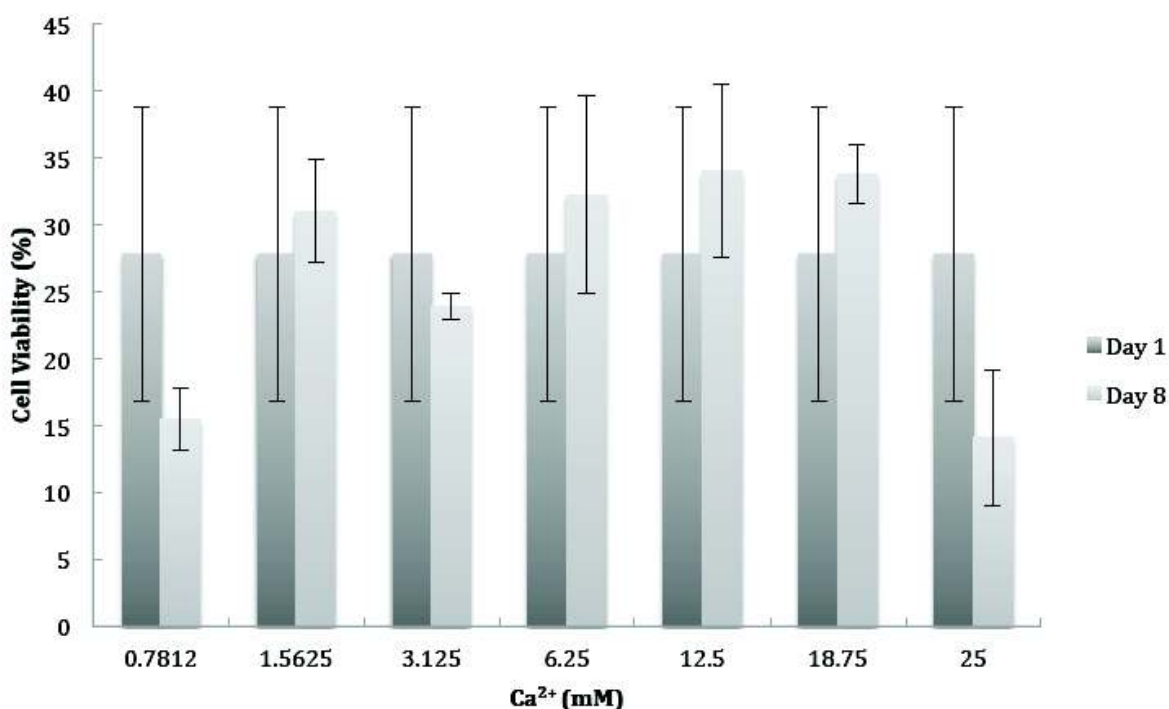


Figure 1: Viability of cells exposed to increasing concentrations of calcium

Additional samples were tested in 0, 15.75, 31.25, 62.5, 93.75, and 125 $\mu\text{g/mL}$ pAsp in mDMEM. As shown in Figure 2 below, the samples in pAsp maintained viability very well, with the exception of the 62.5 $\mu\text{g/mL}$ sample. Since this concentration is the typical concentration used when attempting to produce intrafibrillar mineralization, we decided to perform a second experiment to ensure our findings were accurate.

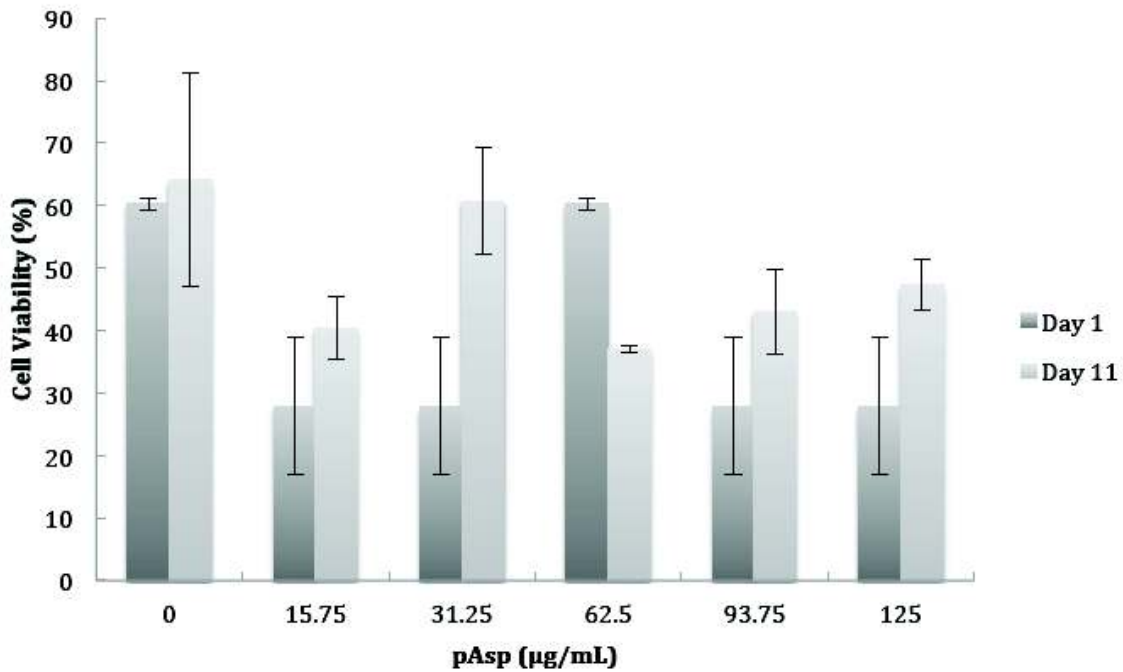
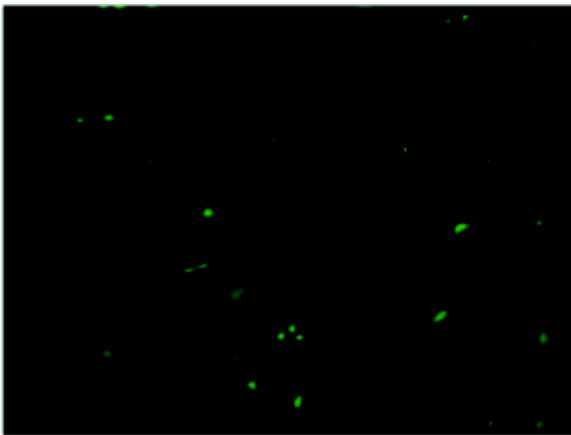


Figure 2: Viability of cells exposed to increasing concentrations of pAsp

Of particular interest in this experiment was the variance in cell morphology. In the samples that were exposed to the pAsp, we observed cell spreading. In some cases, particularly at higher pAsp concentrations, the spreading was extreme. While some cell spreading we observed in a portion of the calcium samples (Figure 3a), it was minimal in comparison to the pAsp samples (Figure 3b).

(a)



(b)

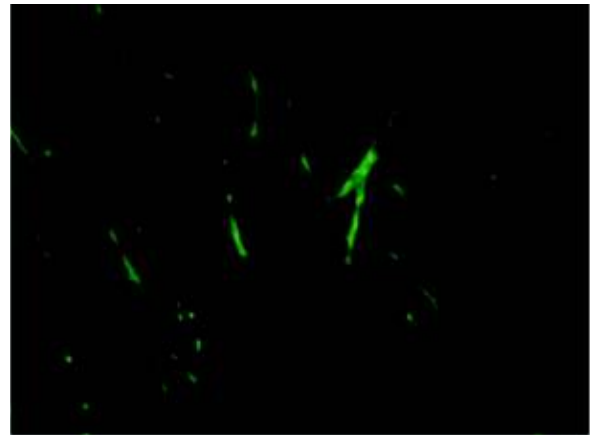


Figure 3: (a) Image of 6.25 mM calcium sample at Day 8 (b) Image of 62.5 µg/mL pAsp sample at Day 11

Experiment 2

In the second experiment performed, we expanded the parameters. Five gels were made with different working solutions: one with DMEM, one with DPBS, one with APBS0, one with APBS2, and one with APBS4 (the three APBS solutions were modified PBS solutions created for this experiment). Each APBS gel was created with a standard 10.906 mM phosphate

concentration (assuming 10 mM for buffering and 0.906 mM found in DMEM) to match the 1.8 mM calcium concentration (found in DMEM) that the mDMEM contains. The APBS2 and APBS4 gels had an additional phosphate concentration that was paired with a corresponding mDMEM calcium concentration that would give the 1 to 1.67 ratio of phosphate to calcium that is in hydroxyapatite (HA) found in bone. The APBS solution phosphate concentrations are given in Table 1.

Table 1: Phosphate concentrations found in the modified PBS gels and the calcium concentrations of the mDMEM with which the gels were paired.

Gel Type	[PO ₄ ³⁻] (mM)	[Ca ²⁺] (mM)
APBS0	10.906	1.8
APBS2	12.906	5.14
APBS4	14.906	8.48

The control groups were the DMEM, DPBS, and APBS0 gels all cultured in FCC DMEM media. The calcium groups were the APBS0, APBS2, and APBS4 gels cultured in mDMEM, some with additional mineralizing solution. The pAsp groups were the DPBS and APBS0 gels, cultured in FCC DMEM media and the mDMEM media respectively, exposed to both 62.5 and 125 µg/mL pAsp. In general, the control groups maintained viability well (Figure 4, underlined in blue). The APBS0 and APBS2 groups in particular had extremely good viability at Day 11. The pAsp groups demonstrated excellent viability (Figure 4, underlined in red), with the exception of the 125 µg/mL pAsp in FCC DMEM media. However, at Day 11, this gel had an abnormal appearance, and it was difficult to see the cells. As a result, the accuracy of this count is somewhat questionable, and therefore could explain this discrepancy.

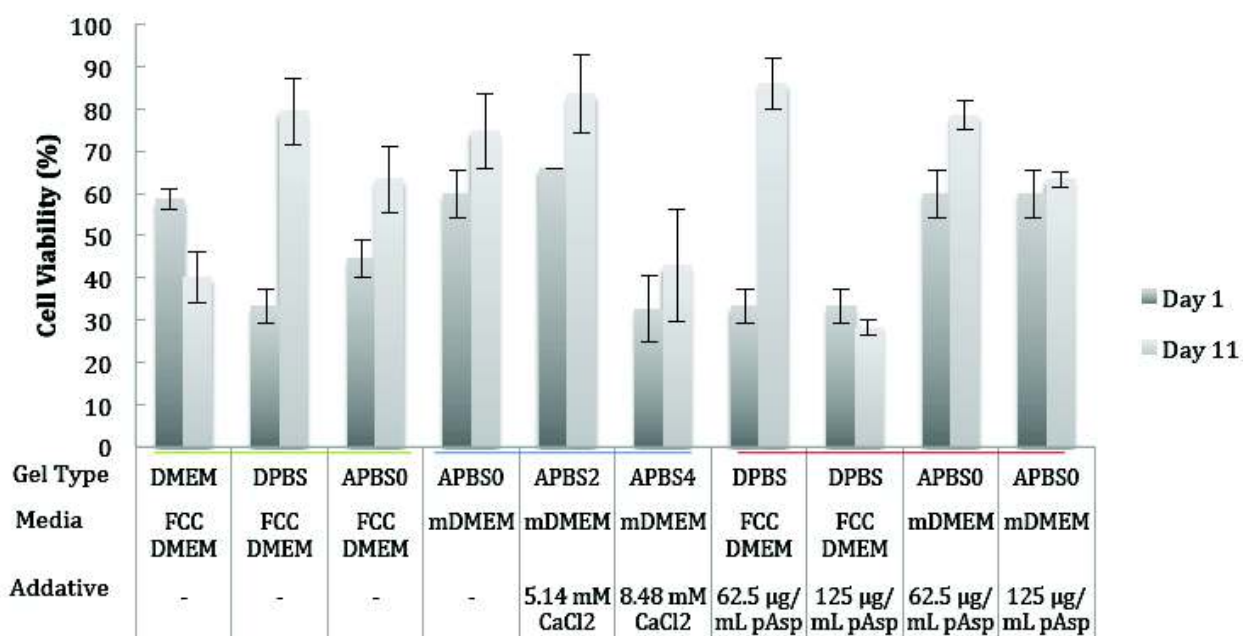


Figure 4: Viability of cells from Experiment 2

As in Experiment 1, we noted that the cells exposed to pAsp underwent extreme cell spreading. While some of the other experimental groups exhibited cell spreading (Figure 5b), it was again the pAsp groups that demonstrated this spreading at an extraordinary level (Figure 5a).

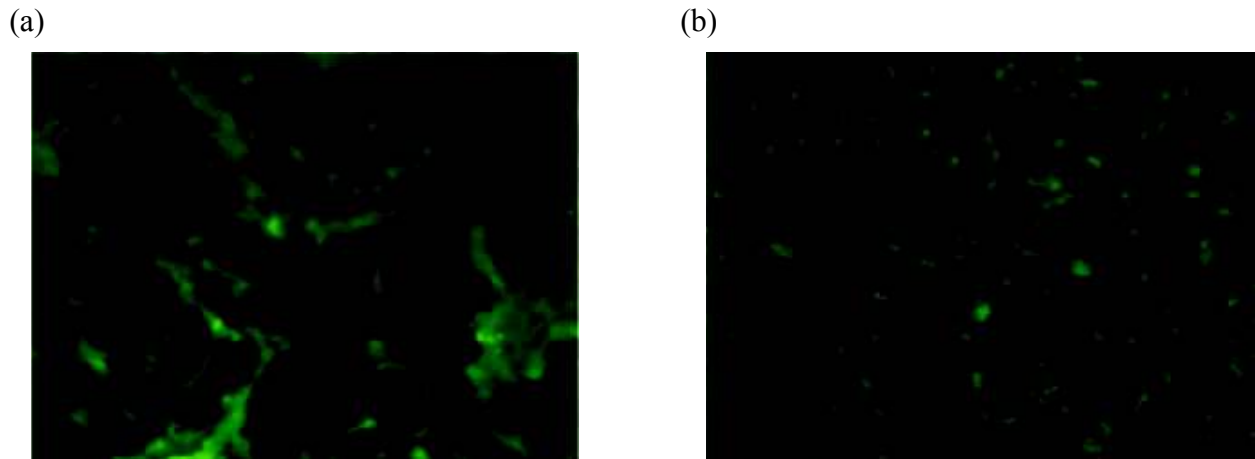


Figure 5: (a) Image of ABS0/62.5 µg/mL pAsp in mDMEM sample at Day 11 (b) Image of PBS2/5.14 mM calcium in mDMEM sample at Day 11

Experiment 3

The third and final experiment was a truncated form of the second with fewer experimental groups over a shorter period of time. DMEM gel samples cultured in FCC DMEM media and APBS0 gel samples cultured in mDMEM media were exposed to 0, 62.5 and 125 µg/mL pAsp. As demonstrated in Figure 6 below, all three samples cultured in FCC DMEM media showed excellent cell viability on Day 5, increasing in each group. The three samples cultured in mDMEM media showed a substantial drop in cell viability from Day 1 to Day 5. However, because the control group exhibited the same drop that the pAsp samples did, we believe that the drop in viability was likely due to a bad batch of mDMEM as opposed to the pAsp.

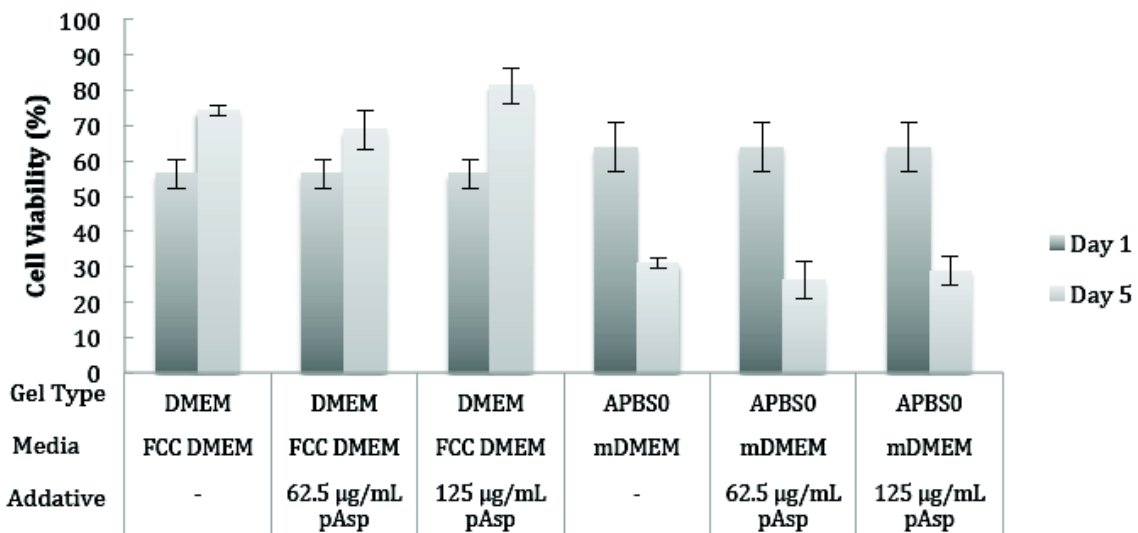


Figure 6: Viability of cells from Experiment 3

Cell elongation was again noted in the samples exposed to pAsp (Figure 7a). The elongation appeared to be less pronounced than in the previous two experiments, likely because the samples were only in the pAsp mineralizing solution for three days instead of the usual five.

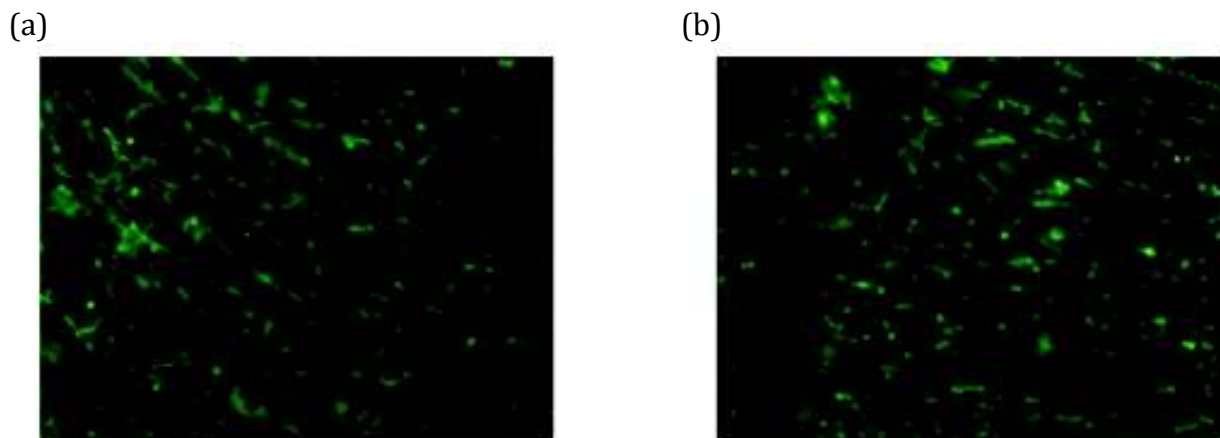


Figure 7: (a) Image of DMEM/62.5 $\mu\text{g}/\text{mL}$ pAsp in FCC DMEM media sample at Day 5 (b) Image of DMEM in FCC DMEM media sample at Day 5

IV. Discussion and Conclusion

Poly(aspartic acid), used for intrafibrillar mineralization, did not cause a decrease in the viability of cells. Moreover, most of the groups that were exposed to pAsp experienced an increase in cell viability. The cells to which pAsp was introduced experienced cell spreading, in some cases to the extreme. While some of the groups that did not come into contact with pAsp showed signs of cell spreading, it was generally minimal compared to the groups that had been exposed to pAsp. This observation led us to believe that the pAsp was either causing, or at least exacerbating, this change in cell morphology. To further explore this interesting phenomenon, our samples should be examined using transmission electron microscopy (TEM). Those images would allow us to see if the cells are elongating along collagen fibers, which would help explain this unusual occurrence. Furthermore, meniscal FCCs should be examined *in vivo* to determine whether these cells experience the same cell spreading that we observed *in vitro*. *In vivo* spreading would indicate that this unexpected cell morphology does not have a negative impact on cell function.

V. Acknowledgments

We would like to thank the NSF MRSEC program (DMR-1120296) and the REU Site program (DMR-1063059) for funding the REU program, along with the Cornell Center for Materials Research.

VI. References

¹ KAROLA MESSNER and JIZONG GAO (1998). The menisci of the knee joint. Anatomical and functional characteristics, and a rationale for clinical treatment. *Journal of Anatomy*, 193, pp 161-178.

² Olszta, M. J., X. G. Cheng, S. S. Jee, R. Kumar, Y. Y. Kim, M. J. Kaufman, E. P. Douglas & L. B. Gower (2007) Bone structure and formation: A new perspective. *Materials Science & Engineering R-Reports*, 58, 77-116.

³ A.A. Oshkour, N.A. Abu Osman, M.M. Davoodi, M. Bayat, Y.H. Yau, and W.A.B. Wan Abas. Knee Joint Stress Analysis in Standing. 5th Kuala Lumpur International Conference on Biomedical Engineering 2011 IFMBE Proceedings. Volume 35, 2011, pp 179-181.

⁴ Rho, J. Y., Ashman, R. B., and Turner, C. H., 1993, "Young's Modulus of Trabecular and Cortical Bone Material: Ultrasonic and Microtensile Measurements," *J. Biomech.*, 26(2), pp. 111-119.

⁵ F. Nudelman, A.J. Lausch, N.A.J.M. Sommerdijk, E.D. Sone. In vitro models of collagen biomineralization. *Journal of Structural Biology*, 183 (2) (2013), pp. 258-269.

Computational and Electrochemical Analysis of Benzidine Derivatives

Kyle Chesney[&], Kenneth Hernández-Burgos⁺, Thanh-Tam Truong⁺, Luxi Shen⁺, and Héctor D. Abruña^{+*}

[&] Department of Chemistry, University of Florida, Gainesville, FL 32611

⁺ Department of Chemistry and Chemical Biology, Baker Laboratory, Cornell University, Ithaca, NY 14853

* Corresponding author

Abstract

We have carried out computational and experimental studies on the effects of introducing functional groups in various sites on N,N,N',N'-tetramethyl-[1,1'-biphenyl]-4,4'-diamine (benzidine) with regards to their application as electrical energy storage materials. Specifically, we performed computational analysis via density functional theory (DFT) methods to determine that a furan derivative had the best combination of stability and high redox potential. The computational and electrochemical analyses, via cyclic voltammetry (CV), confirmed that a dimethyl fluorene variant exhibited 2 reversible redox couples at high potentials. Ongoing and future work will focus on examining the properties of 2 other molecules which have been down-selected via computational studies.

Introduction:

As fossil fuels continue to run out, the race to find alternative methods of energy generation and storage is becoming more of a pertinent issue. Among electrochemical energy storage (EES) technologies, lithium-ion batteries (LIBs) have both the highest gravimetric and volumetric energy densities among secondary batteries and will likely play a pivotal role in our transition to alternative energies.¹ Currently, the cathode is the limiting electrode with respect to the capacity of the cell. Materials suitable for cathodes must be redox active and stable in their charged state so that the material will not breakdown when the battery is cycling. Thus, the goal is to find systems which have both high redox potentials and are stable in a range of oxidation states. The cathodes of LIBs are usually made of phosphates and metal oxides,² such as LiCoO₂, but cobalt has a relatively high cost and the electrodes are prone to degradation and failure when overcharged.³ Organic materials represent a promising alternative.⁴ Organics have become popular due to the abundance of the elements employed (H, C, S, O, and N) – making them inexpensive – as well as the ease with which one can alter their

electronic properties via structural and substituent modifications. Moreover, organic compounds can be easily screened via computational analysis.⁵

Unfortunately, organics suffer low volumetric energy densities and their solubility in electrolyte solutions lowers their cycle lives. A large variety of redox-active organic systems have been studied, including conducting polymers (which have low capacity and solubility), radical compounds (with limited capacity due to exchanging only one electron per formula unit), and organosulfur compounds (which exhibit sluggish kinetics and limited cyclability). A fairly well documented redox active molecule is benzidine. The effects of substitutions on a similar system, 1,4-phenylenediamine, have been previously studied, and shown that substituents can greatly affect the electronic properties of the system.⁶ We decided to study the effects of altering the structure of benzidine.

Computational Methods:

All compounds were optimized via Universal Force Field⁷ (UFF) using the Avogadro 1.0.1 software program⁸. Subsequent

density functional theory (DFT) calculations were performed using Gaussian09.^{9,10,11} The B3LYP exchange-correlation functional was used for further structural optimization and to obtain the minimum energy for each compound.^{12,13} The 6-31+G(d,p) basis set was employed to treat all species. The polarizable continuum model (PCM)^{14,15} was employed using acetonitrile (MeCN) as the solvent as implemented in Gaussian09.

We carried out extensive calculations on a broad range of compounds (see Figure 1). In this plot it can be observed that the molecules under study have a good combination of high redox potential and high capacity, which results in high energy density.

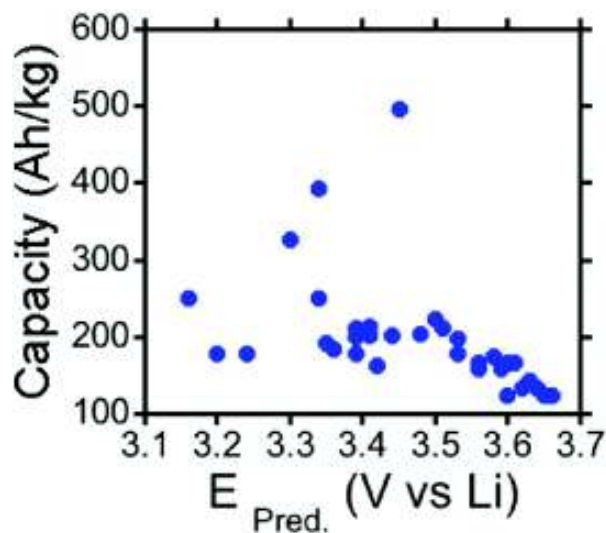


Figure 1: Computational screening plot of all the systems under study.

Nuclear independent chemical shifts (NICS)^{16,17} was used to approximate the stability as a function of aromaticity. We performed nuclear magnetic resonance (NMR) single point calculations on molecules previously optimized in the DFT analysis. We employed the more computationally intensive 6-311+G(d,p), as the molecules were already optimized; solvent parameters remained the same. The NICS method utilizes a ghost (Bq) atom placed 1 angstrom above the geometric center of a ring

to determine the diatropic ring currents, produced by the π electron delocalization. A negative value for a NICS calculation implies a more aromatic – and therefore more stable – system. The opposite is true for positive values (non-aromatic or quinoid system).

The formal potential, E , was calculated as a function of the change in free energy (ΔE), by the following equation,

$$\Delta E = -nFE \quad (1)$$

where n is the number of electrons transferred and F is Faraday's constant. The standard free energy of the reaction is approximated with the adiabatic ionization potential, and the formal potential, E , calculated to vacuum. Corrections due to temperature and the zero point energy were neglected, as the accuracy of 0.05 V is sufficiently large to negate them. For the reference potential of Ag/Ag^+ we shifted the calculated formal potentials, relative to vacuum, by -4.90 V. Figure 2 compares the calculated formal potentials with the experimental cyclic voltammograms. We found an accurate linear correlation between the experimental and calculated values, indicating that our method provides an accurate description of the ground state properties for the neutral and cationic species.

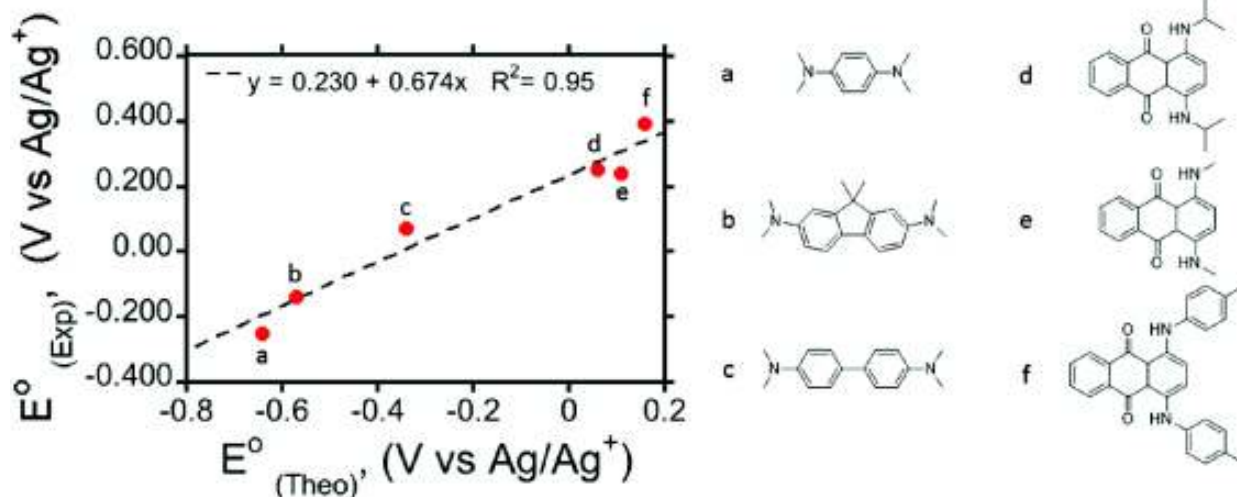


Figure 2: A linear regression plot used to correct for effects not taken into account by computational method, and the molecules used.

Synthetic Methods:

3.8 mg of Pd₂(dba)₃, 6.9 mg of DavePhos, and 132 mg of NaO^tBu were put into a 100 mL schlenk tube under a N₂ atmosphere. The schlenk tube was then put on a line and the head space flushed with nitrogen. We then added 152.1 mg 2,7-dibromo-9,9-dimethyl-9H-fluorene as a solid, after which we bubbled N₂ though 137.7 mg dimethylamine, mixed with 2.5 mL toluene, and added to the schlenk tube. The reaction mixture was heated to 100 °C and left to run for 2.5 days. After cooling to room temperature, the mixture was filtered over celite with CH₂Cl₂ and left to cool in the refrigerator. We purified by a silica gel column chromatography using a plug-type setup with 5% EtOH/Hexanes and rotovapped, then transferred to a vial with CH₂Cl₂, rotovapped, and let sit under vacuum overnight; 125.9 mg (87% yield) of the target molecule shown in scheme 1 were obtained. We proved that we obtained the molecule of interest by using NMR analysis (Figure 3).

¹H NMR (300 MHz, CDCl₃): δ 7.41 (d, 2H), 6.72 (s, 2H), 6.63 (d, 2H), 3.39 (q, 8H), 1.45 (s, 6H), 1.19 (t, 12H)

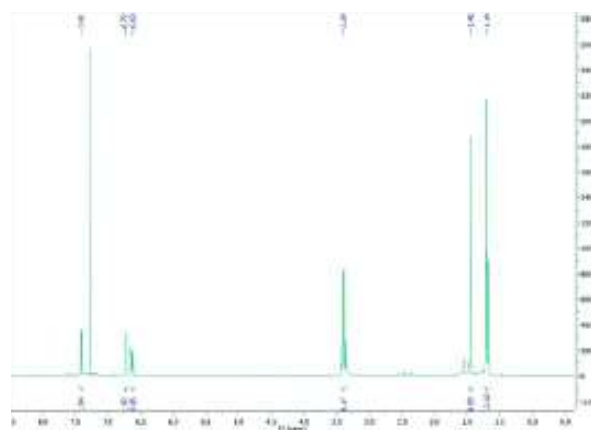
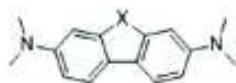


Figure 3: NMR spectrum of our synthesized compound.

Electrochemical Methods:

Cyclic voltammetry (CV) studies were conducted at room temperature using a potentiostat (Epsilon). Measurements were taken in a three-electrode cell using homemade glassy carbon electrodes (GCEs) which were 3mm in diameter, both coil Pt, and mess Pt counter electrodes, and Ag/Ag⁺ (0.05 M AgClO₄ + 0.1 M tetrabutylammonium perchlorate (TBAP)/MeCN) reference electrode. The GCEs were polished with 1.0 um, 0.3 um, 0.05 um alumina powders, mixed with water puri-

Table 1: A table of the theoretical and predicted oxidation potentials with respect to the different heteroatoms.



X	E°_{Theo} (V vs. Ag/Ag ⁺)		E°_{Pred} (V vs. Ag/Ag ⁺)	
	1 st ox.	2 nd ox.	1 st ox.	2 nd ox.
NCH ₃	-0.51	-0.06	-0.11	0.20
S	-0.30	0.14	0.03	0.32
O	-0.32	0.13	0.01	0.32
C(CH ₃) ₂	-0.57	-0.12	-0.15	0.15

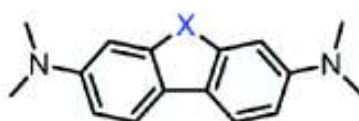
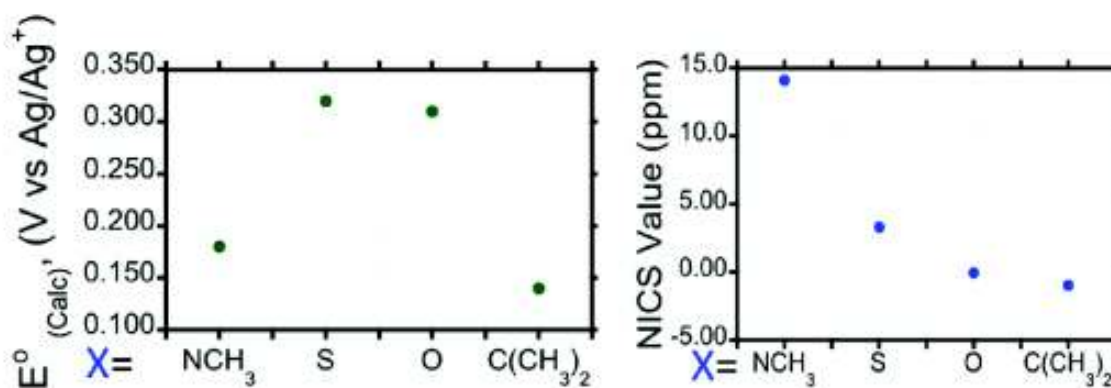
Figure 4: Plot of the 2nd oxidation potential with respect to heteroatom alongside a plot of the NICS value with respect to the heteroatom.

fied with a ThermoScientific Barnstead Nanopure system (18.2 MΩ cm), the GCEs were rinsed with distilled water and acetone, dried before use. The reference electrode was either rinsed with acetone and MeCN, or cleaned with 1:1 HNO₃/H₂O overnight between analyses of different compounds. The experiments were performed in 0.1M TBAP/MeCN solutions and purged using Argon gas before use. The CV experiments were performed at varying scan rates (20, 50, 100, 200, and 500 mV/s)

were weighed out and added to constitute a 1 mM concentration.

Results:

Computational analysis led us to choose to study the heteroatom series for its combination of low molecular weight and high redox potential. Table 1 displays the computed and corrected values (corrected via linear regression plot from Figure 2) for the first and second oxidations of varying substitutions for

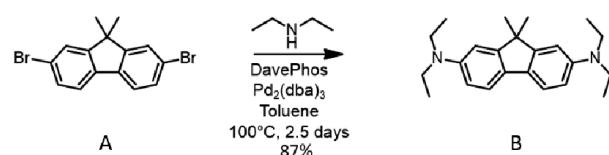


from -0.60 V to 1.00 V vs Ag/Ag⁺. Samples the heteroatom.

The oxidation potentials must be compared to the NICS values, however, as the molecule must be stable throughout its oxidation states for those states to be usable. Figure 4 displays the same values for the 2nd oxidation potentials organized in a graph to more easily compare it to the results of the NICS calculations.

From Figure 4 it is clear that the furan moiety represents the best combination of high redox potential and stability. However, the dimethyl variant had the highest stability, and as such, we decided to synthesize that compound first, we also attempted the synthesis of the non-methylated version, but it failed, which we attribute to the reactivity of the protons on the heteroatom.

The dimethyl compound was synthesized according to scheme 1 and the process detailed in the synthetic methods section.



Scheme 1: Synthesis of N²,N²,N⁷,N⁷-tetraethyl-9,9-dimethyl-9H-fluorene-2,7-diamine.

CV studies showed that compound 1 underwent two reversible one electron oxidations at E⁰ values of -97 mV, and 204 mV ($\Delta E^0 \sim 0.30$ V), Fig. 5B reflects the computationally predicted trend with the oxidation values of compound 1 lying between those of TMPD (Fig. 5A) and benzidine (Fig. 5C). The

$E_{\text{predicted}}$ (V vs. Ag/Ag ⁺)		$E_{\text{experimental}}$ (V vs. Ag/Ag ⁺)	
1 st Ox	2 nd Ox	1 st Ox	2 nd Ox
-0.20	0.27	-0.23	0.30
-0.15	0.15	-0.10	0.20
0.00	0.28	0.05	0.27

lowering of ΔE^0 suggests that the synthesized compound has less isolated oxidation processes, with each the two redox sites affecting the other more than in TMPD ($\Delta E^0 = 0.58$ V), but less so than in benzidine ($\Delta E^0 = 0.18$ V). Furthermore, we observed the experimental values for oxidation potentials were reasonably close to those which we obtained via theoretic

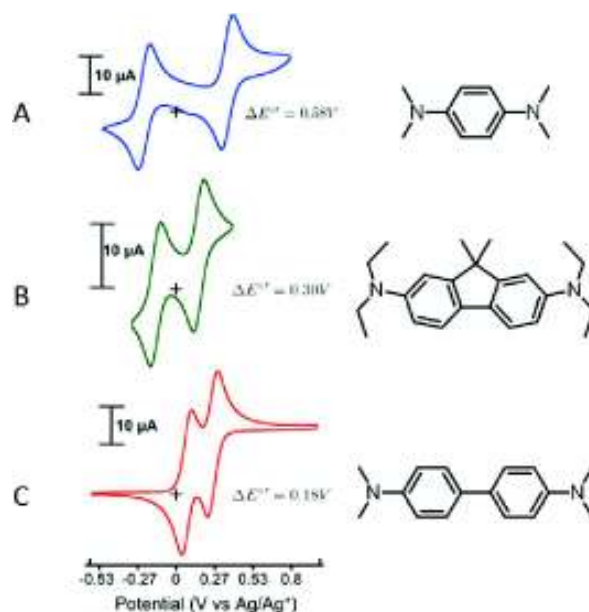


Figure 5: CV diagrams of TMPD (A), the synthesized compound (B), and benzidine (C).

cal studies (Table 2).

Conclusions:

We have predicted the formal potentials of a series of molecules based on a common framework using density-functional calculations and identified a promising family of molecules for electrical energy storage applications, for which we began synthesis and electrochemical characterization. We found that varying the heteroatom greatly affected the redox properties of the molecules while having minimal impact on the overall weight (as compared to the effects of introducing various R-groups in different positions). However these variations also resulted in vastly different stabilities throughout the different oxidation

states, with no clear relations between the redox potential and stability as of yet (i.e. NCH₃ had the second lowest redox potential and the least stability in the dicationic state, while O had the second highest stability as well as the second highest redox potential). Our study

shows that the introduction of a heteroatom into a benzidine-like system, especially oxygen, may produce molecules which hold promise as electrode materials for electrical energy storage applications.

¹ Abruña, H. D., Kiya, Y., & Henderson, J. C. Batteries and electrochemical capacitors. *Phys. Today*, **2008**, 61(12), 43-47.

² J.-M. Tarascon, & M. Armand. Issues and challenges facing rechargeable lithium batteries. *Nature* 414, 359-367.

³ United States Department of Energy Report; Basic Research Needs for Electrical Energy Storage: Report of the Basic Energy Sciences Workshop for Electrical Energy Storage, 2007.

⁴ Song, Z.; Zhou, H. Towards Sustainable and Versatile Energy Storage Devices: An Overview of Organic Electrode Materials. *Energy Environ. Sci.* **2013**, 6, 2280-2301.

⁵ Hernández-Burgos, K., Burkhardt, S. E., Rodríguez-Calero, G. G., Hennig, R. G., & Abruña, H. D.. Theoretical Studies of Carbonyl-Based Organic Molecules for Energy Storage Applications: The Heteroatom and Substituent Effect. *J. Phys. Chem. C*, **2014**, 118(12), 6046-6051.

⁶ Chung, Y. C., & Su, Y. O. Effects of Phenyl-and Methyl-Substituents on p-Phenylenediamine, an Electrochemical and Spectral Study. *Journal of the Chinese Chemical Society*, **2008**, 56(3), 493-503.

⁷ Rappe, A. K.; Casewit, C. J.; Colwell, K. S.; Goddard, W. A., III; Skiff, W. N. UFF, a Full Periodic Table Force Field for Molecular Mechanics and Molecular Dynamics Simulations. *J. Am. Chem. Soc.* **1992**, 114, 10024-10035.

⁸ Hanwell, M. D.; Curtis, D. E.; Lonie, D. C.; Vandermeersch, T.; Zurek, E.; Hutchison, G. R. Avogadro: An Advanced Semantic Chemical Editor, Visualization, and Analysis Platform. *Journal of Cheminformatics* **2012**, 4, 17

⁹ Frisch, M. J.; Trucks, G. W.; Schlegel, H. B.; Scuseria, G. E.; Robb, M. A.; Cheeseman, J. R.; Scalmani, G.; Barone, V.; Mennucci, B.; Petersson, G. A.; et al. Gaussian 09, Revision A.1; Gaussian, Inc.: Wallingford, CT, **2009**.

¹⁰ Kohn, W.; Sham, L. Self-Consistent Equations Including Exchange and Correlation Effects. *Phys. Rev.* **1965**, 140, A1133-A1138

¹¹ Kantchev, E. A. B.; Norsten, T. B.; Tan, M. L. Y.; Ng, J. J. Y.; Sullivan, M. B. Thiophene-Containing Pechmann Dyes and Related Compounds: Synthesis, and Experimental and DFT Characterization. *Chem. – Eur. J.* **2012**, 18, 695-708.

¹² Becke, A. D. A New Mixing of Hartree-Fock and Local Density Functional Theories. *J. Chem. Phys.* **1993**, 98, 5648-5652

¹³ Lee, C.; Yang, W.; Parr, R. G. Development of the Colle-Salvetti Correlation-Energy Formula into a Functional of the Electron Density. *Phys. Rev. B* **1988**, 37, 785-789.

¹⁴ Cossi, M.; Rega, N.; Scalmani, G.; Barone, V. Energies, Structures, and Electronic Properties of Molecules in Solution with the C-PCM Solvation Model. *J. Comput. Chem.* **2003**, 24, 669-681 767.

¹⁵ Barone, V.; Cossi, M. Quantum Calculation of Molecular Energies and Energy Gradients in Solution by a Conductor Solvent Model. *J. Phys. Chem. A* **1998**, 102, 1995-2001.

¹⁶ Schleyer, P. v. R.; Maerker, C.; Dransfeld, A.; Jiao, H.; Hommes, N. J. R. v. E. Nucleus-Independent Chemical Shifts: A Simple and Efficient Aromaticity Probe. *J. Am. Chem. Soc.* **1996**, 118 (26), 6317- 6318.

¹⁷ Chen, Z.; Wannere, C. S.; Corminboeuf, C.; Puchta, R.; Schleyer, P. Nucleus-Independent Chemical Shifts (NICS) as an Aromaticity Criterion. *Chem. Rev.* **2005**, 105 (10), 3842-3888.

Cryo-Scanning Transmission Electron Microscopy of Sectioned Vitreous Gold Nanoparticle Solution

*Jerry Contreras, Michael Zachman, Lena Kourkoutis
Department of Applied Physics
Cornell University, Ithaca, New York 14853, U.S.A
(Dated: August 5, 2014)*

Scanning Transmission Electron Microscopy (STEM) is widely used to study materials down to the atomic scale. The microscope uses electrons in order to image the sample, in contrast to regular microscopes that image using light. Cryo-STEM keeps the temperature of the sample being imaged approximate to the temperature of liquid nitrogen. Under a normal STEM, aqueous samples, such as biological samples, would be evaporated due to the vacuum in the STEM. Using a cryo-STEM allows for biological samples to be frozen into a solid, and thus makes the imaging of these samples possible. In order to be able to image a sample under the microscope, the thickness of the sample must be less than a few hundred nanometers. Creating a sample that meets this restriction is made possible by various methods, one employing the use of a Cryo-Ultramicrotome. Using the micrometer allows for ribbons to be cut from a larger sample, which are then attached to a normal STEM grid, and are ready to be loaded onto the cryo-STEM. Using a cryo-Ultramicrotome, a gold nanoparticle solution was created and imaged using a STEM.

I. Introduction

In the recent decades, the world has become obsessed with the methods for the creation and storage of energy. The main point of interest lies in fuel cell technology, which is currently in its early years of implementation. Although fuel cells have been in use for decades, their maximum potential has yet to be discovered. Fuel cells come in a variety of forms, the most common being an alkaline fuel cell. A significant advantage of alkaline fuel cells (AFCs) over their acidic counterparts is greatly improved oxygen reduction kinetics as well as better fuel oxidation kinetics¹. All

fuel cells are composed of an anode, a cathode, and an electrolyte material. The electrolyte material serves as a catalyst for a reaction to take place between the fuel and oxygen, which will chemically react to form water, causing for electrons to be released. These electrons travel through the fuel cell and stored in batteries as energy. The energy can then be used to power equipment, such as vehicles. Currently, fuel cells are too inefficient and costly to be used commercially. There inefficiency is due to the electrolyte material, which can be either a liquid or polymer membrane, for it requires for fuel to be above certain purity, and is currently too fragile to last for

lengthy periods of time. An alkali fuel cell is able to use hydrogen as its fuel, but the hydrogen would have to have a purity of over 90%. The electrolyte material will only allow for high purity hydrogen to pass through it, anything else will be either kept out, or stuck inside the electrolyte, building up over time until the electrolyte is too clogged to function. Finding methods in which to increase the efficiency of a fuel cell is a hot topic at the moment, due to the high interest in the world for more efficient automobiles. A polymer electrolyte being a material, its properties can be studied through a normal scanning transmission electron microscope with ease, but the chemical reactions occurring inside of it would evaporate. Using a cryo-scanning transmission electron microscope, both the polymer and chemical reactions, can be imaged through the microscope, allowing researchers a better understanding of what occurs during the chemical reaction. In order to be able to image it in an STEM, the polymer must first be plunged frozen, allowing for the chemicals inside of it to be vitreous. A liquid being vitreous refers that it is frozen in a manner that leaves it with a glass like surface, and allows for electrons to pass through it with ease. After it has been plunge frozen, the sample can then be trimmed and cut into ribbons by a cryo-Ultramicrotome, which will keep the sample at low

temperatures. These ribbons can then be mounted on to a STEM grid, and loaded into the cryo-STEM, allowing for the imaging of a polymer electrolyte and its chemical reactions.

II. An Explanation for the Cryo-Ultramicrotome

The microtome used is the Leica EM FC7, capable of temperatures as low as 93 kelvin. A normal microtome remains at room temperature and is only capable of cutting normal polymers. A cryo-Ultramicrotome is able to keep constant low temperatures to allow for aqueous samples to be frozen and cut. These low temperatures are made possible by a liquid nitrogen dewar that is attached to the machine, which continuously pumps liquid nitrogen into the cutting chamber. The cutting chamber in the microtome is reached by an opening located on the top of the machine, and contains the sample holder and knives that are used in the trimming and cutting process. A microtome may sound complex, but the idea behind it is quite simple. In short, the sample holder will oscillate up and down while continuously advancing forward. The knife placed below the sample will then cut pieces from the sample, and stack the pieces over each other, creating a ribbon. While the process seems simple, the real difficulty lies in the preparation of the sample, and determining the

cutting speed used. Operators of the microtome are not only able to control the temperature of the machine, but as well as the speed of the cutting and how much is cut away from the sample after each oscillation. These three factors make the cutting of the sample possible, as well as complex. Some samples may melt if the temperature is not low enough, crack if the speed is too slow or too fast, and shatter if the feed is too large. Because of this, a microtomist may spend several days perfecting the method in which to cut each new sample, since all samples will have different properties.

III. Preparing a sample

The choosing of the sample is also critical; a sample that crystallizes when frozen is almost guaranteed to crack during the trimming process. A vitreous sample, or one that is see through when frozen, is the most ideal.

Achieving a vitreous sample can be done through several methods, but the simplest method would arguably be plunge freezing. Plunge freezing involves the plunging of an aqueous sample into a cryo-liquid, such as liquid nitrogen. The quick plunging of the sample should cause for an immediate freezing of the sample, avoiding the formation of the crystals which form when the sample is frozen slowly. Our own plunge

freezing was done by using a 100nm thick TEM grid, placing a 175microliter drop of sample on to it, and plunge freezing into slushed nitrogen. Slushed nitrogen forms when liquid nitrogen is placed into a vacuum, lowering the temperature of the nitrogen to below its boiling point, causing it to form into a snow like substance. Taking the slushed nitrogen from the vacuum will dissolve the snow, but the liquid nitrogen that remains will not begin to boil until after a few minutes, it is then that you plunge the sample. Transporting the plunged sample to the microtome will require the use of liquid nitrogen, since the sample cannot be exposed to room temperature at any moment.

Once a sample is achieved from the plunging, the sample must then be loaded onto the microtome. This is done through an aluminum pin, which has a flat head and fits into a small hole in the oscillating part of the machine. The flat head is where the sample must be set on with the use of cryoglue. Cryoglue can be created using a mixture of 2:3 Ethanol-Isopropanol². This specific cryoglue is aqueous down to a temperature of 134 kelvin and does not turn solid until 114 kelvin. Precooling the pin with cryoglue on top of it is critical, if the pin were to be room temperature when the sample is placed on top of it, it would melt the sample. The pin should be placed inside the cutting

chamber, along with a large drop of cryoglue, and precooled to a temperature of 134 kelvin. This temperature will allow for the cryoglue to remain aqueous, making it possible for the sample to be placed over the pin. The TEM grid with vitreous sample will need to be embedded in the cryoglue, causing for the sample to be buried in cryoglue. Once this has been achieved, the temperature can be lowered to 114 kelvin, solidifying the cryoglue around the sample.

As the temperature in the chamber nears 114 kelvin, a pair of lab forceps should be precooled close to the temperature of the cutting chamber. The forceps will be used to move the aluminum pin from the precooling position, and into the oscillating sample holder. Once the sample has been placed securely inside the sample holder, and tightened into place, it is ready to undergo trimming.

IV. Trimming of the Sample

Before beginning the trimming process, the knives required must be placed. For trimming, a glass knife is used, which can be created using a Leica Glass Knife Maker and a glass slab. Using the knife maker will produce two knives, but for some samples, four knives may be required. A glass knife is set onto a knife holder and precooled, since a warm knife will melt the sample.

Once has reached the correct temperature, the knife holder must be moved to a position close to the sample, placing it at a point where the sample is only a few hundreds of nanometers away from the knife. Being able to align the sample and knife correctly may take some practice, new operators should expect to ram the knife into the sample a few times. But once the sample is in position, the process turns into an automatic procedure, since the operator will use the microtome controls to trim the sample.

The goal of trimming is to cut the sample, create a small nub in the sample. The nub is a cube with a height of 100 nanometers, along with width and length of the same figure. Due to the sample being buried in the cryoglue, the operator must cut into the cryoglue, pausing only once the sample is uncovered. By burying the sample in cryoglue, the sample is less susceptible to cracking and shattering. Once the sample has been uncovered, the knife may need to be replaced, since the cryoglue that has been trimmed off may have stuck to the edge of the knife. If this is the case, the operator must replace the knife, wait for the knife to cool down, and realign the knife. With the sample exposed, the knife must then be moved, so only the edge of the knife is able to trim the sample. Trimming cautiously, a portion of the sample should be trimmed by

100 nanometers, leaving a section without trimming. The first cut being completed, the knife should be withdrawn, the sample rotated by 90°, and the steps from the first cut repeated. Reaching the third trimming cut, the knife should be positioned as to allow for 100nm of the sample to remain. The fourth trimming cut should do the same as the third, with the exception of the feed being lowered. New operators are likely to commit mistakes in the fourth cut, resulting in the shattering of the already cut sample. If this occurs, the trimming would have to be redone. Completing the fourth cut will leave the operator with a cube sized piece of sample protruding from the overall sample. This cube is optimized for the creation of ribbons, and will allow you to begin the cutting process.

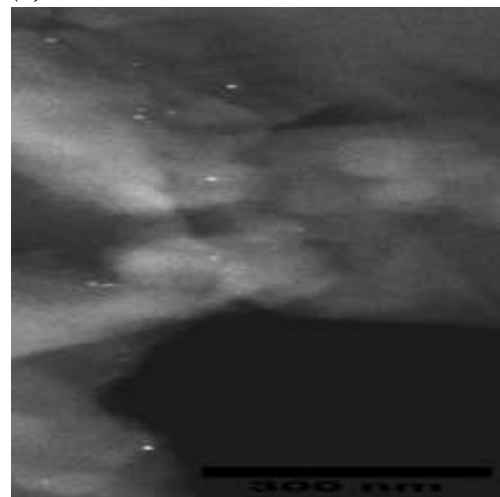
V. Cutting the sample

The cutting process requires the use of a diamond knife, or a very well created glass knife. This process is straightforward, since the operator will align the middle of the knife to the sample, and cut at a feed of 100nm. As the sample is being oscillated, small sections of sample will be cut from the sample, and accumulate into a ribbon on the surface of the knife. The operator must be careful with his selection of speed, since breaking the small piece of sample at this stage will require a

repeat of the trimming. After a long enough ribbon has been created, all that is left to do is to place it onto a 100nm thick copper TEM grid. The moving of the ribbon to the grid can be achieved through different methods, such as using an eyelash to move the ribbon, or placing a TEM at the surface of the knife and allowing the ribbon to be made already on the grid.

Once the ribbon is mounted on the grid, all that is left to do is attach it to the grid. This is necessary due to the method of transportation from the microtome to the cryo-STEM, which will require for the TEM grid to be submerged in liquid nitrogen. If the ribbon is not attached well, the submersion into liquid nitrogen may remove the ribbon from on top of the grid, and the entire process would have to be redone.

(1)



VI. Cryo-STEM

Achieving the attachment of the ribbon onto the grid allows for the

safe transportation of the new sample to the cryo-STEM. Reaching the microscope, the operator will need to employ the use of a special STEM sample holder, which allows for the constant cooling of the sample while it is inside the microscope. Loading the sample onto the microscope, the operator has only to search for an optimal piece of ribbon. Figure 1 shows several 10nm gold nanoparticles, seen as white dots, embedded in an optimal ribbon, demonstrating that the microtome was capable of producing samples suitable for imaging in a STEM.

VII. Conclusion

In our own search for the ribbon, problems arose with the amount of ice that had accumulated over the TEM grid, which covered some of the ribbon, making it impossible to image. But a piece was found and imaged, leading to the conclusion that the cryo-Ultramicrotome was ideal for the imaging of vitreous fluids. In the end, the complete

microtome process required eight hours to be completed, but after further practice, the process can be achieved in a matter of minutes. The lengthy process is due to the exchanging of several glass knives, as well as the amount of time the operator waited for the tools to be pre-cooled. Overall, the microtome requires great patience to use, since they may need to create several samples for imaging.

With this new method of creating fuel cell samples for STEM imaging, it is possible to broaden the study of fuel cell chemical reactions, and find methods in which to optimize fuel cell catalysts.

VIII. Acknowledgements

This research was made possible by a grant from the National Science Foundation, and the Cornell Center for Material Research. Special thanks must be given to John Grazul and Luis Estavez, for their help with the cryo-Ultramicrotome and emotional support.

(1)Robertson. N; (2009) et al, Tunable High Performance Cross-Linked Alkaline Anion Exchange Membranes for Fuel Cell Applications.

(2) Richter. K. (1993). A cryoglue to mount vitreous biological samples for cryoultramicrotomy at 110k.

Effects of Nanoparticle Structure and Solvents in Electrophoretic Deposition for Germanium Nanoparticles

Alexandria Cruz, Joseph Caron, and Richard Robinson*

Department of Material Science and Engineering
Cornell University, Ithaca, New York 14853, U.S.A.

(Dated: August 6, 2013)

Germanium nanoparticles have high potential to be used in lithium ion batteries because germanium has a higher capacity than the graphite used in today's batteries. Germanium nanoparticles can be easily applied to the anodes of batteries with Electrophoretic Deposition (EPD). The EPD process requires only one device and it is easy to scale up making it good for mass production. EPD depends heavily on the solvent and the structure of the nanoparticles used. Changing either of these properties can affect the nanoparticle deposition. Not much research has been done using EPD to apply germanium nanoparticles and we investigate how using different solvent solutions like hexane and chloroform/acetonitrile affect deposition. We also observe how nanoparticles can vary between batches. Finally, we show that nanoparticle's shapes and solvents affect the amount of nanoparticles deposited on copper plates.

I. Introduction

Lithium ion batteries are becoming more ubiquitous as they are utilized in laptops, cell phones and other electronic devices. Commercial lithium ion batteries have graphite anodes which has a theoretical capacity of 372 mAh/g. Compared to graphite, germanium has a higher theoretical capacity of about 1600 mAh/g.^[1,2] The current drawbacks for germanium as an anode material are its high cost and poor cyclability. Repeated cycling causes lattice strain due to the volume change associated with lithium going in and out of the lattice.^[2] When the germanium lattice breaks, layers becomes cracked and loses connectivity. This process is known as pulverization.^[2]

EPD is a method which applies germanium easily to a surface using electric fields.^[3] The process for EPD is simple since it requires only electrodes, organic solvent, and a power source. This simplicity makes

the process cost effective and easy to scale up.^[3] Deposition can also be controlled by changing the voltage, concentration and time that the substrate is exposed to an electric field.^[3]

Another benefit of EPD is that nanoparticles can be applied to the surfaces without any binders or conductive additives, which makes the process simpler and uses less material.^[3] EPD has been previously used in our lab to improve battery performance and we expect similar success for the EPD process for germanium.^[4] By excluding the binder additive we can explore pulverization without confounding variables.

The solvent that EPD takes place in is important to consider because the solvent can transfer charges to the nanoparticles which affects their electronic mobility and the homogeneity of nanoparticle solution. Not much research has been done to find out how to apply consistent layers of germanium

nanoparticles or how germanium behaves in different solvents for EPD.

The solvents that were tested are 1) hexane and 2) 8:1 ratio of chloroform:acetonitrile. Hexane is a non-polar solvent which should allow germanium to express inherent positive charge. In contrast chloroform/ acetonitrile are polar solvents and their polarity would affect whether germanium is deposited on the cathode or anode.

II. Experimental

a. Preparation of nanoparticles

Nanoparticles were prepared by the heat up method presented by Vaughn et al.^[5]

Oleylamine and oleic acid were degassed with nitrogen. In the nitrogen glove box, 0.060g of GeI₄ was added to a 50mL 3-neck flask. In the fume hood 10mL of oleylamine and 0.75 mL of oleic acid were added to the flask and the solution was sonicated to dissolution. 1mL of HMDS was then added to the solution. The 3-neck flask was set up with a condenser, thermometer and a rubber septum. The flask was heated to 278°C at a rate of 2°C/ min while stirring. The solution was kept at 278°C until a dark brown/ red was observed. The solution was then aged for 20 minutes and later cooled to room temperature. The resulting nanoparticle solution was washed in ethanol and hexane twice.

b. Preparation of EPD

Each of the bare copper plates is rinsed in acetone and then hexane. Then, the plates are weighed 20 times and averaged.

The set up for EPD is shown in Figure 1.

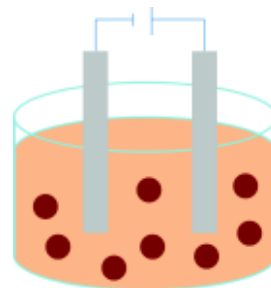


Figure 1: EPD set up. Two electrodes connected to a power source submerged in a germanium nanoparticle solution.

The two stainless steel electrodes are attached to a voltage source. Copper collector plates are attached to the substrate with a small square of a tape. The two electrodes are separated by 2 cm with the copper plates facing each other. The electrodes are then submerged in the solution.

The EPD solution is germanium nanoparticles in a solvent of either 9mL of hexane or 8mL chloroform/ 1mL acetonitrile solution. Before being added to the solvent, the germanium nanoparticles are dissolved in hexane to a concentration of 5mg/mL and either 0.1mL or 0.2 mL of the germanium solution was added to the EPD solution.

A DC voltage of 600 volts was applied to the electrodes for 12 minutes. After 12 minutes, the substrates were removed from the solution and the voltage source was turned off to avoid the solvent accidentally damaging the EPD coating. The backside of the copper plate was cleaned with a cotton swab dipped in hexane and dried with a kimtech wipe to remove any tape residue from the EPD process.

Table 1: Average deposition in chloroform and acetonitrile with 0.5 mg of Ge		
	Cathode	Anode
3.35a	-.120mg	.0796mg
3.35b	-	.0149mg
3.35b +wash	-	.0315mg

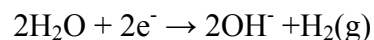
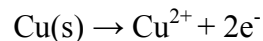
Table 2: Average deposition in hexane on the cathode		
	0.5mg Ge	1.0mg Ge
3.34a	-	.0770mg
3.35a	.0116mg	.0178mg
3.35b	.0848mg	.450mg
3.35b + wash	.0095mg	-

III. Results

a. Comparison of hexane and acetonitrile/chloroform

In hexane, the nanoparticles go to the cathode. Thus, the amounts deposited on the anode would be nearly zero and are not reported in Tables 1 or 2.

When the solvent was chloroform/acetonitrile solution, the nanoparticles favored the anode. For chloroform/acetonitrile solution, when a plate was placed on the cathode, there would always be a reduction in the plates mass instead of increase. This happens because of a redox reaction between the copper and the water in the solution where copper gets oxidized and water becomes reduced.



Despite the solution being chloroform/acetonitrile, there are normally small traces of water in the solution. This redox reaction does not happen in hexane, because hexane does not have any free electrons to conduct the charge required to sustain the redox reaction.

c. Comparison of concentrations

Theoretically, deposition follows Hamaker's equation^[5]

$$Y = \sigma C \int \int \frac{dV}{dn} ds dt$$

Where C is the nanoparticle concentration, dV/dn is the electric field, dt is the deposition time, ds is the surface area, and s is a constant.^[5] Deposition is a balance between these variables, but concentration C is one of the most important values, because below a critical concentration, there will be no linear EPD deposition no matter how much voltage or deposition time change.^[5]

For both hexane and chloroform/acetonitrile, even though the concentration is doubled, the deposition does not double like in Hamaker's equation. This may be caused by the nanoparticles not being completely monodispersed. Nanoparticles of different sizes could deposit at different rates, because the larger the particle the stronger the surface charge has to be to EPD which may have caused the deviation from Hamaker's equation.^[3] However, we do not have enough data to confirm this because of

the limited supply of nanoparticles in each batch.

Another possibility is that the germanium concentration was not above the critical concentration, and doubling the concentration would not scale the deposition linearly.

d. Comparison of Nanoparticles

An essential factor for EPD is the nanoparticles themselves. For EPD to get a good deposition, particles have to be on the range of micrometers or smaller so they can be evenly dispersed in the solution instead at the bottom of a solution. Having monodisperse nanoparticles is also necessary for even deposition, because larger particles will settle out causing a gradient in deposition. Larger particles could also introduce the problem of crack formation on the deposited film.

The average deposition amounts varied depending on which germanium nanoparticle solution was used, as shown in

Tables 1 and 2. This does suggest that the deposition depends on the nanoparticle structure.

Figure 2 shows the TEM images of the nanoparticles. 3.34a has grains that range greatly in size and are not monodispersed. 3.35a does not show individual nanoparticles. 3.36a has nanoparticles that are close to the same size. 3.36b+wash shows nanoparticles, but they appear to be melded together.

Our initial hypothesis is that the better our nanoparticles appeared, the better they would deposit because smaller nanoparticles could pack more easily together and are less likely to form cracks. This is case for EPD in hexane, where 3.35b got the highest deposition while 3.35a got the lowest deposition in Table 2. However, for chloroform/ acetonitrile solution, the results were reversed and 3.35a got the highest deposition while 3.35b got the lowest deposition.

Though there is no reason explaining

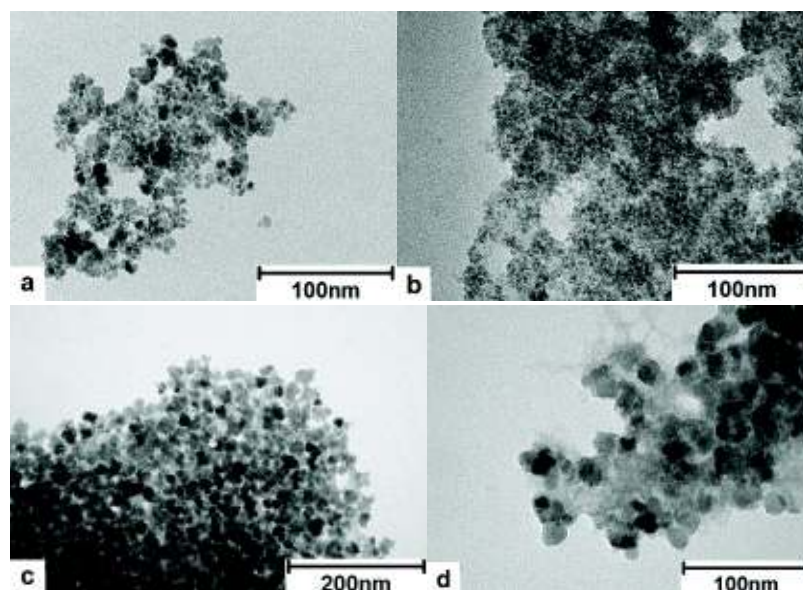


Figure 2: TEM images of nanoparticles: a) 3.34a, b) 3.35a c) 3.35b and d) 3.35b+ wash

why solvent affects deposition of differently shaped nanoparticles but one possible explanation may be in the ligands on the nanoparticle. The interactions between the solvent and the ligands on the nanoparticle do affect the nanoparticle's solubility which affects deposition.

When the germanium nanoparticle solution is in hexane, the more ligands that are adsorbed to the surface, the more soluble the germanium nanoparticles would be in hexane. In contrast, when the solvent is chloroform/acetonitrile, the germanium becomes more soluble with less ligands. This trend can be seen in comparing 3.35b with 3.35b+ wash. 3.35b+ wash has an extra rinse in ethanol to remove ligands. In hexane 3.35b had a higher deposition of .848 mg as compared to 3.35b+wash's deposition of .0095mg. For chloroform/acetonitrile, 3.35b+wash had a higher deposition of .0315mg while 3.35b has a deposition of .0149mg. These results indicate that nanoparticles deposit better in hexane when there are more ligands on the particle. The results also show that nanoparticles with less ligands deposit better in chloroform/acetonitrile.

IV. Conclusion

The use of polar vs non polar solvents does affect deposition though it is unclear why. Hexane causes deposition on the cathode while chloroform/acetonitrile causes deposition on the anode.

The structure of nanoparticles and the ligands impacts EPD deposition. As seen in Tables 2, hexane prefers to deposit nanoparticles that have more ligands

adsorbed on the surface. Table 1 shows that chloroform/ acetonitrile prefers to deposit nanoparticles with less ligands.

More data is needed to confirm these initial results. The problem with these experiments is that germanium nanoparticle production varies in quality and quantity. This leads to some nanoparticle batches getting more tests and more accurate data than other batches.

We now know that chloroform/acetonitrile have potential to do an unwanted redox reaction with copper. Since hexane does not allow redox reactions, our EPD trials in the future will be with hexane.

We also observed that better deposition happens in hexane when nanoparticles have more ligands. This inspired future projects about putting different types of ligands on nanoparticles to create better depositions.

In working with hexane we could save time by not working with bad nanoparticles like 3.35a, because Table 2 already reveals that bad nanoparticles do not deposit well.

More work needs to be done to get the nanoparticles look as similar as possible. We also need to do more work on getting even, reproducible EPD depositions. Once we are learn how to make uniform depositions, we can tune the process to investigate what amount of germanium makes the best anode for a lithium ion battery.

References

- [1] E. Yoo, J. Kim, E. Hosono, H. Zhou, T. Kudo, Itaru Honma Amer. Chem. Soc.

[2] M. Park, K. Kim, J. Kim, J. Cho. Adv. Mater. 22 (2014) 415-418.

[3] L. Bersa and M. Liu. Prog. In Mater. Sci. 52 (2006) 1-61.

[4] D. Ha, M. Islam, and R. Robinson. Nano Lett. 12 (2012) 5122-5130

[5] D. Vaughn II, J. Bondi, R. Schaak. Chem. of Mater. Sci. 22 (2010) 6103-6108

[6] S. Radice, C. R. Bradbury, J. Michler, and S. Mischle. Jour. Of Euro. Cer. Soc. 30 (2010) 1079-1088.

The Second Osmotic Virial Coefficient: *Determination from a Two-Component Equation of State and from Computer Simulation using Correlation-Function Integrals*

David Jahn¹, Dima Bolmatov², Benjamin Widom²

¹*Department of Physics, Brooklyn College of the City University of New York, New York 11210, United States*

²*Department of Chemistry, Baker Laboratory, Cornell University, Ithaca, New York 14853-1301, United States*

We have investigated the thermodynamic properties of dilute solutions, specifically determining the second osmotic virial coefficient B , using two methods: a) analysis proceeding from a two-component equation of state, namely deriving the solute activity $z_2(\rho_2, z_1, T)$ from an equation of state in the form $p = p(\rho_1, \rho_2, T)$, where ρ_1 is the solvent density and ρ_2 is the solute density, then solving for B by considering the expansion of solute activity z_2 in powers of the solute density ρ_2 at fixed solvent activity z_1 and temperature T , and b) considering the specific expression of B as a correlation-function integral, namely the a two-component Kirkwood-Buff integral, which equates the second virial osmotic coefficient B to the integral of the infinitely dilute limit of the solute-solute pair-correlation function $h_{22}(r)$ over all space. We apply these methods specifically to the calculation of B for dilute propane-water solutions using a mean-field equation of state with the Carnahan-Starling form of the hard-core repulsive term for method (a), and a molecular dynamics simulation for method (b).

Introduction

The osmotic second virial coefficient of a dilute solution is a measure of solute-solute interactions in the presence of a solvent. Its sign determines whether effective interaction between solute molecules is predominantly attractive or repulsive. In biological systems, the second virial osmotic coefficient B of dilute protein solutions has been shown to be correlated with protein crystallization¹, as well as protein solubility and phase behavior in aqueous solutions².

The osmotic pressure Π of a two-component system is defined as the difference

$$\Pi \equiv p(z_1, z_2, T) - p(z_1, 0, T) \quad (1)$$

between the pressure of a two-component liquid at temperature T with solvent at activity z_1 and solute at activity z_2 and the pressure of the pure solvent at the same activity and temperature.

In the limit of infinite solute dilution ($\rho_2 \rightarrow 0$), osmotic pressure Π is given by the van 't Hoff function

$$\Pi = \rho_2 kT \quad (2)$$

in terms of solute density ρ_2 , and solute activity z_2 is given by Henry's law

$$z_2 = \rho_2 / \Sigma \quad (3)$$

where Σ is the solubility of the solute in the solvent.

Taking into consideration deviations from these relations arising from solute-solute interactions as a solution becomes less dilute than the ideal infinite limit, Π and z_2 can be expanded in powers of ρ_2 at a given fixed z_1 and T :

$$\Pi = \rho_2 kT (1 + B\rho_2 + \dots) \quad (4)$$

$$z_2 = \frac{1}{\Sigma} \rho_2 (1 + 2B\rho_2 + \dots) \quad (5)$$

B here is known as the second virial osmotic coefficient. These relations were introduced in McMillan–Mayer solution theory³.

In a statistical mechanics sense, B in these expansions at a given fixed z_1 and T at infinite dilution is related to the integral of the infinitely dilute limit of the solute-solute pair-correlation function $h_{22}(r) = g_{22}(r) - 1$ by the equation

$$B = -\frac{1}{2} \int h_{22}(r) d\tau \quad (6)$$

where the integral is evaluated over all space. This thermodynamic / correlation-function relation is the infinitely dilute limit of one of the Kirkwood-Buff relations(4-7).

In this study we obtain a value for B first analytically by determining from an empirical equation of state an expression for $z_2(\rho_2, z_1, T)$, then solving for B in equation (5), and then computationally through performing a (relatively) dilute molecular dynamics simulation of propane in water and evaluating numerically the integral in (6).

Determining B from $p(\rho_1, \rho_2, T)$

Many empirical equations of state can be expressed as an analytic function of the form $p = p(\rho_1, \rho_2, T)$, including various parameters that may be adjusted to fit experimental data. Taking then the relation $(\partial F / \partial V)_{T, N_1, N_2} = -p$, where F is the Helmholtz free energy, V volume, and N_1 and N_2 the number of solvent and solute molecules respectively, we can integrate $p(N_1/V, N_2/V, T) - (N_1/V + N_2/V)kT$ with respect to V from an arbitrary V to $V = \infty$, holding the other variables constant. We then can use the fact that this integral is equal to the difference between the Helmholtz free-energy density $f = F/V$ and the ideal-gas $f_{i.g}$, to derive expressions for z_1 and z_2 in terms of ρ_1, ρ_2 , and T . Finally, we can invert the function $z_1 = z_1(\rho_1, \rho_2, T)$ to arrive at an expression for ρ_1 in terms of z_1, ρ_2 and T , which finally lets us derive a form for z_2 as a function of z_1, ρ_2 , and T . Since there is a direct relation between z_2 and B as given in equation (5), by simply setting z_1 as a constant equal to the solvent activity at liquid-liquid coexistence, and solving for B at various densities of ρ_2 (assuming all constants further than B in the series expansion are negligible), we can arrive at a close approximation to the “true” value of B for a given two-component equation of state.

As an example, taking a one-component mean-field equation of state with the Carnahan-Starling equation as its repulsive component, given by the formula

$$p = \rho kT \frac{1+b\rho+(b\rho)^2-(b\rho)^3}{(1-b\rho)^3} - a\rho^2$$

where the first term is the repulsive contribution parametrized by b , with

$$b = \frac{\pi}{6} \sigma^3 ,$$

σ being the hard sphere diameter of the molecule, and the second term being the attractive contribution of the system's effective potential, parametrized by a .

We adapt this equation of state to a two-component system in an analogous manner as ref. 8, first making the substitution

$$\rho = \rho_1 + \rho_2$$

where ρ_1 and ρ_2 are the respective densities of the solvent and solute, then taking the parameters a and b as weighted averages of parameters a_{ij} and b_{ij} with weights that are quadratic in the densities:

$$a = (\rho_1^2 a_{11} + 2\rho_1 \rho_2 a_{12} + \rho_2^2 a_{22}) / (\rho_1 + \rho_2)^2$$

$$b = (\rho_1^2 b_{11} + 2\rho_1 \rho_2 b_{12} + \rho_2^2 b_{22}) / (\rho_1 + \rho_2)^2$$

The two parameter equation of state is thus parametrized by six variables, two determining the solvent-solvent interaction (a_{11} and b_{11}), two determining the solute-solute interaction (a_{22} and b_{22}), and two determining the solute-solvent interaction (a_{12} and b_{12}).

Likewise as in ref. 8 we make our equations dimensionless by introducing the dimensionless variables

$$\varpi = \frac{b_{11}^2}{a_{11}} p, \quad t = \frac{b_{11}}{a_{11}} kT, \quad D_1 = b_{11} \rho_1, \quad D_2 = b_{11} \rho_2, \quad \alpha = a/a_{11}, \quad \beta = b/b_{11}$$

as well as defining

$$A_{12} = a_{12}/a_{11}, \quad A_{22} = a_{22}/a_{11}, \quad B_{12} = b_{12}/b_{11}, \quad B_{22} = b_{22}/b_{11}$$

so that

$$\alpha = (D_1^2 + 2D_1 D_2 A_{12} + A_{22} D_2^2) / (D_1 + D_2)^2$$

$$\beta = (D_1^2 + 2D_1 D_2 B_{12} + B_{22} D_2^2) / (D_1 + D_2)^2 .$$

We can use the process described above to determine the dimensionless second virial osmotic coefficient B/b_{11} for various values of D_1 assuming all osmotic virial coefficients beyond B are negligible, employing the derived parameters

$$a_{11} = 1.8865 \times 10^{-35} \text{ erg cm}^3, \quad b_{11} = 1.5703 \times 10^{-23} \text{ cm}^3$$

$$A_{12} = 1.6175, \quad B_{12} = 2.1500$$

and plugging in the parameters from ref. 8

$$A_{22} = 2.2201, \quad B_{22} = 4.096$$

This graph is presented in figure 1, which indicates a stable position in the graph at

$$B/b_{11} = -44, \quad B = -420 \text{ cm}^3/\text{mol}$$

indicating that the coefficient is no longer a function of density, giving a value for B comparable to that derived in ref. 8.

Determining B from the Solute Pair-Correlation Function

We performed an NVT ensemble molecular dynamics simulation of gaseous propane in a cubic box using the explicit-atom OPLS-AA potential model. These simulations were performed using the LAMMPS molecular dynamics software package. The size of the box was 1000 nm^3 (10 nm on a side), with either 20, 40, or 80 molecules simulated for 500ns each. The radial distribution function $g(r)$ between central carbon atoms of the 20 molecule simulation is presented in figure 3.

An NPT ensemble simulation of 1000 water molecules using the TIP4P/2005 model was also performed for 5ns, whose radial distribution function $g(r)$ between oxygen atoms is presented in figure 2.

Finally, these two models were combined in a system of 18 propane molecules and 4000 water molecules, which was simulated for approximately 200ps. Calculating the integral from equation (6) for this system numerically we obtain a very rough value of $B = 150 \text{ cm}^3 \text{ mol}^{-1}$.

Conclusion

In this study we calculated the second virial osmotic coefficient of a dilute propane-water solution using both analytic and computational methods. The equation of state using the Carnahan-Starling repulsive component generates a value for B of $-420 \text{ cm}^3 \text{ mol}^{-1}$, as compared to the value calculated by Widom and Underwood⁸ employing the van der Waals equation of state $-570 \text{ cm}^3 \text{ mol}^{-1}$, and a value of $-668 \text{ cm}^3 \text{ mol}^{-1}$ calculated by Liu and Ruckenstein¹² using the UNIQUAC¹³ and Wang-Chao¹⁴ equations of state.

Computationally, the explicit-atom OPLS-AA model for propane combined with the TIP4P/2005 model for water generated a tentative value of B of $150 \text{ cm}^3 \text{ mol}^{-1}$, which is somewhat more in agreement with the analytic approach than the three-point OPLS propane model employed by Koga and Widom⁹, which found a B value of $-40.9 \text{ cm}^3 \text{ mol}^{-1}$. It is possible that the model used in this work is producing a more accurate B than that of Koga and Widom due to its explicit-atom nature, although the duration of simulation was extremely short and the calculation may be imprecise. It is also possible that the simulation is insufficiently dilute to adequately model the second virial osmotic coefficient. Further work is necessary both to verify that this calculation of B is precise, and to determine the source of the discrepancy between values of B calculated by the analytic approach versus the computational approach.

Acknowledgements

I would like to acknowledge Professor Benjamin Widom for his guidance on this project, Dr. Dima Bolmatov for assistance, Baker Lab at Cornell University, as well as the CCMR REU program for allowing me the opportunity to conduct summer research. The CCMR REU program is funded by NSF Grant DMR-1120296.

References

1. Neal, B. L., et al. "Why is the osmotic second virial coefficient related to protein crystallization?." *Journal of crystal growth* 196.2 (1999): 377-387.
2. Ruppert, S., S. I. Sandler, and A. M. Lenhoff. "Correlation between the osmotic second virial coefficient and the solubility of proteins." *Biotechnology progress* 17.1 (2001): 182-187.
3. W. G. McMillan Jr, and J. E. Mayer. "The statistical thermodynamics of multicomponent systems." *Journal of chemical physics* 13 (1945): 276–305.
4. Kirkwood, John G., and Frank P. Buff. "The statistical mechanical theory of solutions. I." *The Journal of Chemical Physics* 19.6 (1951): 774-777.
5. Zimm, Bruno H. "Simplified relation between thermodynamics and molecular distribution functions for a mixture." *The Journal of Chemical Physics* 21.5 (1953): 934-935.
6. Ben-Naim, Arieh. *Water and aqueous solutions: introduction to a molecular theory*. New York: Plenum Press, 1974.
7. Ben-Naim, A. "Inversion of the Kirkwood–Buff theory of solutions: application to the water–ethanol system." *The Journal of Chemical Physics* 67.11 (1977): 4884-4890.
8. Widom, B., and Robin C. Underwood. "Second osmotic virial coefficient from the two-component van der Waals equation of state." *The Journal of Physical Chemistry B* 116.31 (2012): 9492-9499.
9. Widom, B., and K. Koga. "Note on the Calculation of the Second Osmotic Virial Coefficient in Stable and Metastable Liquid States." *The Journal of Physical Chemistry B* 117.4 (2013): 1151-1154.
10. Koga, Kenichiro. "Osmotic second virial coefficient of methane in water." *The Journal of Physical Chemistry B* 117.41 (2013): 12619-12624.
11. Koga, K., and B. Widom. "Thermodynamic functions as correlation-function integrals." *The Journal of chemical physics* 138.11 (2013): 114504.
12. Liu, H., and E. Ruckenstein. *The Journal of Physical Chemistry B* 102 (1998): 1005.
13. Prausnitz, J. M.; Lichtenthaler, R. N.; Gomes de Azevedo, E. *Molecular Thermodynamics of Fluid Phase Equilibria*, 2nd ed.; Prentice-Hall: Englewood Cliffs, NJ, 1986; pp 238– 245.
14. Wang, W.; Chao, K.-C. *Chem. Eng. Sci.* 1983, 38, 1483.

Second Osmotic Coefficient versus Propane Density

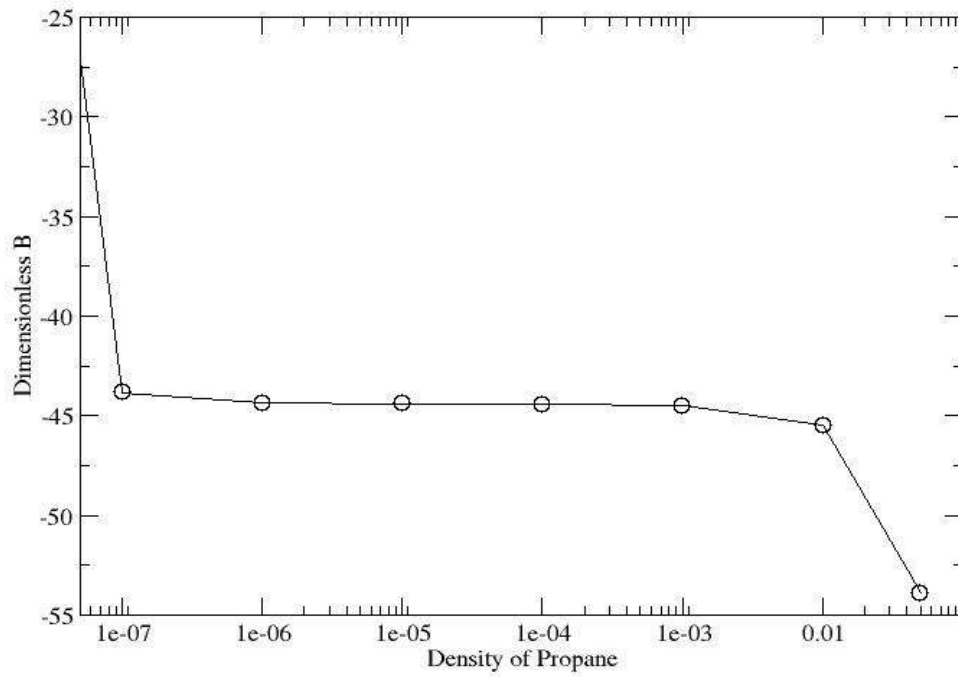


Figure 1: Plot of dimensionless B calculated for various propane densities

RDF for Simulated Water TIP4P Force Field

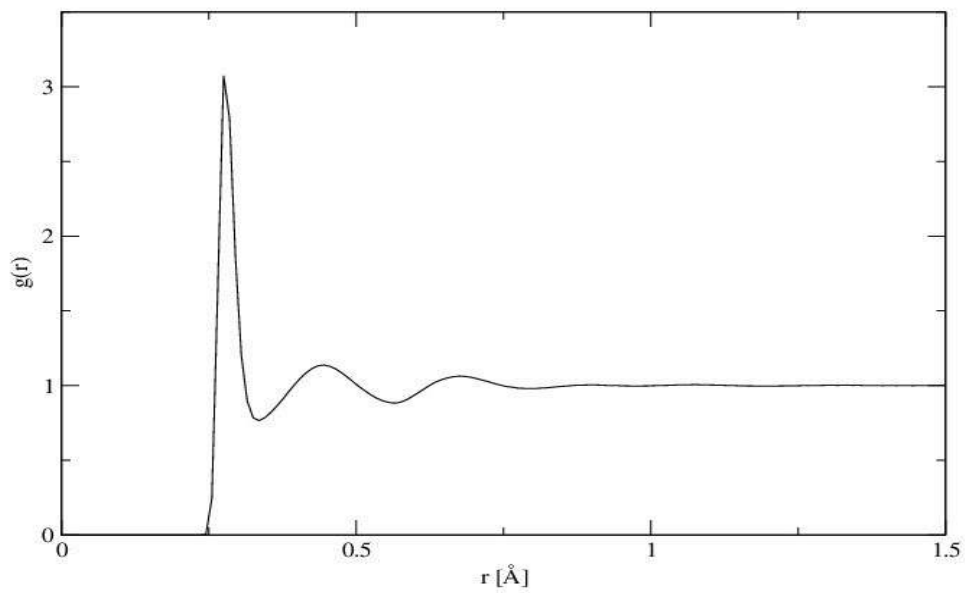


Figure 2: Plot of $g_{O-O}(r)$ for pure water, TIP4P/2005 potential model

Radial Distribution Function for Gaseous Propane

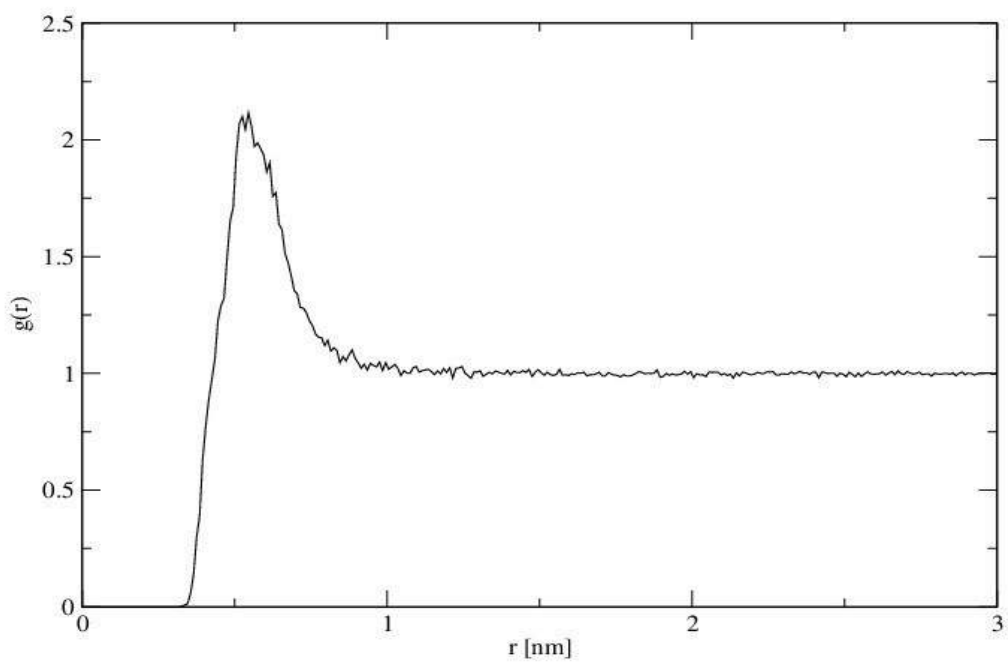


Figure 3: Plot of $g_{CH_2-CH_2}(r)$ for gaseous propane, OPLS-AA potential model

Mechanical Activation of Covalently Linked Spiropyran in PDMS Networks

Jesse Kidd¹, Jaewoo Kim², and Meredith Silberstein²

¹*Department of Chemistry, Concord University, Athens, WV*

²*Department of Mechanical and Aerospace Engineering, Cornell University, Ithaca, NY*

Abstract

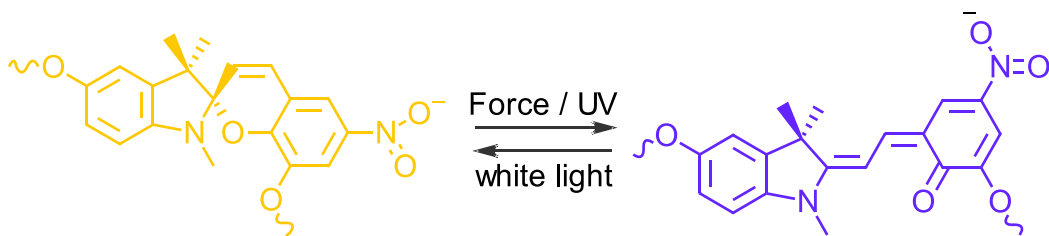
Mechanophore covalently linked poly(dimethyl)siloxane (PDMS) was synthesized through vinyl-terminated spiropyran (SP) and mechanical tests were performed under uniaxial extension and compression. Incorporation of the force-sensitive mechanophore, SP allows us to observe how it activates in response to PDMS networks. A silica filled commercialized Sylgard 184 was used as a base material and DCM or xylene was added as plasticizers for specimens containing spiropyran. Uniaxial extension samples shows a vivid color change and gradual increase in in-situ fluorescence intensity, demonstrating the conversion from spiropyran to merocyanine under extension. In the case of uniaxial compression fluorescence intensity also increases initially, but became saturated at around 60% strain. To understand silica filler effect on force transmission, unfilled PDMS was synthesized with SP through a hydrosilylation reaction. The spiropyran was force-activated as in filled-PDMS, but the sample failed at 40% strain before significant fluorescence was observed.

I. Introduction

As the need for stronger and smarter materials has increased the area of research called mechanochemistry has gained significant attention. Mechanochemistry can be defined as the study of force induced chemical reactions.¹ These chemical reactions may be utilized in areas of catalysis, supramolecular synthesis, regioselective and solvent free synthesis, and as a molecular level probe.^{1,2} At the forefront of mechanochemical research is the mechanophore, a molecule that reacts to external stimuli such as mechanical force. Mechanophores can be incorporated into a bulk polymer as a stress detector,³ thus increasing the reliability of engineering materials. Many force reactive mechanophores have been shown to exhibit useful optical properties when local force is induced.³ In particular, one mechanophore stands out as being reliable at detecting mechanical deformations in polymeric materials.

Spiropyran has been the subject of many studies when incorporated as a crosslink within polymeric materials.^{4,5} As reported in previous studies, when subjected to mechanical force spiropyran undergoes 6 π -electrocyclic ring opening to produce the colorful molecule

merocyanine⁶ (**Scheme 1**). The product merocyanine is produced through mechanical activation, UV radiation and heat. The reversible reaction occurs with exposure to white light over time. At the core of spiropyran is a spiro bond consisting of a C-N bond and C-O bond. Through the software simulations Steered Molecular Dynamics (SMD), Density functional theory (DFT), and Constrained Optimization (COGEF) the rupture of the C-O induces a ring arrangement to produce merocyanine.⁴ Besides color change, merocyanine has reported to be fluorescent with an excitation range of 550-590nm and an emission centered at 610nm.⁵



Scheme 1: Due to an external force or UV radiation, Spiropyran rearranges into the colorful Merocyanine. This process is reversible with exposure to visible light.

Polydimethylsiloxane (PDMS) is an organic polymer which exhibits great mechanical strength, stretchability, and transparency for an elastomer. PDMS is widely used in microfluid devices⁷, cosmetics, soft lithography⁸, and even silly putty. PDMS can be easily modified through additives that act as a plasticizer, making it more flexible and ductile. The commercialized PDMS Sylgard 184 contains silica filler to enhance its mechanical properties. While making the polymer very practical, the chemical structure becomes complicated and uncertain due to the presence of the filler.

Various modified PDMS networks were tested with and without the mechanophore spiropyran. Sylgard 184 was used as a base material to which the solvents dichloromethane (DCM) and xylene were added as plasticizers while incorporating spiropyran into the material. Like Sylgard 184, a unfilled PDMS was synthesized through a hydrosilylation catalyzed crosslinking reaction¹¹ with and without spiropyran. The objective of this research was to observe how spiropyran activates in modified PDMS networks.

II. Methods

Three different types of PDMS networks were tested with spiropyran. The first network was the commercially available Sylgard 184. Sylgard 184 is the basic PDMS polymer but with industrial additives to increase its ultimate strength, making it overall more glassy. It comes with two parts, a base agent containing the PDMS backbone and a curing agent which contains the PDMS crosslink and hydrosilylation catalyst. According to Dow Corning, the recommended ratio between base and curing agent is a 10:1 weight ratio. The spiropyran used in this project was a bis(methyl methacrylate) functionalized spiropyran.

A. Materials

Sylgard 184 base and cure kit was purchased from Dow Corning. Vinyl terminated poly(dimethyl)siloxane with an average molecular weight of 25,000 and viscosity of 850-1150 cSt, poly(methylhydro)siloxane of an average molecular weight of 1700-3200, and xylenes of ACS reagent, $\geq 98.5\%$ xylenes + ethylbenzene basis was purchased from Sigma Aldrich. Methylene chloride (DCM) HPLC grade was purchased from Fisher Scientific.

B. Spiropyran-DCM-Sylgard 184

0.05 wt % (2.4mg) spiropyran was dissolved in 5 wt % (0.316g) dichloromethane (DCM). This solution produced a rich and vibrant magenta color from the open ring form merocyanine. Once the mixture was homogenous, 10 parts (4.37g) of Base was mixed with 1 part (0.437g) Cure. The total mixture was stirred at room temperature for 30 minutes. During stirring the solution turned from light purple to pale yellow. The homogenous solution was then desiccated under vacuum for 1.5 hours. This step is to ensure the evaporation and separation of DCM from the PDMS-Spiropyran mixture. The resulting viscous pale yellow liquid was then poured into a 3-D printed dogbone molds and placed in a 65°C oven for 4-5 hours. The specimens were then transferred to an 80°C oven for 8-12 hours until fully cured. Cylindrical samples were obtained using the same synthesis by pouring the uncured product into test tubes.

C. Spiropyran-Xylene-Sylgard 184

Because Sylgard 184 polymer is a substantially strong rubber, a xylene additive was mixed into the Sylgard-Spiropyran mixture. Following the methods from a group at Duke University,⁹ 0.4 wt % (14.7mg) of spiropyran was dissolved in 10 wt % (0.365g) xylenes and vortex mixed until the spiropyran was fully dissolved. This yielded a greenish-blue solution, which was then mixed with 10 parts (3.32g) Base and vortexed. 1 part (0.332g) of Curing agent was added to the pinkish mixture and vortexed again until complete homogeneity. The mixture was then desiccated under vacuum for approximately 30 minutes to remove any bubbles, placed in molds and transferred to a 65°C vacuum oven for 16-18 hours until fully cured. Cylindrical samples were obtained then same way as the Spiropyran-Sylgard 184 specimens.

D. Spiropyran-PDMS

The third PDMS network tested was mixture of α,ω -divinyl-polydimethylsiloxane and polymethylhydrosiloxane (PMHS). This reaction was carried out through hydrosilylation by the catalyst chloroplatinic acid, H_2PtCl_6 . The Pt(IV) complex has been documented to be effective at activating Si-H bonds across alkenes.¹⁰ With a calculated PHR of 200:1, we decided to use a 5% PHR, making it a 10:1 ratio. A 0.05 wt % (1.9mg) of Spiropyran was dissolved in 5 wt% (0.19g) of DCM. 10 parts (3.66g) of divinyl functionalized PDMS, 1 part (0.366g) of PMHS, and 30 μL of an 8 wt% of H_2PtCl_6 solution was added and mixed for 6-8 hours at room temperature. The pale yellow mixture was then desiccated to remove excess DCM for 1.5 hours; poured into McLube 1711L coated molds, and placed in a 65°C oven. After 4-5 hours the molds were then transferred to an 80°C oven for 8-12 hours until cured fully.

E. Mechanical Testing and Optical Measurements

Uniaxial tensile and compressive loading was performed with a Zwick/Roell Z010 at a strain rate of $5 \times 10^{-3} \text{s}^{-1}$. A 532nm laser with an intensity of 8mW was directed towards specimens undergoing mechanical testing. If merocyanine was present the laser caused fluorescence, which was collected through a 570nm filter coupled with a Qimaging EXi Blue CCD camera. Intensity

was then measured through the program ImageJ by tracing the center of mass with respect to time to obtain an area of interest's mean intensity. Normalized Intensity was found by measuring the maximum intensity of a UV activated specimen and comparing the mechanically activated intensities through the equation:

$$I_{Normal} = \frac{I_{measured} - I_{minimum}}{I_{maximum} - I_{minimum}}$$

III. Results and Discussion

The mechanophore spiropyran was incorporated as a crosslinking agent to induce selective covalent bond scission in three PDMS networks. Spiropyran allows for the detection of the detection was damage through rupturing a C-O bond, undergoing a 6π-electrocyclic ring, reducing the HOMO-LUMO gap producing a longer emission wavelength into the visible spectrum. Dogbone shaped specimens were made for the three PDMS networks and Sylgard 184 and PDMS without spiropyran as controls. **Figure 1a** demonstrates the Stress vs. Strain curve of the three Sylgard 184 specimens. The control showed to be the most brittle of the three. The PDMS (DCM) and PDMS (Xylene) specimens proved to be more rubbery which is supported by Void Theory and Free Volume Theory. By implementing the solvents DCM and xylene, we increased the free space between polymer stands in PDMS.

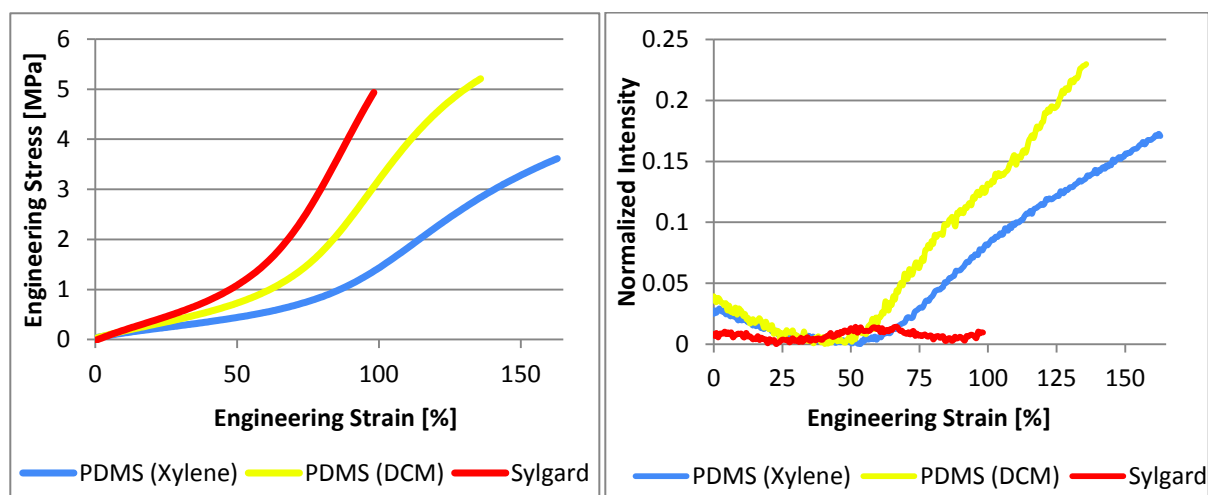


Figure 1 a) Stress vs. Strain curves for the three Sylgard 184 samples. By adding Spiropyran, DCM, and xylene the mechanical properties became more viscoelastic. **b)** Normalized Intensity vs. Strain curve of the three Sylgard 184 network

Because of the increased mobility between PDMS strands caused by DCM and xylene it is now possible to analyze the activation of Spiropyran as a function of mobility. **Figure 1b** denotes that normalized intensity vs. engineering strain plot. As strain increases in both the PDMS (DCM) and PDMS (Xylene) specimens the normalized intensity of fluorescence increases while the Control remains relatively 0. Also observed in **Figure 1b** is the initial

decrease in normalized intensity. It is believed that this was due to thinning of the specimen, reducing the concentration of merocyanine while at the same time the local forces within the polymer not being great enough to activate more merocyanine. Comparing PDMS (DCM) to PDMS (Xylene) shows that the PDMS (DCM) yields a higher normalized intensity. When coupled with the adjacent **Figure 1a** it's worth noting that PDMS (Xylene) experiences less stress and more strain compared to PDMS (DCM). Therefore; it's plausible to deduce that activating Spiropyran in a PDMS network is a stress/force driven reaction. This is also demonstrated by graphing the normalized intensity as a function of true stress.

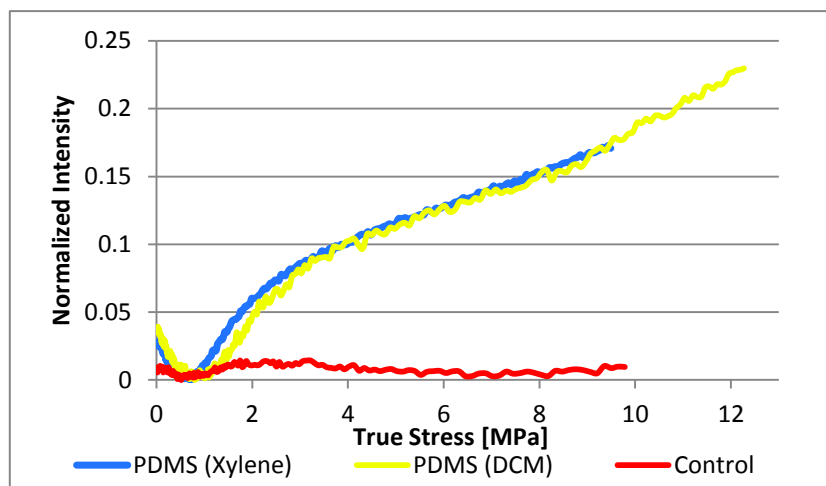


Figure 2 True stress vs. normalized intensity. As true stress increases the normalized intensity increases leading to the assumption that intensity is a function of stress.

During mechanical loading the conversion from spiropyran and merocyanine is a colored reaction. Spiropyran is a yellowish orange color and merocyanine is a deep magenta. **Figure 3** shows all specimens types testing and how they changed color initially, mechanically activated, and UV activated spiropyran. The first row contains the Sylgard samples without spiropyran, where no color change is seen. The last row contains the PDMS with spiropyran specimens. No color change is seen. There are several ideas as to why the color does not change. The PDMS specimen contains a naturally dark color that could inhibit fluorescence or the specimen may not be able to experience the necessary stress and strain needed to activate spiropyran.

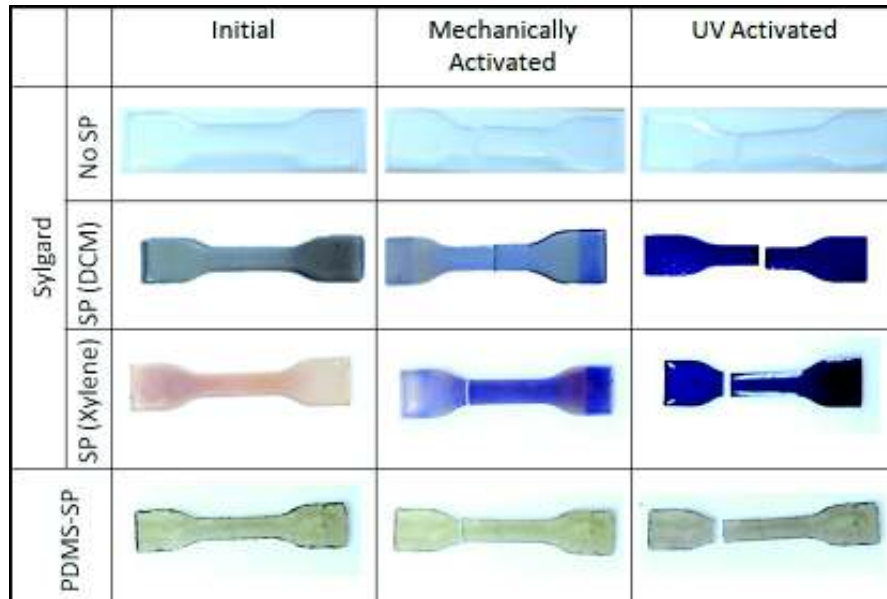


Figure 3 The color change seen from specimens initially, after mechanical loading, and after UV radiation.

The same experiment was conducted with uniaxial compressive loading where specimens were cylindrical shaped with a diameter to height ratio of 1:1. **Figure 4** shows the stress vs. strain curve and normalized intensity vs. strain curve. The plasticizing effects that the solvents DCM and xylene are again evident in the stress strain curve, **Figure 4a**. Both the PDMS (DCM) and PDMS (Xylene) specimens experienced greater strains at a lower stress compared to Sylgard. Similarly as stress and strain increases the normalized intensity increases, **Figure 4b**. However, at a strain of approximately 60% the PDMS (Xylene) specimens decrease in intensity. This implies that any merocyanine present would be converted into spiropyran leaving it colorless. Contrarily, the specimens were deep blue indicating an increase in the presence of merocyanine. The decrease in intensity is a reoccurring phenomenon seen in compression samples. This artifact could be due to the experimental setup or natural surface properties. It requires further investigation.

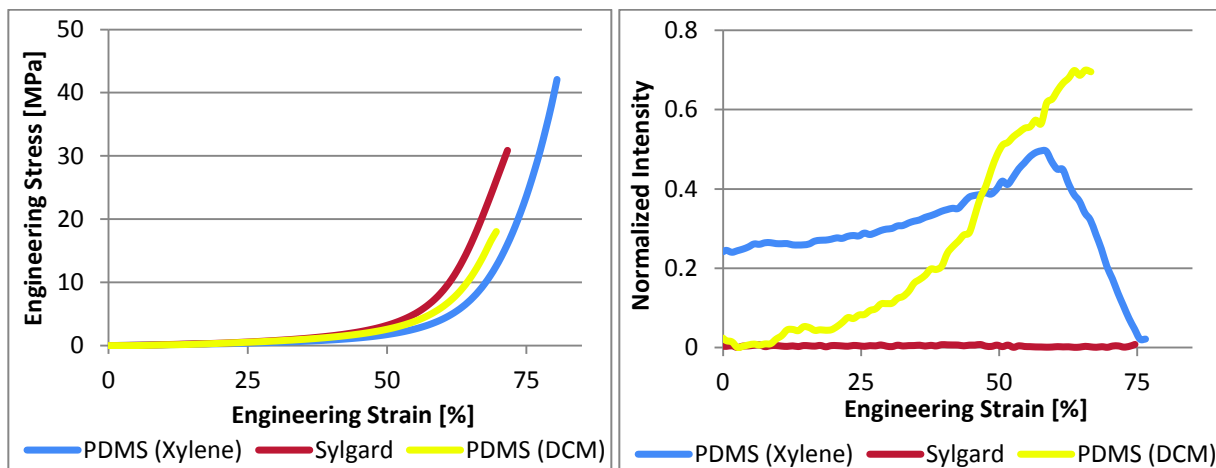


Figure 4 Uniaxial compression data **a)** The stress vs. strain curve of the three Sylgard 184 specimens. **b)** Normalized Intensity vs. strain curve of the three Sylgard 184 specimens.

When normalized intensity is graphed as a function of true stress in **Figure 5** a similar curve is produced. The PDMS (Xylene) specimens experienced a dramatic decrease in intensity as stress increased. The saturation effect is seen in the PDMS (DCM) curve at about 20 MPa. It's unusual that these curves formed when compared to the uniaxial extension specimens **Figure 2**. The curves are understandable and predicted in uniaxial extension, but for uniaxial compression unique graphs emerge creating ambiguity. Further testing is needed.

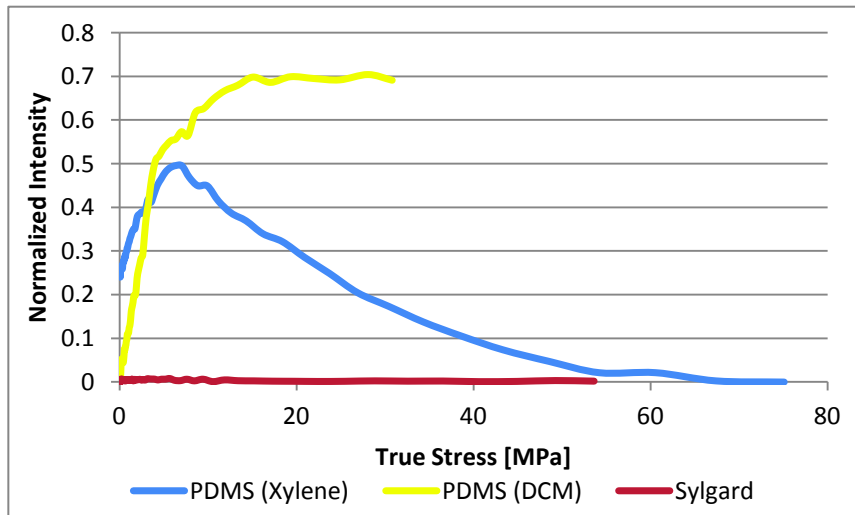


Figure 5 Uniaxial compression. Normalized intensity as a function of true stress for the three Sylgard 184 specimens. Unusual phenomena occur when compared to the curves for uniaxial extension.

As mentioned earlier, Sylgard 184 is a commercially available PDMS which contains many silica fillers to enhance its mechanical properties. The addition of filler adds ambiguity when one wishes to analyze or model how macroscopic force is transmitted to local force where spiropyran is especially useful. To overcome this, an unfilled PDMS was used with spiropyran as a molecular level probe. **Figure 6a** demonstrates the reproducibility of a stress/strain curve between the unfilled PDMS with and without spiropyran. The decrease in mechanical properties is evident when compared to the Sylgard curve in **Figure 1a**. Sylgard 184's measured stress reached 5 MPa and a maximum strain of approximately 100% where the unfilled PDMS had a significantly less stress and strain of 0.25 MPa and 43% respectively. **Figure 6b** shows the change in normalized intensity as strain is increased. The intensity of the PDMS-SP specimen did increase in intensity, however the curve is inconsistent and is not a significant increase when compared to the PDMS curve.

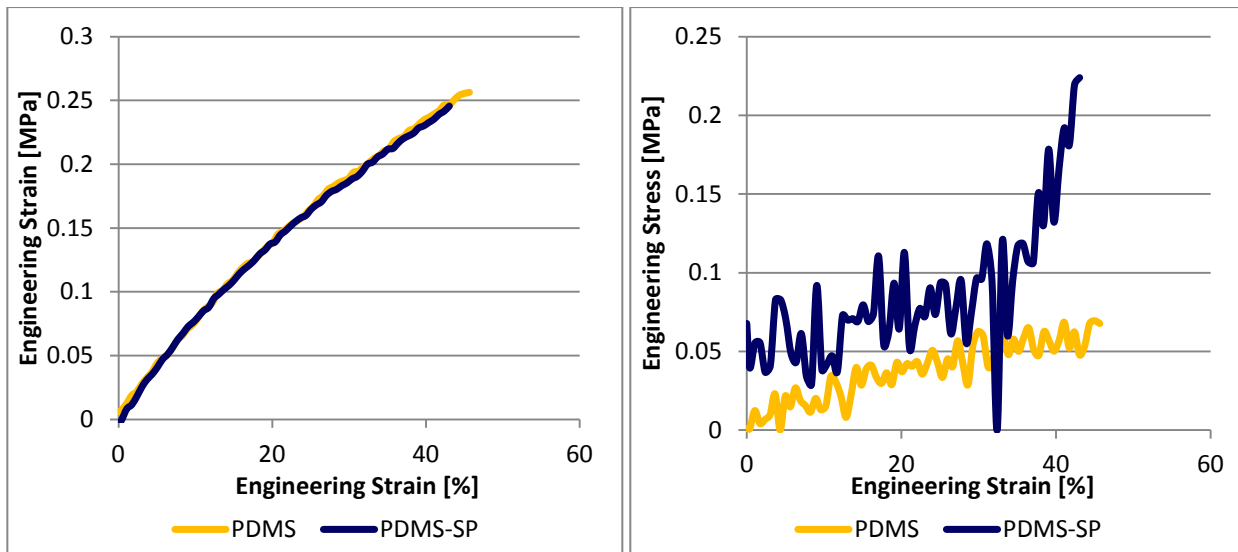


Figure 6 Unfilled PDMS specimens under uniaxial extension **a)** Stress vs.strain curve **b)** Normalized intensity vs. strain curve

The lack of increase in fluorescence of the unfilled PDMS samples with spiropyran could be due to a number of reasons. Because of the dark colored chloroplatinic acid catalyst used for hydrosilylation, the PDMS is characteristic of a naturally dark yellow/brown color. As a result, the natural color of the PDMS could prevent the escape of light from the fluorescent merocyanine. When exposed to UV light, the PDMS-SP samples increased in fluorescence slightly by approximately 50. This implies that the chemical identity of spiropyran has changed possibly due to the catalyst used. The absence of fluorescence increase as stress and strain increase leads to the assumption that the polymer may not be mechanically strong enough to enable activation of spiropyran.

IV. Conclusion

The mechanophore spiropyran was successfully crosslinked into various PDMS networks and molded into uniaxial extension dogbone shaped specimens and cylindrical uniaxial compression specimens. A silica filled commercially available Sylgard 184 was used as a base polymer to which DCM and Xylene was added as plasticizers to specimens containing spiropyran. This enabled observation of how spiropyran is activated with differing PDMS networks. Uniaxial extension specimens PDMS (Xylene) and PDMS (DCM) increased in merocyanine fluorescence as stress and strain increased while the Sylgard 184 specimen without spiropyran flat lined at a relative 0 normalized intensity. Uniaxial compression specimens exhibited unusual behavior in the PDMS (Xylene) samples where normalized intensity peaks at 60% strain then decreased to 0, this artifact may be due experimental setup or surface properties. Unfilled PDMS specimens with and without spiropyran was tested with uniaxial extension. The mechanical strength was significantly less compared to the silica filled Sylgard 184. As strain increased, normalized intensity increased in the PDMS-SP sample, but was too inconsistent and

not a significant increase when compared to the PDMS sample. As a whole, color change by mechanically activating spiropyran to merocyanine was observed in PDMS (Xylene) and PDMS (DCM) uniaxial extension and compression specimens.

V. Future Work

To further the investigation of the mechanophore spiropyran in PDMS networks, there are many areas to investigate and improve. The role that transition glass temperature has on the activation of spiropyran has yet to be investigated in depth. By adding the plasticizers such as DCM and xylene to the Sylgard 184, the viscoelasticity increased enabling the material to experience more strain at a lower stress. By monitoring the change in T_g and the activation of spiropyran a study can be conducted in determining how much stress and strain is necessary to activate spiropyran in foreign polymers.

The decrease in intensity seen in the PDMS (Xylene) and saturation of intensity of the PDMS (DCM) specimen in **Figure 5** is puzzling and interesting. By investigating the causes of these phenomena one may be able to construct a more realistic and expected increase in fluorescence intensity as stress and strain increase. As mentioned before, this property may be due to the experimental setup or surface property.

Unfilled PDMS containing spiropyran may yield many processing results as to understanding the exact mechanochemical pathway in spiropyran's activation. Modeling this phenomenon would become extremely less complicated compared to the unpredictable structure of Sylgard 184. However, results here are subpar. To improve the probability of obtaining better results a stronger more transparent material is needed. This can be accomplished by using shorter less heavy chains of vinyl terminated PDMS and PMHS. This would reduce the free space between the polymer strands increasing the mechanical properties. The use of an ideal hydrosilylation catalyst is also recommended, ideal meaning a catalyst that is not in solution and can be removed from the bulk polymer. If the catalyst cannot be removed, the catalyst must not affect the optical characteristics of the polymer (e.i. transparency).

VI. Acknowledgements

Funding for this research was supported through the NSF Grant DMR-1120296, part of the NSF MRSEC Program. Additional support was provided by Cornell University, the State of New York, and by industrial sources. Thanks Jaewoo Kim, Meenakshi Sundaram, Naigeng Cheng, Suwon Bae, and Meredith Silberstein for the encouragement and guidance.

VII. References

- 1 Lee, C. K.; Beiermann, B. A.; Silberstein, M. N.; Wang, J.; Moore, J. S.; Sottos, N. R.; Braun, P. V.; Exploiting Force Sensitive Spiropyrans as Molecular Level Probes. *Macromolecules*. **2013**, *46*, 3746-3752.
 - 2 James, S. L.; Friscic, T.; Mechanochemistry. *Chem. Soc. Rev.*, **2013**, *42*, 7494.
 - 3 Roberts, D. R. T.; Holder, S. J.; Mechanochromic systems for the detection of stress, strain and deformation in polymeric materials. *J. Mater. Chem.*, **2011**, *21*, 8256-8268.
 - 4 Davis, D. A.; Hamilton, A.; Yang, J.; Cremer, L. D.; Gough, D. V.; Potisek, S. L.; Ong, M. T.; Braun, P. V.; Martinez, T. J.; White, S. R.; Moore, J. S.; Sottos, N. R.; Force induced activation of covalent bonds in mechanoresponsive polymeric materials. *Nature Letters*, **2009**, *459*.
 - 5 Kingsbury, C. M.; May, P. A.; Davis, D. A.; White, S. R.; Moore, J. S.; Sottos, N. R.; Shear activation of mechanophore-crosslinked polymers. *J. Mater. Chem*, **2011**, *21*, 8381-8388.
 - 6 Tripikin, D. S. Mechanochromism of organic compounds by example of spiropyran. *Russ. J. Phys. Chem.* **2001**, *75*, 1720-1722.
 - 7 Fujii, T.; PDMS-based microfluid devices for biomedical applications. *Micr. Nano Engi.* **2011**, *61-62*, 907-914.
 - 8 Odom, T. W.; Love, J. C.; Wolfe, D. B.; Paul, K. E.; Whitesides, G. M.; Improved Pattern Transfer in Soft Lithography Using Composite Stamps. *Langmuir*, **2002**, *18* (13), pp 5314–5320.
 - 9 Gossweiler, G. R.; Hewage, G. B.; Soriano, G.; Wang, Q.; Welshofer, G. W.; Zhao, X.; Craig, S. L.; Mechanochemical Activation of Covalent Bonds in Polymers with Full and Repeatable Macroscopic Shape Recovery. *ACS Macro Lett.*, **2014**, *3* (3), pp 216–219.
 - 10 Benkeser, R. A.; Cunico, R. F.; Dunny, S.; Jones, P. R.; Nerlekar, P. G.; The formation of 1,6-bis(trichlorosilyl)hexane by the chloroplatinic acid catalyzed hydrosilylation of 1-hexyne. *J. Org. Chem.*, **1967**, *32* (8), pp 2634–2636.
 - 11 Sabourault, N.; Mignani, G.; Wagner, A.; Mioskowski, C.; Platinum Oxide (PtO₂): A Potent Hydrosilylation Catalyst. *Org. Lett.*, **2002**, *4* (13), pp 2117–2119.
-

(111) Silicon Native Oxide Coverage Metrology By Angle Resolved X-ray Photoelectron Spectroscopy

Erik R. Milosevic, Scott J Grutzik, and Alan T. Zehnder
Cornell Center for Materials Research
Cornell University, Ithaca, NY 14853

In 2006 T. Alan *et al.*¹ noted that silicon nanobeams exhibited a decrease in strength upon the oxidation of their (111) planar surface. An understanding of this phenomenon is necessary to current research on nanoscale systems such as MEMS devices and three dimensional integrated circuits. The rate of oxide growth on this planar surface is an important piece of information needed to better understand this decrease in strength. Here, silicon samples were allowed to oxidize in a variety of environments. Using angle resolved X-ray photoelectron spectroscopy and the quantitative analysis software QUASES-ARXPS the samples were measured at regular intervals during the oxidation process to determine a rate of oxide growth. Samples oxidized as expected. For the two of the oxidation environments and for early data points in the third, unrealistically thin native oxide thicknesses are computed by QUASES-ARXPS. This arises from a lack of complete oxide surface coverage.

I. Introduction

An understanding of the mechanical properties of silicon has become vital to the development of next generation MEMS devices and integrated circuits. These devices have adopted complex and delicate architectures that rely heavily on a complete understanding of the mechanical strengths of silicon. T. Alan *et al.*¹ reported that silicon nanobeams exhibited a decrease in strength upon the formation of a native oxide on the (111) planar surface of the beams. Insight into the mechanism of this phenomenon is critical to research involving the use of nanoscale silicon structures, as well as the development and functionality of the devices spoken to above.

A quantitative description of the changes in coverage and thickness of the oxide layer over time is a needed piece of information for the development of a mechanism. A method of using X-ray photoelectron spectroscopy (XPS) to measure thick, artificially grown silicon dioxide layers on crystalline silicon is described by Z. H. Lu *et al.*². Their method uses the intensity ratio of

the Si 2p peak (I_{Si}) and the SiO₂ peak (I_{oxy}) to determine the thickness of the oxide layer (d_{oxy}) by the equation

$$d_{oxy} = \lambda_{oxy} \sin \alpha \ln [I_{oxy} / (\beta I_{Si}) + 1]$$

where α is the photoelectron takeoff angle, λ_{oxy} is the silicon dioxide photoelectron effective attenuation length and β is defined as $I_{oxy,\infty} / I_{Si,\infty}$, which is the ratio of the intensity of an infinitely thick oxide layer to an infinitely thick silicon layer.

An improvement on the above method can be made through the use of angle resolved X-ray photoelectron spectroscopy (ARXPS) in conjunction with the quantitative analysis software QUASES-ARXPS³. This allows the acquisition of structural information such as the thickness and percent coverage from extremely thin native oxide layers.

II. ARXPS Procedure and Parameters

XPS spectra were taken with a binding energy range from 92eV to 112eV as the

peaks of interest, the Si $2p$ peak and the SiO₂ peak, have characteristic binding energies of 99.3eV and 103.3eV, respectively⁴. The incident beam had an energy of 50V and was 55° from normal with respect to the sample. This angle did not change during ARXPS analysis. The beam was 1mm in diameter and the spot formed a 1mm x 2mm ellipse on the surface of the sample. Spectra were taken using the above conditions at 0°, 10°, 20°, 30°, 40°, 50°, and 60° from normal relative to the electron detector. The resulting Si $2p$ and SiO₂ peaks for each angle and sample were integrated to determine their intensities relative to one another.

Upon the acquisition of the relative intensities, the information was input into the quantitative analysis software QUASES-ARXPS which fits a model to the input data. The oxidative coverage of the samples was assumed to be 100%. The electron mean free paths corresponding to the various layers of the structure were needed for the QUASES-ARXPS software to function. The mean free paths used were obtained from S. Tanuma *et al.*⁵ and are as follows:

Table I:

$\lambda(\text{SiO}_2)$ in SiO ₂	7.74Å
$\lambda(\text{SiO}_2)$ in Si	5.53Å
$\lambda(\text{Si})$ in SiO ₂	7.69Å
$\lambda(\text{Si})$ in Si	5.27Å

The coverage and concentration of each layer were held at 100% in the software. The thickness was varied to produce the curve that best fit the data. The resulting model would be representative of the measured sample.

III. Experimental Methods

Samples were 1cm x 1cm chips cut from the same (111) silicon wafer. The samples were subjected to the standard RCA clean⁶:

Table II:

10 min at 70°C in

5 parts DI H ₂ O
1 part NH ₄ OH
1 part H ₂ O ₂

10 min at 70°C in

5 parts DI H ₂ O
1 part HCl
1 part H ₂ O ₂

The HF dip was excluded from the standard RCA clean. Following the two steps above, the samples were placed in a 6:1 H₂O : Buffered Oxide Etch (BOE) solution for 30 seconds to strip the surface of any silicon dioxide. BOE was used over HF as BOE produces a smoother surface⁷.

After cleaning, the samples were left to naturally oxidize in one of the following three environments:

Table III:

Environment	% Relative Humidity
Atmospheric	60*
Dry	25
Wet	100

*Samples were subjected to normal atmospheric humidity fluctuations in an indoor laboratory space.

Two silicon chips were oxidized in each environment. ARXPS analysis of one chip from each environment was done after 1, 2, and 3 days of exposure. ARXPS analysis was performed on the remaining three chips after 1, 5, 11, 19, and 33 days of exposure.

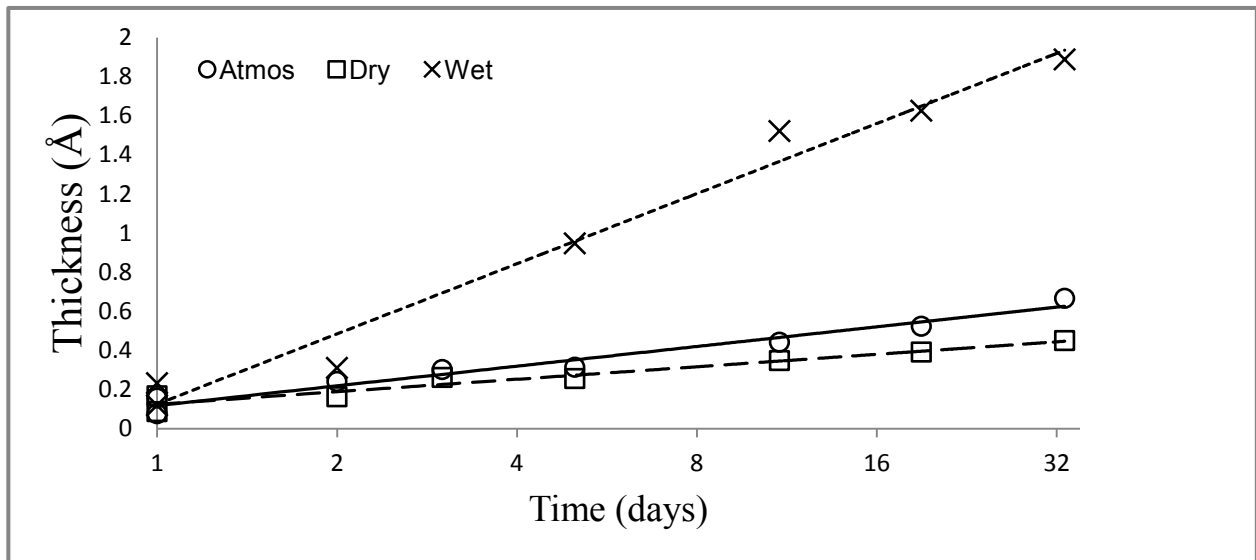


Figure 1: Thickness as a function of time. (Time in log scale)

IV. Experimental Results and Discussion

A plot of the oxide thickness as a function of time can be seen in Figure I. This is the result of an analysis assuming a coverage of 100%. As the samples become more oxidized, the rate at which the oxidation process occurs decreases. Unrealistically thin oxide layers were measured for the atmospheric and dry samples, as well as for the early data points of the wet sample. This can be attributed to a lack of complete oxide layer coverage on the silicon surface. The leveling of the wet samples curve over time is indicative of oxidative coverage approaching 100%. This is in agreement with U. Neuwald *et. al.*⁸ who reported full oxidative coverage in approximately 33 days.

V. Conclusions

In summary, the rate of native silicon dioxide growth on (111) planar silicon was measured using an improved technique that consisted of angle resolved X-ray photoelectron spectroscopy and the software QUASES-ARXPS. The exact method is outlined in detail for future reference.

Samples were determined to be oxidizing at a rate in agreement with previous research⁸. Reported unrealistic thicknesses were likely due to the lack of complete oxidative coverage at the time of measurement. Once a full layer of oxide is achieved, oxide thickness will continue to slowly increase until an equilibrium thickness is achieved. Future work will consist of determining the effective thickness of a monolayer of silicon dioxide and using this to determine the coverage at the data points that output unrealistic thicknesses.

VI. Acknowledgments

This work made use of the Cornell Center for Materials Research Shared Facilities which are supported through the NSF MRSEC program (DMR-1120296). This work was funded by the National Science Foundation (NSF) grant CMMI-0856488. This work was supported by the Cornell Center for Materials Research with funding from the Research Experience for Undergraduates program (DMR-1063059 and DMR-1120296). This work was performed in part at the Cornell NanoScale Facility, a member of the National Nanotechnology Infrastructure Network,

which is supported by the National Science Foundation (Grant ECCS-0335765).

¹T. Alan, and A. T. Zehnder, Appl. Phys. Lett. **89**, 231905 (2006)

²Z. H. Lu, J. P. McCaffrey, B. Brar, G. D. Wilk, R. M. Wallace et al, Appl. Phys. Lett. **71**, 22746 (1997)

³T. S. Lassen and S. Tougaard. *QUASES-ARXPS User's Guide: Quantitative Analysis of Surfaces by Electron Spectroscopy*. Tougaard ApS, ver. 1.1. (2012).

⁴J. F. Moulder, W. F. Stickle, P.E. Sobol, and K. D. Bomben, 1995, *Handbook of X-ray Photoelectron Spectroscopy*, ULVAC-PHI, Chigasaki

⁵S. Tanuma, C. J. Powell, and D. R. Penn, Surf. And Inter. Anal. **21**, 165-176 (1993)

⁶K. Werner, J. Electrochem. Soc. Vol. 173, No. 6 (1990)

⁷S. P. Garcia, H. Bao, M. H. Hines, Surface Science, **541**, 252-261 (2003)

⁸U. Neuwald, H. E. Hessel, A. Feltz, U. Memmert, and R. J. Behm, Appl. Phys. Lett. **60**, 1307 (1992)

Photoelectrochemical Oxidation of Water and Sulfite on Titanium Dioxide Nanorods

Erin Nissen¹, Justin Sambur², and Peng Chen²

¹Department of Chemistry, Colorado Mesa University, Grand Junction, CO 80515

²Department of Chemistry and Chemical Biology, Cornell University, Ithaca, NY 14853

ABSTRACT: Titanium dioxide nanorods have been used as a semiconductor electrode for the photooxidation of water and sulfite. Upon addition of sodium sulfite, an easily oxidizable scavenger molecule, anomalous current-voltage behavior was observed. An extreme enhancement of the current at positive potentials was observed, while the opposite trend occurred at negative potentials. One possible reason for such behavior is due to trace transition metal impurities on the surface of the nanorods that act as catalyst sites, which were incorporated into the material during the high-temperature molten-flux salt synthesis procedure.

Introduction

The world's population is expected to reach 8.5 billion people by the year 2030.¹ With this daunting increase in population the demand for energy will increase to 27 TW by the year 2030.² Currently 2.4 million pounds of CO₂ is released into the atmosphere every second,³ as the energy demand increases the amount of CO₂ pollution will be catastrophic.

One desirable approach to avoid such disastrous effects of increasing atmospheric CO₂ on the environment is to use clean energy resources such as wind, geothermal or solar. Of these possible renewable energy sources, solar energy has the potential to meet the ~27 TW global energy demand. In fact, there is enough solar energy striking the Earth's surface in one hour to account for the amount of energy consumed globally in one year!⁴ Harnessing this energy would allow for a theoretical yield of 60 TW².

Currently the only commercially available solar energy conversion technique is photovoltaics, a process involving solar energy conversion to electricity. Although this approach is promising, there is no way to account for the diurnal nature of the sun; no electricity is generated at night. Thus, an attractive strategy would convert solar energy to a chemical fuel that could be used on-demand.

To achieve this goal, many researchers are pursuing photoelectrochemical solar energy conversion to hydrogen. Fujishima and Honda were the first to demonstrate this approach by studying photo-assisted water splitting on TiO₂ electrodes.^{5,6} In this strategy, photons from the sun are used to split water molecules on the surface of a semiconductor to produce hydrogen and oxygen. The hydrogen can be stored and used when appropriate in fuel cells, expelling the only byproduct, water. Although tremendous research has been focused on this goal, several challenges still remain. In order to realize wide-scale commercialization of solar water splitting cells, a low-cost, earth-abundant, highly efficient and chemically stable semiconducting material must be discovered.

Since Fujishima and Honda's discovery, many advancements have been made towards harnessing chemical energy from splitting water. Current research has focused on the surface kinetics between the electrode and electrolyte. Chow *et al.* recently reported on the photooxidation of water on bare and catalyst-modified bismuth vanadate (BiVO₄).⁷ On the bare BiVO₄ surface, water oxidation proceeded slowly compared to the oxidation of sulfite. However, when an oxygen evolution catalyst was coated on the surface of BiVO₄, the photocurrent greatly increased and

almost reached the photocurrent observed for sulfite oxidation. They concluded that in the presence of surface catalysts, the photocurrent response dramatically increased due to an increase in surface kinetics.

Following the strategy of Chow *et al*, herein we studied sulfite oxidation and water oxidation by TiO₂ nanorods.

Experimental

Nanorod Synthesis. All chemicals were purchased from Sigma-Aldrich. The synthesis of TiO₂ nanorods has been previously described in detail.⁸ In a typical synthesis, a mixture of 25 nm rutile and anatase nanoparticles (Degussa P25), NaCl, and Na₂HPO₄ in a 1:1:4 by weight ratio. After annealing the samples at 850 C for 30 hours, each was washed with boiling hydrochloric acid three times to remove any remaining salt crystals.

Electrode preparation. A 4:1 by volume ethanol:water solution was then spin casted at 750 rpm onto an In-doped Tin Oxide (ITO) transparent conducting electrode. The electrode was annealed at 450C for 30 min prior to use.

Photoelectrochemical measurements. All measurements were performed in 13 mL of N₂-purged 1 M KCl, pH 8.3 100mM sodium borate electrolyte solution. The photoelectrochemical measurements were recorded using a CH-Instruments potentiostat and a one compartment photoelectrochemical cell. TiO₂ nanorod-coated ITO, Pt wire and a Ag/AgCl electrode served as the working, counter and reference electrodes, respectively. Chopped illumination (100 mHz) from a 365 nm UV light source (8mW) was used for each measurement unless stated otherwise.

Various measurements were recorded using a SRS model 810 lockin amplifier to enhance the photocurrent signal. The analog output from a CV 27 potentiostat served as the current input to the lockin amplifier. All currents were recorded using a scan rate of -1 mV/s scanning from 200mV to -800mV. Current measurements were reported using settings R, 90 degrees out-of-phase Y, and

modulating sin wave for initial, negative, and steady state current in the corresponding order.

Results

When the TiO₂ nanorod covered ITO electrode is subjected to UV light pulses there is an initial excitation of an electron from the valence band into the conduction band, sending a hole to the interface between the electrolyte solution and the semiconductor surface. A series of reactions take place at the interface to oxidize water at the surface to oxygen (eqns 1-7 below). The electrons are collected at the ITO electrode and continue through the external circuit creating a (photo)current. The electrons finally reach the platinum cathode where they reduce water/protons to hydrogen. Figure 1 demonstrates typical photocurrent-time responses for TiO₂ nanorods as a function of applied bias.

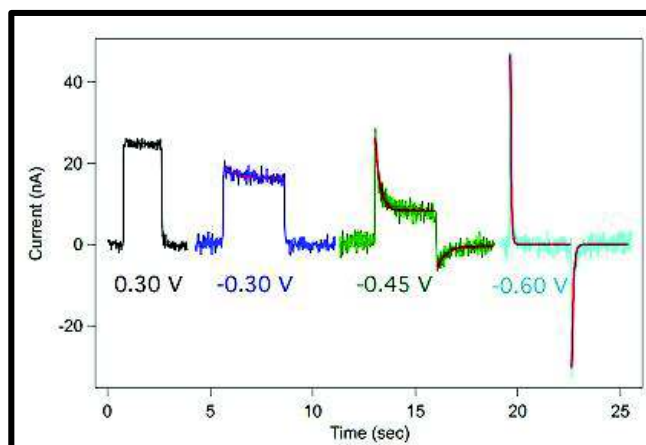
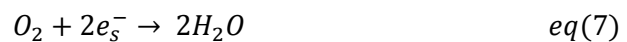
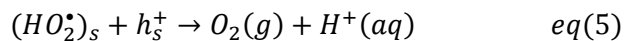
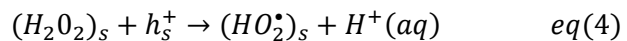


Figure 1. Photocurrent transient effects demonstrated at various Potentials.

If photooxidation of water proceeds efficiently on the electrode surface, then the photocurrent is expected to be stable with time (black trace, +300 mV). However, at more negative potentials, the photocurrent decays with time. The decay of the photocurrent is best understood by considering the irreversible elementary steps written in eqns 1-7 below. It has been suggested and experimental shown that at certain applied potentials, one or more of the elementary steps does not proceed efficiently and therefore, the photocurrent decreases with time. In other

words, one step acts as a 'kinetic bottleneck' that limits performance.



These steps result in the interesting dynamics of the photocurrent with modifications in the potential as seen in the transient transformations in Figure 1. Equation (1) demonstrates the initial onset of photocurrent when the photoelectrochemical cell is subjected to UV photons.

The current immediately begins to decay with time as surface intermediates are formed in equation (2-5) and begin to recombine with electrons found on the surface until reaching a steady state current as seen in equation (6). Lastly, when the light is turned off, all remaining electrons which were not collected by the electrode flow back to the interface of the solution, switching the flow of the current, and resulting in a negative spiking current, and recombine with any unreacted oxygen or intermediates left over which is demonstrated in equation (7).⁹

These dynamic photocurrent responses were reconstructed at each potential to form the current vs voltage plot in Figure 2. It is obvious to see the sharp decrease of steady state current at approximately -600 mV vs Ag/AgCl is commensurate with the maximum of the initial and negative current. This qualitatively

illustrates that there is only excitation and recombination events occurring at potentials more negative than -550 mV, and overall water oxidation does not occur.

There has been a lot of research done to improve the current response by adding a catalyst to the surface of the electrode in order to increase the rate of water oxidation. Another approach is to add an easily oxidizable molecule, which can react with holes on the surface and increase the flow of electrons to be collected at the electrode. This approach is advantageous because without modifying the electrode, it is possible to characterize the energy conversion efficiency (albeit to an undesired chemical reaction, e.g. sulfite oxidation).

Previous work by Hamann and co-workers demonstrated an increase in steady state current

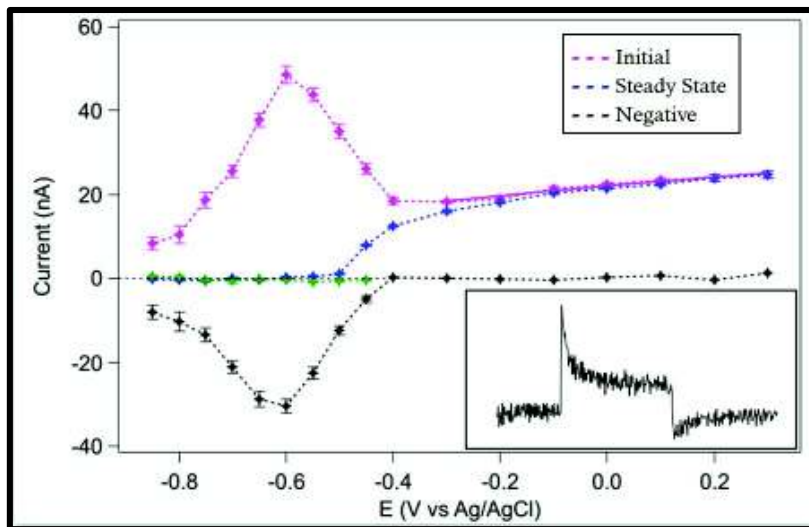


Figure 2. Reconstructed Current vs Voltage curve for the photooxidation of water on TiO₂ nanorods.

by the photooxidation of iron (II) ferrocyanide, a common fast one-electron redox couple used in electrochemistry. They showed that increasing amounts of scavenger lead to a corresponding increase in the steady state photocurrent.¹⁰

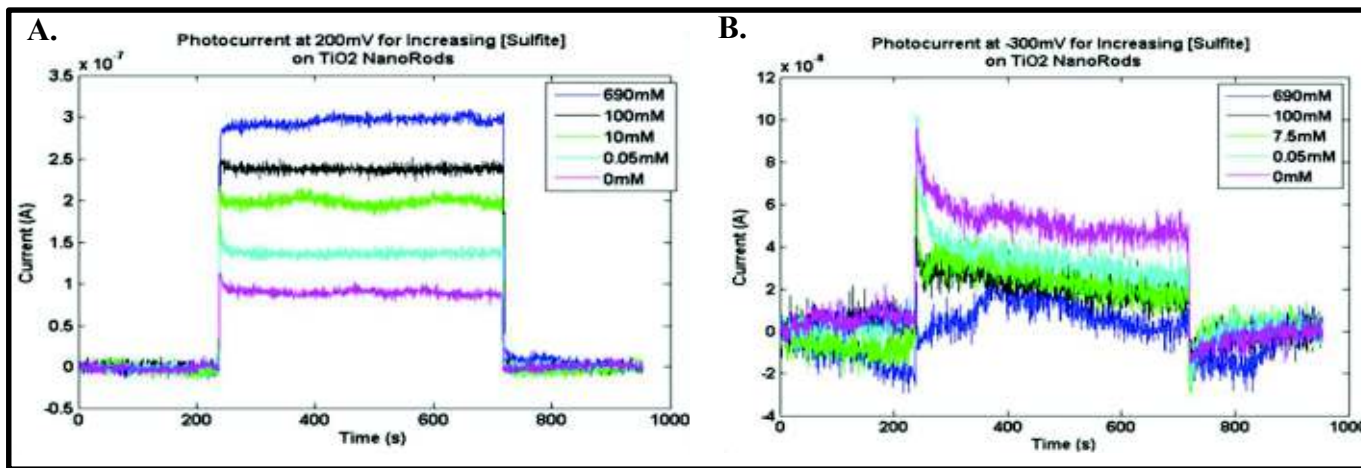


Figure 3. A representative pulse from the photooxidation of water on TiO₂ nanorods in the presence of increasing Sodium Sulfite concentration at 8mW for 100mHz cycles at A.) 200mV and B.) -300mV.

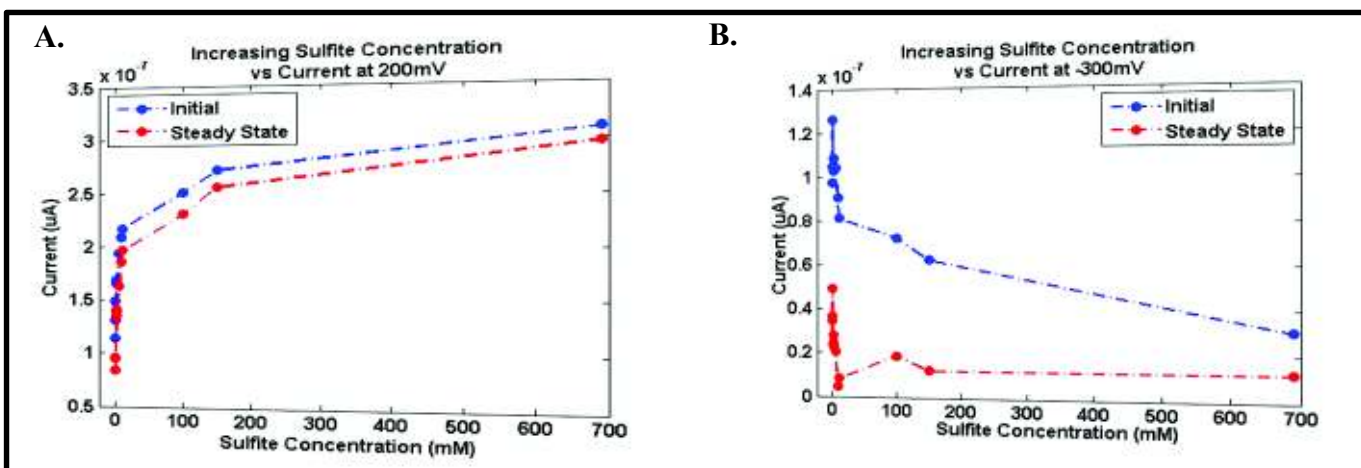


Figure 4. The current response plotted at a function of Sodium Sulfite Concentration for Initial and Steady State Current at A.)200mV and B.) -300mV.

Following this approach, sodium sulfite, another common scavenger molecule, was added to the electrolyte solution in increasing amounts in an attempt to increase the photocurrent response. Figure 3 shows the photocurrent response as a function of increasing sulfite concentration in the electrolyte solution at positive and negative bias. Figure 4 shows a plot of the initial and steady state current values as a function of added sulfite. At positive bias, the initial and steady state photocurrents increase with sulfite concentration. However, at negative bias, the opposite trend was observed. Furthermore, the full current vs voltage

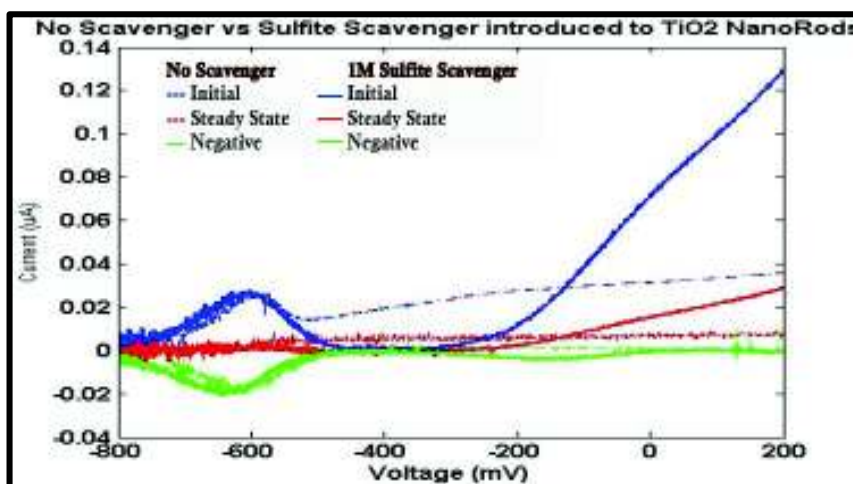


Figure 5. Current vs Voltage curve comparing bare TiO₂ nanorod oxidation of water to 1M Sodium Sulfite oxidation.

curve in Figure 5 demonstrates the true difference in bare TiO₂ vs the addition of 1M scavenger molecule. There is an extreme rise in photocurrent at positive potentials, while negative potentials result in little to no photocurrent, and the humping region at -600 mV seems to be unaffected.

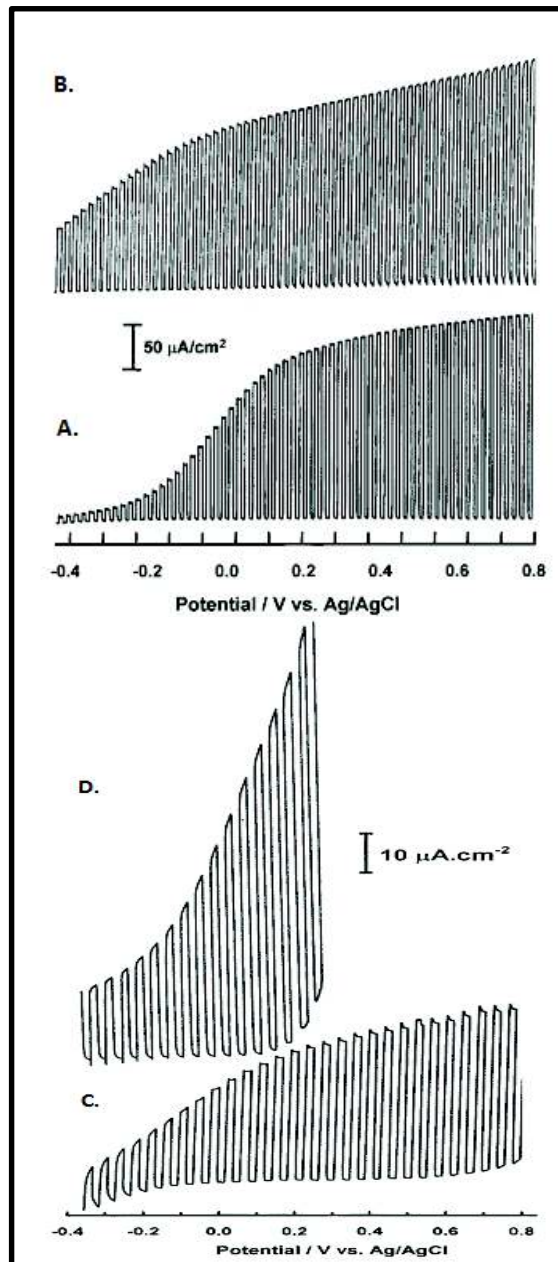


Figure 6. Photocurrent-potential profiles under chopped irradiation for **A.** a neat TiO₂ thin film in 0.1 M NaNO₃ **B.** and in 0.1 M Na₂SO₃ + 0.1 M NaNO₃. Photocurrent-potential profiles under chopped irradiation for **C.** Ni(0.01)-TiO₂ composite film in 0.1 M NaNO₃ **D.** and in 0.1 M Na₂SO₃+0.1 M NaNO₃.

Discussion

These photocurrent results shown in Figure 6 were previously observed by Rajeshwar and co-workers¹¹ on nickel doped TiO₂ films. They found that in the presence of Ni there is a sharp, significant increase in the photocurrent only in the positive voltage regime, while the addition of sulfite on bare TiO₂ increased the photocurrent only in the negative voltage region. These results imply that there are metallic impurities in the TiO₂ nanorods in this study.

The synthetic approach previously discovered by Yang and co-workers was also used to prepare nanorods with 2% doping densities of many transition metals.⁵ We believe that the impurities from the starting materials, NaCl and sodium phosphate, may also introduce trace impurities into our bare TiO₂ nanorods. The incorporation of these transition metal impurities could account for the observed behavior described herein.

Conclusion

Water oxidation can be performed by the illumination of TiO₂ nanorods with UV light. However, the reaction requires 4 holes and is often kinetically difficult, leading to reduced photocurrents. We observed that in the presence of sodium sulfite, the photocurrent increased in the positive potential regime, but does not improve the photocurrent at negative potentials. This clearly demonstrates that surface kinetics limits the photocurrent efficiency at positive potentials. In addition, the results suggest that transition metal impurities may be present on the surface of the nanorods.

ACKNOWLEDGMENT

I would like to thank The National Science Foundation and Cornell Center for Material Science Research for giving me the opportunity to conduct research in the Chen group this summer. I would also like to thank Dr. Peng Chen for welcoming me into his lab group, and specifically Dr. Justin Sambur for providing mentorship throughout the entire summer, and making me feel welcome in the Chen group.

REFERENCES

- ¹ <http://www.businessinsider.com/analyst-world-population-will-peak-at-85-billion-in-2030-2012-11>
- ² <http://nsl.caltech.edu/energy>
- ³ <http://www.cbsnews.com/news/carbon-dioxide-emissions-rise-to-24-million-pounds-per-second/>
- ⁴ <http://www.txses.org/solar/content/solar-energy-facts-you-should-know>
- ⁵ A. Fujishima and K. Honda, *Nature*, 1972, 238, 37.
- ⁶ Klahr, B., Giménez, S., Fabregat-Santiago, F., Bisquert, J., & Hamann, T. W. (2012). *Energy & Environmental Science*, 5(6), 7626. doi:10.1039/c2ee21414h
- ⁷ Kim TW, Choi KS. 2014. *Science*. 243(990-994).
- ⁸ Roy B, Ahrenkiel SP, Fuieler PA. 2008. Controlling the size and morphology of TiO₂ powder by molten and solid salt synthesis. *Journal of the American Ceramic Society*. 91(8):2455–63
- ⁹ Tafalla, D., Salvador, P., & Benito, R. M. (1990). Kinetic Approach to the Photocurrent Transients in Water Photoelectrolysis at n-TiO₂ Electrodes II. Analysis of the Photocurrent-Time Dependence. *Journal of the Electrochemical Society*, 137(6), 1810–1815.
- ¹⁰ Klahr, B. M., & Hamann, T. W. (2011). Current and Voltage Limiting Processes in Thin Film Hematite Electrodes. *The Journal of Physical Chemistry C*, 115(16), 8393–8399. doi:10.1021/jp200197d
- ¹¹ de Tacconi NR, Mrkic M, Rajeshwar K. 2000. Photoelectrochemical Oxidation of Aqueous Sulfite on Ni–TiO₂ Composite Film Electrodes. *Langmuir*. 16(22):8426–31

Understanding the Formation of PbS Nanosheets

Kaitlyn A. Perez¹, Haitao Zhang², Jun Yang², and Frank W. Wise²

¹*Department of Chemistry, Bucknell University, Lewisburg, PA 17837*

²*School of Applied and Engineering Physics, Cornell University, Ithaca, NY 14853*

Two-dimensional nanosheets potentially have the capability to be superior in charge transportation while exhibiting quantum confinement. More specifically, lead sulfide (PbS) nanosheets are promising materials for solar cell and infrared light-emission applications. We report here the synthesis of PbS nanosheets via a colloidal synthesis using lead oleate and bis(trimethylsilyl) sulfide (TMS) as precursors. The nanosheets are formed via oriented attachment of PbS nanoparticles. We have revealed that the PbS nanosheets are single crystals, and the thickness of the nanosheets can be tuned by the reaction temperature. With condition optimization, it is plausible that PbS nanosheets can be synthesized with controllable thickness and tunable optical properties, making them attractive for use in solar cell and other applications

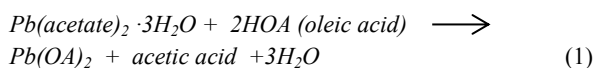
Colloidal nanomaterials have been gaining much attention due to the low cost of their production and the simplicity of their processing.^{1,2} Semiconductor nanomaterials appear promising for integration into electronic and optoelectronic applications due to their size-tunable band gap.³ Semiconductor nanoparticles are usually stabilized using bulky hydrocarbons, which inhibit charge transportation in thin-films made of nanoparticles.⁴ Recently, much effort has been invested in replacing the large, passivating hydrocarbons with shorter organic molecules, halides, and inorganic molecules to improve charge transport in thin films.⁵⁻⁷ Another method for producing thin films with good mobile charge carrying abilities is using two-dimensional nanosheets. Although nanosheets only experience quantum confinement in one dimension, their mobile charge carrying ability is far superior to that of nanoparticles.⁴

Cadmium chalcogenide nanosheets with controlled thickness and tunable optical properties have been well studied.^{8,9} Efforts have been made to synthesize lead chalcogenide nanosheets.^{4,10} Specifically, a colloidal synthesis method has been developed for lead sulfide (PbS) nanosheets, but the result-

ant nanosheets lack uniform thickness and well-defined optical properties.^{4,10}

The work described in this paper is focused on understanding the mechanism of PbS nanosheet formation with a goal of developing a method for synthesizing PbS nanosheets with controllable thickness and tunable optical properties. Such nanosheets are ideal materials for high-tech applications such as solar cells and light emitters.

Weller et al. reported the first synthesis of colloidal PbS nanosheets (*Science*, **2010**, 550). The same synthetic recipe has been used in a number of follow up works (*Klinke et al. APL*, **2012**, 073102; *Siebbeles et al. Nature Communications* **2014**, ASAP). This method uses thioacetamide (TAA) as a sulfur source and lead oleate (Pb(OA)₂) as a lead precursor, which is produced by the reaction:



The acetic acid and H₂O produced via (1) are removed by vacuum, but there is likely residual H₂O and acetic acid in the reaction solution. The thickness of the nanosheets is tunable by using different chlorinated-solvents at different reaction temperatures.

We found that the reproducibility of this method, however, is not good in our tests. The same synthetic recipe of different batches can produce different products of nanosheets or nanoplates. The uncontrollable amount of residual acetic acid in the reaction solution after vacuuming has a significant effect on the reactions. A reaction with 20 minutes of vacuuming produces nanosheet products, while a very low yield of nanoplates is obtained from a reaction with 60 minutes of vacuuming (Figure 1). Extending the vacuuming time also decreases the reactivity of the precursors, which is apparent from the color change of the reaction solutions.

A synthesis was then performed with lead oxide as the lead salt instead of lead acetate, in which acetic acid was excluded. Lead oleate, the lead precursor for nanosheet formation, was produced via:



Only a very low yield of nanoplates (Figure 2A) is harvested in this reaction. Adding a small amount of acetic acid (Pb:acetic acid = 12:1) leads to a faster reaction (*based on the color change of reaction solutions*) that produces nanosheets (Figure 2B). Further studies on the effects of acetic acid and temperature reveal that the high reactivity of the synthetic reactions promotes the formation of nanosheets (Figure 2A-D). If the reactivity is high enough, then nanosheets are formed as seen in Figure 2B and 2D; when there is low

reactivity, nanoplates are formed as seen in Figure 2A and 2C.

As an alternative to increasing the reactivity of the precursors, we used a new sulfur source TMS, which is more reactive toward lead salt for the formation of PbS than thioacetamide (TAA). Using TMS as a sulfur source and PbO as a lead source, PbS nanosheets are produced without adding acetic acid at a variety of temperatures (Figure 3). High Resolution TEM studies (inset of Figure 3C) reveal that the surface of nanosheet is (100) facet. Adding acetic acid to a PbS nanosheet synthesis that has TMS as the sulfur source did not appear to have any beneficial effect.

The chemical yield of nanosheets products increased with decreasing reaction temperature, with a maximum yield of approximately 40% in a 70°C synthesis. This observation is consistent with the formation mechanism of PbS nanosheets reported in literature. According to Weller's studies, PbS nanosheets are formed through a 2-step pathway. The first step of the reactions produces small PbS nanoparticles, which then attach to each other via (110) facets to form nanosheets.¹⁰ In lower temperature reactions, the original nanoparticles will have a smaller size, making them less stable and more likely to have a (110) facet (*(110) facets are unstable and only exist in small size PbS nanoparticles*). These small nanoparticles can attach to each other much more easily than the larger nanoparticles that are produced in higher re-

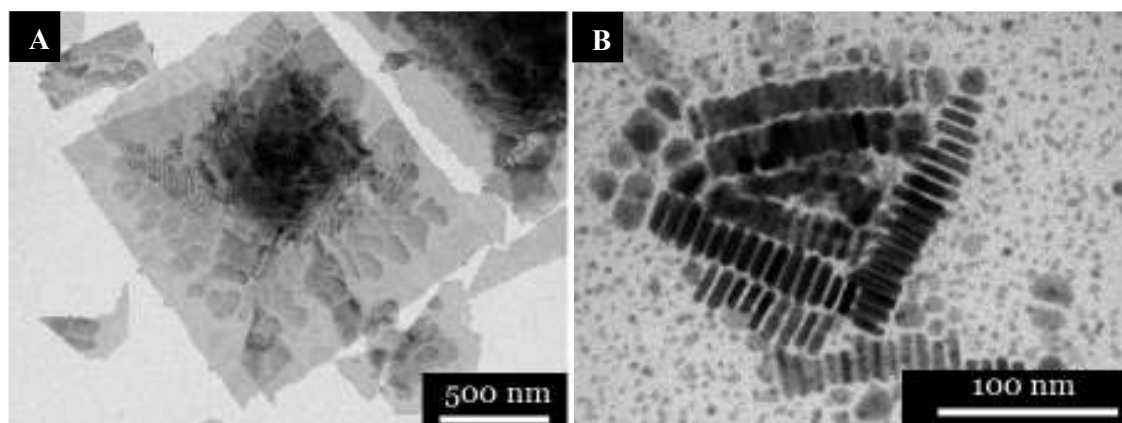


Figure 1: TEM images of products of literature synthesis with 20 minutes (A) and 60 minutes (B) of vacuuming.

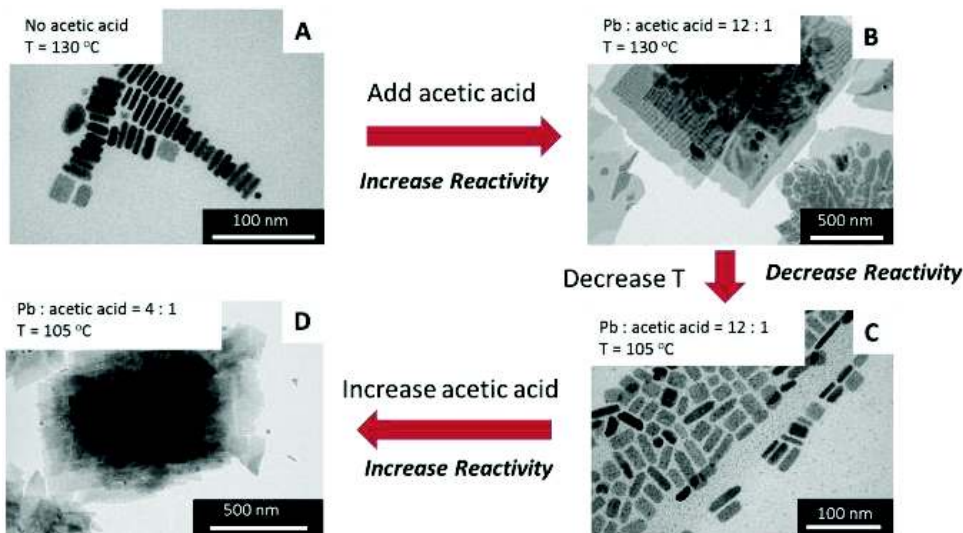


Figure 2: TEM images of products of temperature and acetic acid concentration variations to the synthesis with PbO and TAA.

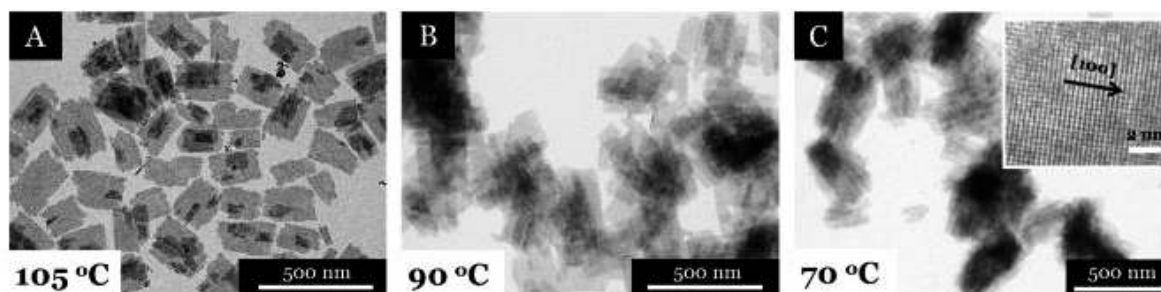


Figure 3: TEM images of products of synthesis with PbO and TMS as (A) 105 °C, (B) 90 °C, (C) 70 °C.

action temperatures.

We also expect that the thickness of the nanosheets will increase with increasing synthetic temperature. The emission spectra, shown in Figure 4A, which display a red shift with increasing temperature, are consistent with increased thickness of nanosheets. More characterization must be done before we can confirm that PbS nanosheet thickness increases with temperature. The absorbance spectra of our nanosheet products, shown in Figure 4B, do not show a clear excitonic peak, which we expect due to the quantum confinement of the nanosheets. This may be due to a lack of uniform thickness in the nanosheets or due to scattering effects. Further studies will be carried out to verify this.

The thickness of the nanosheets synthesized from a typical synthesis with PbO and TMS at 105 °C was measured using

Atomic Force Microscopy (AFM) to be 4 nm, and the surface appears to be relatively uniform (Figure 5). The true thickness of the nanosheets should be less than 4 nm due to the presence of passivating oleic acid ligands on the surface. Additional AFM studies conducted on nanosheets synthesized using a typical synthesis at 90 °C and 70 °C will enable

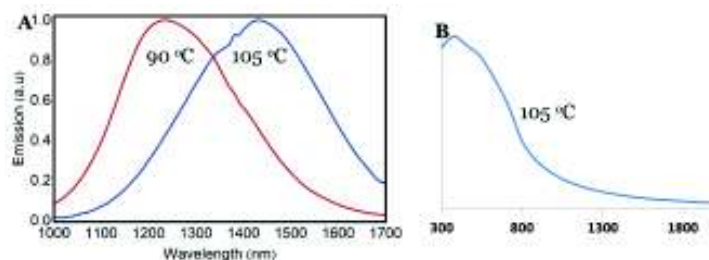


Figure 4: (A) Photoluminescence spectra of PbS nanosheets synthesized from PbS nanosheet synthesis with PbO and TMS at 90°C and 105°C. (B) Absorbance spectrum of PbS nanosheets from a typical synthesis with PbO and TMS at 105°C.

us to determine if the thickness of nanosheet is tunable by synthetic temperature, which we predicted from the emission spectra (Figure 4).

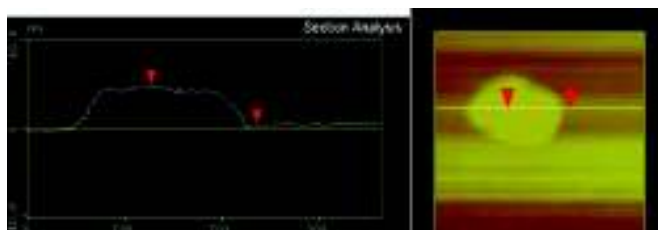


Figure 5: AFM analysis of a single nanosheet synthesized using a typical PbO and TMS synthesis at 105°C.

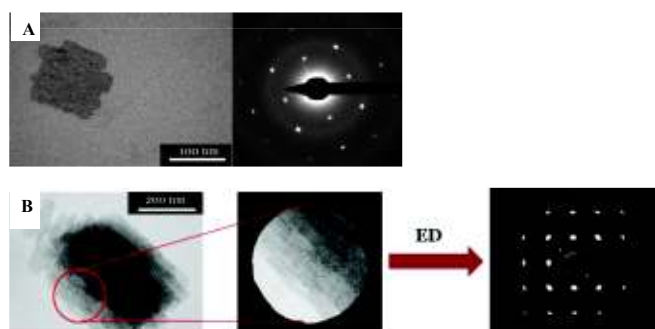


Figure 6: (A) Corresponding TEM image and electron diffraction of a single nanosheet synthesized following a typical procedure with PbO and TMS at 70°C. (B) A TEM image of the section of a stack of PbS nanosheet and the corresponding electron diffraction pattern.

Electron diffraction (ED) studies reveal that the PbS nanosheets synthesized using TMS at 70 °C is single-crystalline. As shown in Figure 6A, the ED image of a single nanosheet exhibits a clear cubic diffraction pattern. Many nanosheets in low temperature syntheses (70 °C and 90 °C, see Figure 3) are within aggregated stacks. It is interesting that nanosheets within a single stack appear to align well based on their electron diffraction pattern (Figure 6B).

Conclusions:

In conclusion, we have elucidated that a small amount of residual acetic acid plays an im-

portant role in a previously reported PbS nanosheet synthesis recipe,¹⁰ and the high reactivity of the synthetic reactions promotes the formation of nanosheets. A new method has been developed to synthesize PbS nanosheets by using a more reactive sulfur precursor TMS. The PbS nanosheets synthesized using TMS were found to be single crystalline and have a relatively uniform thickness. These studies will contribute to the improvement of PbS nanosheets synthesis, allowing for PbS nanosheets to be integrated into solar cells and light-emitting applications.

Experimental:

General Procedures

All of the manipulations were carried out in a N₂ atmosphere by employing standard Schlenk line and glove box techniques.

The conventional transmission electron microscopy (TEM) images were recorded on an FEI Tecnai T12 transmission electron microscope operating at 120 kV. Samples for TEM analysis were prepared by putting a drop of solution containing nanocrystals on the surface of a copper grid coated with an amorphous carbon film. Atomic force microscopy (AFM) measurement was conducted on a Veeco Dimension 3100 Ambient AFM STM. UV-vis absorption data were collected on a Shimadzu UV-3101PC spectrometer. The photoluminescence spectra of PbS nanocrystals were taken by a home built setup, with an Acton spectrometer (SP2300), a Femtowatt IR detector and a lock in amplifier (SR830). Nanocrystals were excited by a 632nm diode laser (CW, 20mW/cm²).

I. Literature synthesis of PbS nanosheets using lead acetate and thioacetamide

In a typical synthesis, 860 mg lead acetate trihydrate (Pb(C₂H₃O₂)₂·3H₂O) was mixed with 10 mL diphenyl ether and 3.5 mL oleic acid. The mixture was heated to 110°C. Once all of the Pb(C₂H₃O₂)₂·3H₂O was dis-

solved, the mixture was vacuumed for 20 minutes to remove water and acetic acid. 1 mL of 1,1,2-trichloroethane was added to the solution at 110°C. The mixture was then heated to 130°C and 12 mg of TAA in a 930 μ L of tri-n-octylphosphine (TOP) and 70 μ L of dimethylformamide (DMF) was injected. After 5 minutes, the reaction solution was cooled down slowly to room temperature, and the products were separated by centrifuge. The nanocrystal products were washed with toluene until the supernatant was colorless. The final products were redispersed in either toluene or tetrachloroethylene (TCE).

II. Synthesis using PbO as lead source and TAA as sulfur source

In a typical synthesis, 506 mg lead oxide (PbO) was mixed with 10 mL diphenyl ether and 3.5 mL oleic acid. This mixture was heated under nitrogen at 110°C. When all of PbO was dissolved, the mixture was vacuumed for 20 minutes to remove water. 1 mL of 1,1,2-trichloroethane was added to the reaction at 110°C. The mixture was then heated to 130°C and 12 mg of TAA in a 930 μ L of tri-n-octylphosphine (TOP) and 70 μ L of dimethylformamide (DMF) was injected. After 5 minutes, the reaction solution was cooled down slowly to room temperature, and the products were separated by centrifuge. The nanocrystal products were washed with toluene until the supernatant was colorless. The final products were redispersed in either toluene or tetrachloroethylene (TCE).

III. Synthesis using PbO as lead source and TMS as sulfur source

In a typical synthesis, 506 mg PbO was dissolved in 10 mL diphenyl ether and 3.5 mL oleic acid at 110°C under nitrogen. The mixture was then vacuumed for 20 minutes to remove H₂O. The temperature was reduced to 105°C and 1 mL of 1,1,2-trichloroethane was added to the reaction solution. 34 μ L of TMS in 930 μ L of tri-n-

octylphosphine (TOP) and 70 μ L of dimethylformamide (DMF) was then injected. After 5 minutes, the reaction was cooled down slowly to room temperature. The product was centrifuged, and the nanocrystal products were washed with toluene until the supernatant was colorless. The final products were dispersed in either toluene or TCE.

Acknowledgements:

This work was supported by the Cornell Center for Materials Research with funding from the Research for Undergraduates program (DMR-1063059 and DMR-1120296). This work made the use of the Cornell Center for Materials Research Shared Facilities which are supported through the NSF-MRSEC program (DMR-1120296).

References:

1. D. V. Talapin, and C. B. Murray, *Science* **2005**, 310, 86.
2. S. A. Claridge, A. W. Castleman, S. N. Khanna, C. B. Murray, A. Sen, and P. S. Weiss, *ACS Nano* **2009**, 3 (2), 244.
3. P.V. Kamat. *J. Phys. Chem. Lett.* **2013**, 4, 908-918.
4. S. Dogan, T. Bielewicz, Y. Cai, C. Klinke, *Appl. Phys. Lett.* **2012**, 101, 073102.
5. J. Tang, K. W. Kemp, S. Hoogland, K.S. Jeong, H. Liu, L. Levina, M. Furukawa, X. Wang, R. Debnath, D. Cha, K. W. Chou, A. Fischer, A. Amassian, J. B. Asbury, E. H. Sargent, *Nature Mater.* **2011**, 10, 765.
6. Y. Cai, D. Wolfkuhler, A. Myalitsin, J. Perlich, A. Meyer, C. Klinke, *ACS Nano* **2011**, 5, 67.
7. H. Zhang, B. Hu, L. Sun, R. Hovden, F. W. Wise, D. A. Muller, R. D. Robinson, *Nano Lett.* **2011**, 11, 5356.
8. S. Ithurria, M. D. Tessier, B. Mahler, R. P. S. M. Lobo, B. Dubertret, Al. L. Efros, *Nature Mater.* **2011**, 10, 936.
9. C. She, I. Fedin, D. S. Dolzhenkov, A. Demortière, R. D. Schaller, M. Pelton, D. V. Talapin, *Nano Lett.*, **2014**, 14 (5), 2772.

10. C. Schliehe, B. H. Juarez, M. Pelletier, S. Jander, D. Greshnykh, M. Nagel, A. Meyer, S. Foerster, A. Kornowski, C. Klinke, H. Weller, *Science* **2010**, 329, 550.

The Effect of Hydrodynamic Shear Stress on the Proliferation of *Dictyostelium discoideum*

Eric Rice, Dept. of Chemical Engineering, University of Massachusetts Amherst

Advisor: Carl Franck, Laboratory of Atomic and Solid State Physics, Cornell

University

CCMR REU

8 August 2014

When cells are transferred to shaken suspension culture, they may experience a phase of slow growth, called the Lag phase. Upon reaching a critical cell density, slow growth is followed by a period of exponential growth. The transition from slow to exponential growth is known as the lag-log transition. Understanding how cells interact at a low density and why this transition occurs, may provide important mechanisms behind modes of proliferation. This understanding could lead to advancements in cell biology techniques, population ecology models, and medicine. The focus of this paper was on understanding how varying stir rate of suspension culture affects this Lag-Log transition and the growth behavior of *Dictyostelium discoideum*. If the Lag-Log transition could be explained by cell-to-cell contact, one would expect the rate at which cells are stirred would affect the collisions of cells, hence affect the lag-log transition. Varying stir rates of suspension culture resulted in unexpected growth behavior, and no conclusion regarding variation in lag-log transition could be conveyed. This resulted in the cell-contact hypothesis to be disregarded due to a limited sample size. An unconventional mixing system was used to quantify shear forces present in the suspension culture of *D. discoideum*. The system demonstrated that inertial flows provided by orbital shaking are not necessary for the proliferation of *D. discoideum*. A theoretical model was next implemented in attempt to describe the formation and fracture of cell aggregates in suspension. Both the formation and fracture of clusters depended on the stir rate. The cell clustering model could not accurately describe the experimental data obtained. A future, improved model may still be able to replicate experimental results. A possibility remains, that Dicty is more sensitive to forces than previously understood.

I. INTRODUCTION

i. The Lag-Log Transition

Suspension culture, a cell culture technique where cells and cell aggregates are growing in a moving liquid medium, provides the benefit of observing multicellular growth from a low cell density. Axenic strains of *D. discoideum*, a NIH model organism, proliferate in suspension without the necessity of any other organisms. In biology literature, cells must adapt to the new environment when they are moved to suspension culture at low densities.¹ Cells may undergo a growth phase characterized by little to no growth, called the lag phase. The lag phase growth behavior is often observed when axenic strains of *D. Discoideum*, are cultured in suspension.

Upon reaching a critical density, cells will enter into a period of exponential growth known as the log phase. The familiar lag-log transition has been commonly observed in cell culture across a range of fields, but little effort has been put into understanding this transition. Instances similar lag-log transitions can also be seen in population dynamics, tumor growth kinetics.² Understanding the mechanism behind this transition may contribute to problems in these areas.

Experiments show *D. discoideum* reaches a crossover from lag to log growth at a critical cell density of 10^4 cells/ml.³ There is also evidence of great variability in this transition: upon observation of many growth curves, one will find that *D. discoideum* may spend an extended period of time in the lag phase or experience no lag phase growth at all. The transition may be the product

of a collective effect. The cells may be able to communicate their density through collisions. Another possibility is that the time for transition is inherent between different groups of cells.

ii. Cell Contact Theory

If cells are able to communicate their density through collisions, one would expect a change in growth behavior when varying the stir rate of suspension. As the stir rate increases, the number of cell collisions will also increase. If a critical number of collisions characterize a cell's transition from lag to log phase growth, one would expect an increasing stir rate would cause the cells to enter into the log growth phase sooner (Figure 1).

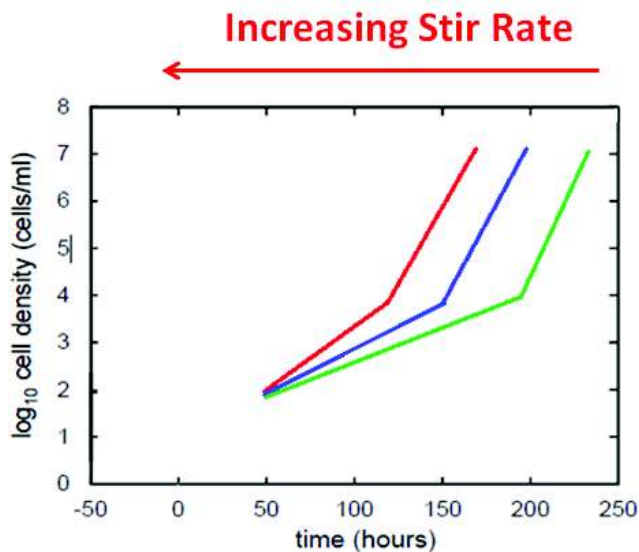


Figure 1: Illustration of the cell contact theory. The red line illustrates the highest stir rate. The green line illustrates the slowest. As stir rate increases, the lag-log transition is expected to occur faster.

iii. Cell Clustering Theory

When culturing cells in suspension, it is important to consider the formation of biofilms, in which a matrix of cells (or microbes) adheres to biological or non-biological surfaces. *D. discoideum* is “sticky” and clusters of cells will always exist in suspension. Clusters of cells are often observed under an optical microscope. Formations of biofilms represent a protective mode of growth believed to provide many growth advantages.⁴ It is possible that single cells proliferate at different rates than cells which are a part of an aggregate.

One may realize that stirring acts twofold on the formations of these clusters. Stirring can effectively create a cluster of cells by bringing together two cells together, creating a biofilm. Stirring also effectively destroys clusters of cells when shear forces act on a cluster of cells.

iv. Summary of Purpose

The main purpose of this paper is to explore the lag-log transition seen by *D. discoideum* when varying the stir rate in suspension culture. If this phenomenon could be explained through cell-to-cell contact, varying the stir rate would affect the number of collisions cells experience, hence likewise affect the lag-log transition. Cell aggregates present in suspension may also undergo a different mode of growth than single, free floating cells. Lastly, *D. discoideum* may “feel” shear forces in suspension culture which causes a decreased growth rate across all growth phases. All three thoughts: a cell-to-cell contact theory, a cell clustering theory, and *D. discoideum*'s innate sensitivity to shear are explored.

Shaken suspension culture is complicated by inertial flow, driven by the momentum of the fluid as it flows around the container. Therefore, this system was simplified to a shearing system dominated by friction flow. Inertial flow was eliminated for two reasons. First, the removal of complex inertial forces would simplify the type of forces “felt” by the cells, which is preferred when designing a system. The second reason was to question the necessity of inertial flow when culturing *D. discoideum*. Protocol requires inoculating axenic culture at 180 rpm on an orbital shaker.⁵ Our experimental goal was to observe how cells would respond to this novel mixing approach.

II. RESULTS AND DISCUSSION

i. Variable Stir Rate Experiment

The stirring in this experiment was characterized by shear forces. *D. discoideum* thrived quite well without the need of inertial forces. It is also important to note the crossover from lag phase growth to log phase growth. It is impossible to determine whether there is a transition for the 400 rpm sample; however the 48 rpm and 65 rpm samples experienced a transition much earlier than expected (Figure 2).

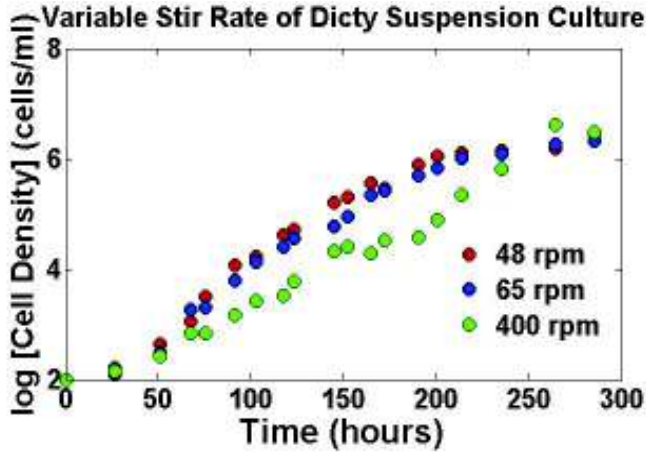


Figure 2: The graph displays the growth curves of *D. discoideum* at varying shear rates. The circles correspond to stir rates of 48 (red), 65 (blue), and 400 rpm (green). A significant difference of growth behavior is observed between the 48 rpm and 400 rpm sample.

The experimental transition here can be seen between 10^2 and 10^3 cells/ml, which diverged from previous experimental results of 10^4 cells/ml. An insufficient volume of data prevented comment on a potential relationship between the variation in the lag-log transition. The absence of this necessary data required us to discount the cell-to-cell contact theory. Another significant characteristic of this data was the lack of explicit exponential growth in the log phase. The log phase growth curve seems to dampen as the forces increase. The cells were expected to exhibit purely exponential growth in this phase; however the mixing forces may be causing stress to the cells. The force “felt” by *D. discoideum* may be slowing the proliferation of the cells. Lastly, when compared to previous experiments, the log growth phase tails off into the stationary phase sooner than expected.

ii. Cell Clustering Theory - Model

The unexpected proliferation behavior seen in the variable stir rate experiment may still be explained through the cell clustering theory. The formation of a biofilm can be associated with growth advantage, and this led us to the assumption that cells grow better in clusters. Here we defined two terms, the growth rate of cells in clusters g_f , and the growth rate of single cells g_s . To eliminate the number of independent variables we assumed the ratio

$$g_f/g_s = 2 \quad (2.1)$$

when averaging the growth rates in both the lag and log phase of previous experimental data.

The system designed in the variable stir rate experiment, efficiently eliminated complex inertial flow. The system was characterized by shear flow, friction dominated flow. We could define our simple system through a linear shear as a function of radial distance. Our system experienced a constant shear force

$$S = 2\pi l f / (R - l) \quad (2.1)$$

where r is defined as half the length of the stir bar and R defined as the radius of the container. These two values remained constant, and varying the stirring frequency determined the amount of shear stress on the system.

As previously stated, fluid-mechanical forces impact the collision rate of cells, hence the rate at which cells join into aggregates, as well as how quickly cell aggregates disperse. This led to the creation of two terms. Flocculation rate, ν , was defined as the reversible action of aggregate formation directly proportional to the shear

$$\nu \propto S \quad (2.2)$$

stress. The rate at which cells fall out of clusters, $\beta(S)$, was also a function of shear stress.

$$\beta(S) = \frac{16}{3} a S \quad (2.3)$$

Beyond a critical shear force, S_c , cells would experience a shear force greater than the potential energy of the forces holding them together. Using equation 2.1, this critical threshold was assumed exist at 180 rpm because this was the suggested protocol for the best proliferation of *D. discoideum*. If the shear force was below this critical threshold, $\beta(S)$ would be turned off. A Heaviside function was used to exhibit this behavior.

The growth rate of single cells is shown

$$\dot{N}_s = \beta(S)N_c - 2\nu(S)N_s^2 + g_s N_s \quad (2.4)$$

and the growth rate of cells in clusters is shown

$$\dot{N}_c = -\beta(S)N_c + 2\nu(S)N_s^2 + g_c N_c \quad (2.5)$$

where \dot{N}_s and \dot{N}_c denote the number of single cells and the number of cells in clusters. We would like the units to be in cell density so we divide by the volume of the solution of cells

$$\dot{N}/V = \dot{N}_s/V + \dot{N}_c/V \quad (2.6)$$

This equation was solved and plotted (Figure 3).

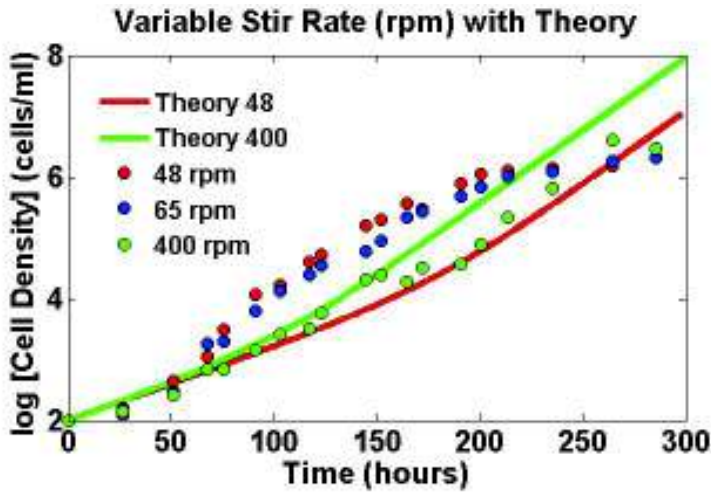


Figure 3: The red and green solid lines represent the modeled theory curves at 48 and 400 rpm. Agreement between experiment and theory is not observed. Cluster formation seems to dominate the system as stirring frequency increases. The rate at which cells are sheared apart is not fast enough to combat the speed at which clusters are formed.

IV. MATERIALS AND METHODS

i. Axenic Cell Culture

Axenic strain, AX4 of *D. discoideum* was used in all experiments. Three sources of cells had been thawed and cultured from frozen stock dating from March 5, 2012, March 7, 2014, and March 17, 2014. Cells were cultured following typical axenic culture protocol.⁶

ii. Variable Stir Rate Experiment

Previous experiments have examined the effects of stirring on the growth behavior of *D. discoideum*.⁷ The goal of this experiment was to obtain as wide of a range as possible in hope of elucidating a sudden range of

interest. The setup of this experiment focused on carefully eliminating variables which could cause extrinsic fluctuations in the growth of *D. discoideum*.

Stirrers were set to a wide range of stirring frequencies. No deviations appeared after frequencies were set. Temperature was controlled. Prior to the experiment, sample tests were conducted using water. A Fisherbrand® spinbar and a 2 oz. flat bottomed specimen vial with a removable (pop-off) plastic cap were used as the suspension culture vessel. The axenic strain from March 17, 2014 was used in this experiment. This setup provided a system dominated by shear flow.

Sterility preparation took place as follows. All vials, caps and stir bars were individually rinsed with 65% isopropyl alcohol (IPA). Throughout the entire drying process, the UV lights were turned on. Excess liquid was dried off stir bars as they were placed into a single dry vial. Caps and 2 oz. vials were next dried with compressed air. The vials were placed upside down on top of the dried caps which sat on a sterilized surface. The solution of cells was then added to each vial individually.

Attention was brought to followed protocol upon the discovery of an infection in one of our samples (data not shown). This was later improved in three subsequent experiments. Any suspected contamination could bring about extrinsic variability which would mask the true growth behavior of the cells. It was suspected that bacteria in the air may be finding its way into the samples. In the subsequent experiment protocol flame was waved in front of the lip of the container, a common technique used in microbiology. This technique created a vacuum which attempted to eliminate airborne bacteria and fungal spores from entering the container.

V. CONCLUSION

A close observation of the growth curves, provided by both the experimental and theoretical data, rule out mechanisms behind the growth behavior observed. Unexpectedly, a variation of the observed lag-log transition was not observed. Evidence supports neither for nor against a variation in the transition; and more data is necessary to make further conclusions. From this conclusion we sought to determine how strong these shear forces were in regards to the organism's ability to "feel" forces.

After performing a calculation (not shown) using equation 2.1, it appears as though *D. discoideum* is not affected by the shear forces (within the observed experimental range) in suspension culture. The minimum force “felt” by *D. discoideum* was experimentally found to be between 0.1 Pa and 0.7 Pa.⁸ This is a factor of three less than the calculated shear force of a 1200 rpm sample. Another consideration is that *D. discoideum* is more sensitive to forces than previously demonstrated. This could potentially agree with the variable stir rate experiment; as the log phase growth curve is expected to dampen as the forces increase.

The setup of the variable stir rate experiment answers the question of inertial flow in traditional cell culture methods. The system demonstrated that inertial forces provided by orbital shaking are not necessary for the proliferation of *D. discoideum*. The cells thrived even when inertial forces were replaced by shear forces. This finding calls us to question the science behind conventional protocol.

Currently, the theory of cell clustering does not accurately describe the experimental data obtained in the variable stir rate experiment. It has been stated that fluid-mechanical forces will change the rate of collisions of cells, as well as how quickly cell aggregates disperse. The created model suggests the clustering of aggregates wins out over single cells. The model illustrates that the shear rate is simply not fast enough to shear apart clusters. However, when observing *D. discoideum* under an optical microscope, one will find that clusters are not as prevalent as this model proposes. Although this rough theory does not accurately describe the experimental data, a more refined theory has the potential to provide further insight into the growth behavior of *D. discoideum*.

VI. FUTURE DIRECTIONS

Previously we concluded that *D. discoideum* may be more sensitive to forces than previously demonstrated. Further experimentation regarding this will help elucidate further understanding of growth behavior.

The model also raises question over the critical shear threshold and the amount of energy holding two cells together. Further light scattering experiments could provide valuable data on cluster formation. Making use of mutants and/or chemical compounds which inhibit cluster formation are also necessary to expose new ideas

regarding the energy between two cells, how quickly cell aggregates disperse, and how clusters affect the growth dynamics of the log phase.

VII. ACKNOWLEDGEMENTS

Support for the REU program is provided by the NSF MRSEC program (DMR-1120296) and the REU Site program (DMR-1063059)

*erice@umass.edu

¹Torrey, John G., Jakob Reinert, and Nancy Merkel. "Mitosis in Suspension Cultures of Higher Plant Cells in a Synthetic Medium." *American Journal of Botany* 49.4 (1962): 420-25. Print.

²Zhang, Ming, Chandra Das, and Hernan Vasquez. "Predicting Tumor Cell Repopulation After Response: Mathematical Modeling of Cancer Cell Growth." *Anticancer Research* 26 (2006): 2933-936. Web.

^{3,7,3} Franck, Carl, Wui Ip, Albert Bae, Nathan Franck, Elijah Bogart, and Thanhbinh Thi Le. "Contact-mediated Cell-assisted Cell Proliferation in a Model Eukaryotic Single-cell Organism: An Explanation for the Lag Phase in Shaken Cell Culture." *Physical Review E* 77.4 (2008): n. pag. Web.

⁴Hall-Stoodley, Luanne, J. William Costerton, and Paul Stoodley. "Bacterial Biofilms: From the Natural Environment to Infectious Diseases." *Nature Reviews Microbiology* 2.2 (2004): 95-108. Web.

⁵, ⁶"Protocols for Growing Dictyostelium Discoideum." *Dictyostelium Growth*. N.p., n.d. Web. 04 Aug. 2014.

<http://dictybase.org/techniques/media/dicty_growth.html#axesus>.

Graphene Dry Transfer with a PDMS Stamp

Carlos J Sanchez¹, Bryce Kobrin², Peter Rose², Paul McEuen^{2,3}

Department of Mechanical Engineering, University of Puerto Rico, Mayagüez, PR¹,

Laboratory of Atomic and Solid State Physics, Cornell University, Ithaca, N.Y.²

Kavli Institute at Cornell for Nanoscale Science, Cornell University, Ithaca, N.Y.³

Abstract:

Interest in the field of two-dimensional materials has grown tremendously since the discovery of the first 2D material, graphene. In order to study graphene accurately, the transfer process cannot contaminate or tear the sample. To come closer to this goal, we worked in collaboration with the Hone Group at Columbia University to adapt to our needs a transfer technique that they have recently developed. This new technique can transfer graphene grown by chemical vapor deposition. The purpose of this technique is to better preserve the quality of the graphene. Using this technique the size and number of cracks was greatly reduced as compared to other transfer techniques used.

It has been known that graphene existed since it is the building layers that make up graphite. The challenge consisted of how to isolate it. In the year 2004, when the first isolation of a single graphene sheet was performed, it opened up a new field of two-dimensional materials (1). Graphene, being just one atom thick, brings a wide range of opportunities, but also its own challenges. The problems result from the difficulty of protecting an atom-thick material from rupturing and from contamination during the transfer process.

The quality of the graphene sample used for experiments impacts the data acquisition success ratio. The transfer procedure becomes a crucial step in graphene research due to the possibility of affecting the subsequent steps. Wet transfers are a common technique in research, but this type of transfer can cause several defects on the graphene. The several rinses it undergoes to clean the sample can produce enough strain forces that can rupture the uniform layer. The graphene is spin-coated with a ~100nm layer of polymethyl

methacrylate (PMMA) that is constantly exposed to the air, which can accumulate different contamination agents that can impact the graphene once it is dissolved.

A dry transfer technique addresses some of the problems found in wet transfers. The new technique reduces the rinsing steps to just one, minimizing the strain forces. The PMMA exposure to the air is limited by being in contact with a polydimethylsiloxane (PDMS) layer that can block the contaminants. The PDMS will also give the sample more structural rigidity lowering the probability of cracks occurring. Overall, this should give a higher yield rate among the fabricated devices.

Protocol:

The dry transfer technique is composed of three main elements: graphene on copper foil, a polydimethylsiloxane (PDMS) stamp, and the target final substrate cleaning and adhesion.

Graphene sample

The first step is to grow a large area graphene. Chemical vapor deposition is the best process to synthesize a good uniform layer growth of graphene (2). The graphene has been spin-coated with a ~100nm layer of PMMA, which enhances the graphene by slightly increasing the rigidity (3). A complete growth is necessary to be able to transfer a constant layer of graphene to the final substrate. Holes in the layer may prevent future devices from working properly. The copper foil containing the graphene should also be as flat as possible to prevent cracks from forming before the beginning of the transfer process. Throughout the process, care should be taken to protect the graphene sample from air when the sample is not in use. This will reduce the amount of contaminants that can affect adhesion during the transfer process.

The PDMS Stamp

The PDMS stamp will act as the rigid structure that will prevent the sample from bending, folding, and twisting while moving and rinsing the graphene. The stamp consists of a PDMS piece larger than the copper sample and the glass slide that it will be attached to during the etching process for better handling.

First, clean a glass slide with isopropanol alcohol (IPA) and dry it with nitrogen. Cut a PDMS piece that is slightly bigger than the area of graphene that is going to be transferred. A larger piece of PDMS facilitates the process of peeling it off from the final substrate later. Next step is to carefully adhere the piece of PDMS to the glass slide. There should not be any air

pockets between the glass slide and PDMS piece.

A flat sheet of copper with graphene, PMMA side up, should be placed on a clean surface. The PDMS should be gently pressed down onto the copper, with just enough pressure to cause adhesion. This step has to be done carefully to avoid cracking the graphene layer.

The PDMS stamp should be placed in the copper etch until there is no visible traces of copper. Afterward, the rinsing of the PDMS stamp is performed by placing the stamp in a dish filled with DI water, then letting DI water run continuously over the stamp for approximately 5 - 10 minutes. Finally rinse the stamp with IPA and gently use nitrogen to dry it.

Final Substrate cleaning and adhesion

The final substrate should be as clean as possible for it to have the best adhesion. The final substrate is cleaned with acetone, IPA, and oxygen plasma, in that particular order. Oxygen plasma is the crucial step because it cleans the substrate most thoroughly. It should be plasma cleaned for more than 5 minutes to get a good, clean substrate. Following the cleaning process, the PDMS has to be carefully peeled off from the glass slide and stamped onto the final substrate without forming any air pockets inside the seal. To ensure there are no air pockets between the graphene and the final substrate, place the sandwich on the desiccator for 20 minutes.

Heat the hot plate to 120°C and place the sandwich on the hot plate for at least ten minutes. A good indicator of when to peel the PDMS off of the final substrate is when the graphene/PMMA is hard to distinguish.

Carefully peel the PDMS off of the final substrate from one side to the other.

Put the final substrate that has graphene spin-coated with PMMA in Acetone for 6 to 12 hours to dissolve the PMMA. The final result should be graphene on top of the final substrate.

Results:

The dry transfer technique resulted in large areas where there is a uniform layer of graphene without any holes. Other areas of the samples have small holes or ruptures.

Figure 1:

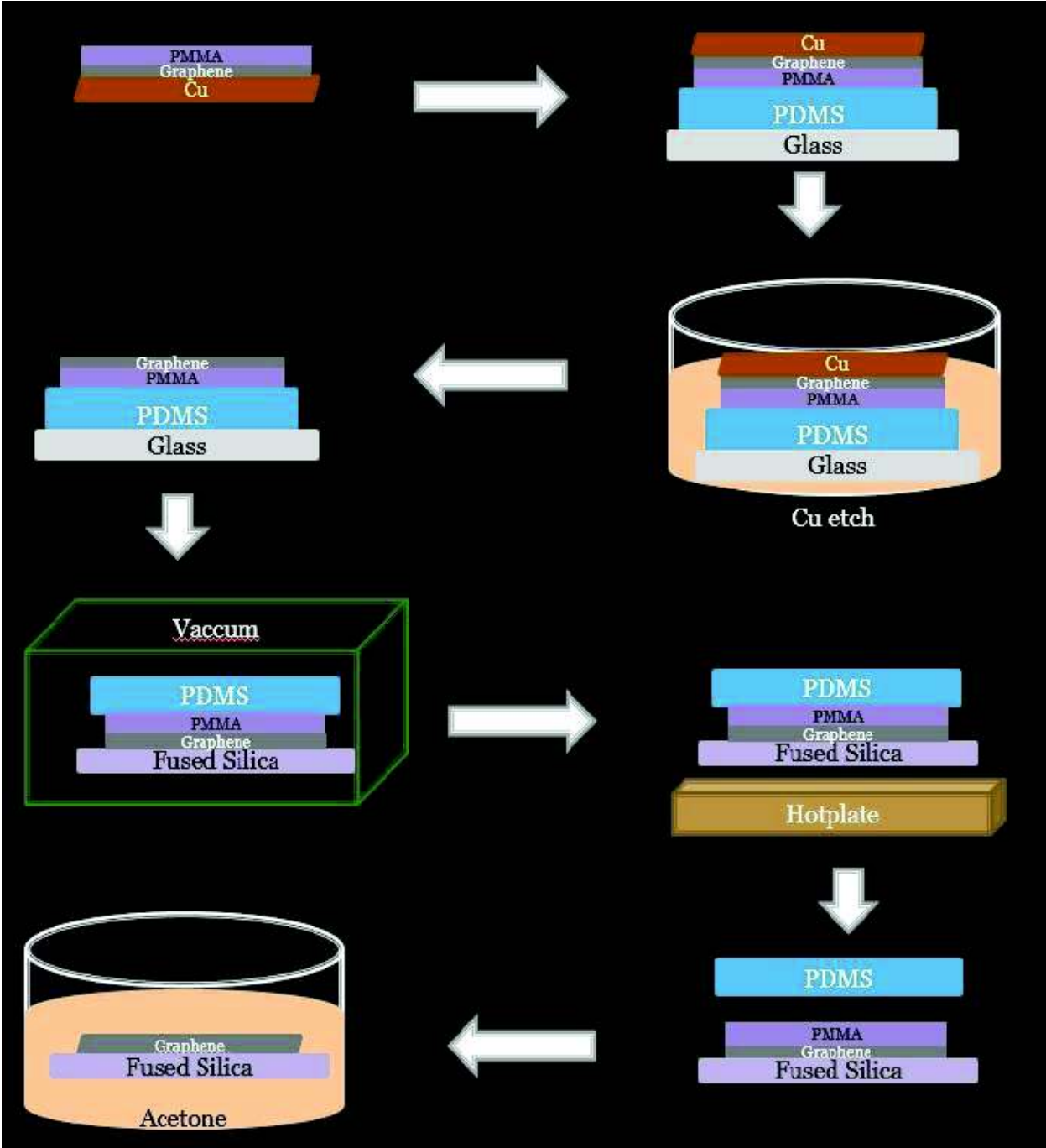


Figure 1: Cartoon representation of the dry transfer technique explained above

These areas with no defects were commonly found near the middle of the samples. However, areas near the edges of the

practical than other techniques. A wet transfer technique has a size limitation due to the handling process involved. This PDMS dry

Figure 2:

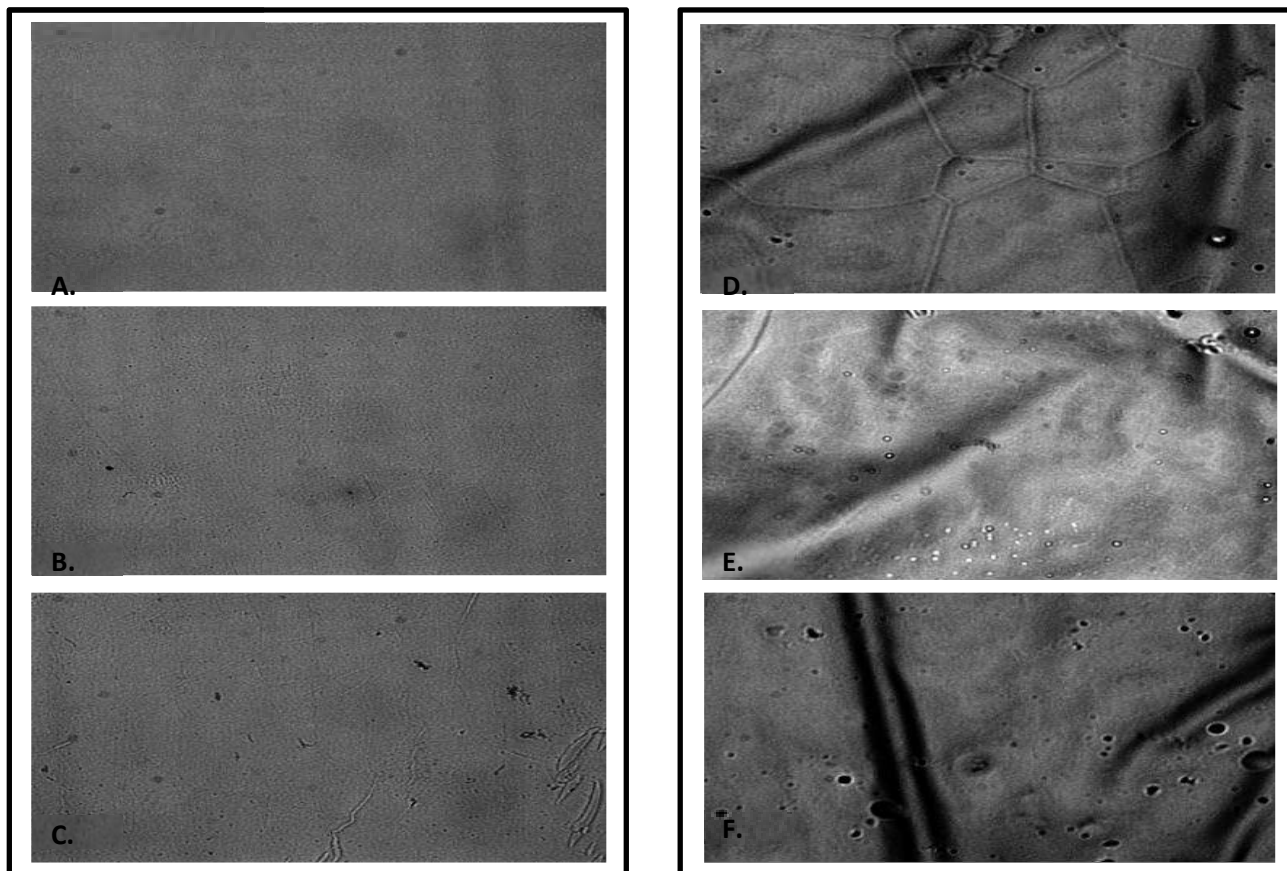


Figure 2: These are all optical images of graphene transferred to their final substrate. The images to the left were transferred using the dry transfer process, A) exhibits a defect free uniform layer of graphene, B) minor defects can be seen on the image. Image C. has the highest amount of defects from the dry transfer process. To the right there are the images taken from a wet transfer process, D) shows several places where contamination exists and several folds. E) It is filled with small cracks on the graphene surface and F) shows the most noticeable folds and contamination from the wet transfer technique.

sample showed the presence of cracks or small holes. The cracks near the edges can be caused by the cutting of the copper foil with a razor blade. When compared to a wet transfer the number of defects has been greatly reduce.

The PDMS transfer technique is one step closer to making wafer size transfers. Since having a rigid structure for graphene support makes transferring larger areas of graphene more

technique opens doors to future transfer methods. The PDMS layer acts as the supporting rigid structure that prevents graphene from rupturing. This will allow researchers to put different layers of materials that can substitute the PMMA on the graphene. Eliminating the PMMA benefits the whole process because it is a difficult material to dissolve, and it often leaves residue. A possible

substitute can be gold, which has a cleaner dissolving process.

Figure 2 contains optical microscope images of graphene once it has been transferred to the final substrate. The left images were graphene transfers done with the dry transfer technique, while to the right were transfers done with a wet transfer technique. It is clear that the dry transfers' images have an overall reduced number of defects compared to the transfer images on the right. The wet transfer images display folds, contamination, and ruptures that ultimately affect the quality of the graphene.

Defects will always exist when using the dry transfer technique. The main purpose of this

dry transfer technique is to reduce those defects in a way that can improve the quality of the graphene. The fabricated graphene devices' performance is ultimately dependent on the quality of the graphene of which they are made.

Acknowledgements:

This work made use of the Cornell Center for Materials Research Shared Facilities which are supported through the NSF MRSEC program (DMR-1120296)

Special thanks to Arend van der Zande for helping us adapt the dry transfer technique to our needs.

References:

- 1 K. S. Novoselov, A. K. Geim, S. V. Morozov, D. Jiang, Y. Zhang, S. V. Dubonos, I. V. Grigorieva, and A. A. Firsov, *Science* 306, 666 (2004).
- 2 X. Li, W. Cai, J. An, S. Kim, J. Nah, D. Yang, R. Piner, A. Velamakanni, I. Jung, E. Tutuc, S. K. Banerjee, L. Colombo, R. S. Ruoff, Large-area synthesis of high-quality and uniform graphene films on copper foils. *Science* **324**, 1312–1314 (2009).
- 3 Xuelei Liang, Brent A. Sperling, Irene Calizo, Guangjun Cheng, Christina Ann Hacker, Qin Zhang, Yaw Obeng, Kai Yan, Hailin Peng, Qiliang Li, Xiaoxiao Zhu, Hui Yuan, Angela R. Hight Walker, Zhongfan Liu, Lian-mao Peng, and Curt A. Richter, Toward Clean and Crackless Transfer of Graphene. *ACS Nano* **2011**, 5 (11), 9144–9153

Supplementary:

PDMS

The PDMS batch was made using Sylgard® 184 Silicone Elastomer Kit, following the mixing ratio suggested by the manufacturer, Dow Corning Corp. The ingredient was then stirred continuously for ~ 10 minutes to allow for the best possible dilution. The next step is to pour into a glass or plastic petri dish the approximate amount that will give a thickness of 1mm when baked. The glass petri dish was then put in a desiccator for at least 20 minutes to remove the air pockets from the PDMS. Afterwards, the hot plate was heated to 60-80°C, and the glass petri dish was put on top for 6 hours.

Electrical Measurement of Domain Walls in Permalloy Nanowires

Caleb Zerger¹, Jason Bartell², Darryl Ngai³ and Gregory Fuchs²

¹Department of Physics, University of Michigan, Ann Arbor, MI 48638

²Department of Applied and Engineering Physics, Cornell University, Ithaca, NY 14853

³Department of Physics, Cornell University, Ithaca, NY 14853

ABSTRACT: Domain walls in Permalloy nanowires are a subject of interest in science and technology, but repeatably localizing these domain walls can be difficult. This paper describes a method of creating and positioning domain walls in a 30×500 nm nanowire. A measurement of anisotropic magnetoresistance (AMR) was then made in an attempt to locate the nanowire. However, no AMR signal was seen, suggesting a domain wall was not properly positioned as expected.

1. Introduction

Domain walls, a region of a material where areas of opposing magnetization meet, have long been a subject of interest in physics¹. The possibility of domain wall application in dense memory storage devices or other electronics has increased interest in recent times^{2,3}. Much of the recent work on domain walls has involved nanowires^{2,4}. These nanowires are appealing for the study of domain walls for several reasons. In thin submicron wires composed of soft ferromagnetic material such as Ni₈₁Fe₁₉ (permalloy), the magnetization is limited mostly to the plane of the wire. Nanowires are also well-suited for carrying current, and offer the opportunity to study the interaction of domain walls with spin current, spin waves, and spin torque oscillators. Domain walls in these structures typically take on one of two geometries: a transverse wall or a vortex wall. Transverse walls, which this paper will focus on, are walls where the magnetization rotates transverse to the wire axis in the film plane as it connects the two opposing magnetic domains. These have been extensively modelled in previous work¹.

An appealing way to study domain walls in nanowires is through magnetic microscopy using the anomalous Nernst Effect. This has the advantage of offering a picture of domain wall structure, as well as a precise location of the do-

main wall within the wire. The disadvantage is that the microscope can only image a very small area at once, making an unguided search for domain walls time consuming. This paper will describe a procedure to create and move a domain wall to a preselected region, and then verify its presence position using electrical measurements. These electrical measurements are useful as they allow an efficient method of roughly locating a domain wall, and are thus complementary to precise but painstaking microscopy. This paper will describe the experimental set up for electrical measurements, as well results of initial attempts to create and position the domain walls using an applied magnetic field and current pulses.

2. Experimental

The experimental set up was designed to enable measurements of anisotropic magnetoresistance (AMR) in the sample. AMR is an effect in which the angle between the magnetization and the current through a wire causes a change in resistance, with resistance being lowest when the magnetization and current are transverse. The resistivity ρ as a function of the angle θ between the magnetization is given by equation (1).

$$R(\theta) = R_0(1 + \Delta R \cos^2(\theta)) \quad (1)$$

Equation (1) indicates that the presence of a transverse domain wall will cause a small but de-

tectable drop in resistance. The setup and procedure exploit this fact to detect the presence of a domain wall between the electrical contacts.

2.1 Equipment and Setup

The samples used for the experiment were 500 nm wide and 30 nm thick permalloy nanowires. Past work has also demonstrated domain walls in wires of this size and material⁴. The wires contain a bend with the lower part of the wire bent back slightly so that the angle is less than 90°. Six copper contacts touch the wire at different points, offering the ability to source current or measure voltage between different points on the wire (See Figure 1).

The necessary contacts, two at the ends for sourcing current and two in the middle to measure voltage, are wire bonded to a chip carrier in which the sample sits. The chip carrier is connected to a Keithley 2401 source-meter equipped for four wire measurement. The chip carrier is positioned at the center of an electromagnet constructed by the group.

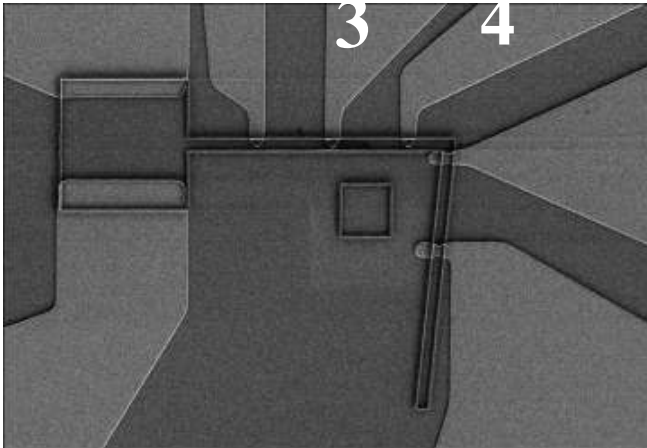


Figure 1: 500 nm nanowire with contact pads. Pads 1 and 2 are used to source current, while 3 and 4 are used to measure resistance between the part of the wire of interest.

2.2 Initial AMR Measurements

An AMR measurement to determine ΔR for permalloy was performed using a 2- μm permalloy wire. The resistance was measured between contacts 3 and 4 as shown in Figure 1, and the magnetic field was swept from -345 to 300 G. The maximum value of resistance occurred at 0 G and 51.618 \pm .006 Ω . The minimum was 51.05 \pm .006 Ω at -345 G. As Figure 2 shows, the magnetization nears but does not reach full saturation transverse to the current direction.

Nevertheless, a lower bound on ΔR is calculated by dividing the difference in the maximum and minimum values of resistance and dividing by the minimum value. For our Permalloy samples $\Delta R \geq$

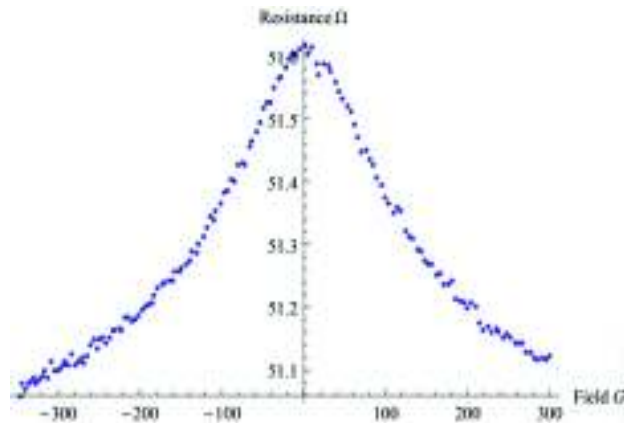


Figure 2: AMR measurement for 2 μm Permalloy wire showing resistance of the sample between contacts 3 and 4 versus a magnetic field varied from -345 to 300 G. The resistance change due to AMR is $> 1\%$ of the total resistance.

0.011.

A simple model of the 500 nm wire was used to calculate the expected AMR signal due to the domain wall by adding up the expected contribution to the resistance between the two contacts at each point along the wire, and using estimates of the domain wall size and geometry. This calculation suggests that the signal due to a domain wall (ΔR_{DW}) should be 7% of ΔR , so $\Delta R_{DW} \geq 0.00077$, or 0.077%.

2.3 Creating a Domain Wall

Creation of the domain wall was accomplished using the applied magnetic field. The 500 nm wire was placed at the center of the electromagnet with the main wire axis (part A of the wire as shown in Figure 1) along the axis of the magnet. The field is then ramped up to over 500 G, causing the magnetic moments in the wire to orient along the field direction. Due to the positioning of the wire, this causes the magnetization to be along the wire axis in part A, but not in part B. The field is then brought down to 0, and the magnetization will want to align with the wire axis⁵ causing the magnetic moments in part B to point up the wire towards the bend, and thus oppose the magnetization from part A, creating a domain wall at the bend.

While this is simple method for creating a domain wall, it is problematic because it does so

only at the bend. Studying a domain wall at the bend is difficult, because the altered geometry of the domain wall is more complicated than it is along the a straight region of the wire. Other magnetic effects could also change the domain wall behavior. Ideally, the domain wall would be moved to a location in part A of the wire, necessitating a method of moving the domain wall.

2.4 Pulsed Current for Current-Induced Domain Wall motion

Current-induced domain wall motion (CIDWM) has been studied often but is still not entirely understood¹⁻³. As the name suggests, it is a phenomena in which a current passing through a domain wall causes the domain wall to move, due partly to angular momentum transfer from conduction electrons to the domain wall¹. In order to move the domain wall from the bend to part A of the wire, CIDWM was used.

A certain threshold current j_t is required to depin a domain wall once it is formed and cause it to propagate. Yang and Erksine at the University of Texas at Austin worked with CIDWM in permalloy nanowires 30×500 nm in size as well. Their work found the experimental threshold current $j_t = 3.9 \times 10^{11}$ A/m². However, the domain walls they worked with were not created at a bend².

2.5 Procedure

First, the domain wall was initialized at the bend using the magnetic field ramping as described earlier. Current pulses were then sent to move the domain wall into part A of the wire.

In order to drive CIDWM, a series of current pulses were sent from a Tektronix 3102 function generator. These pulses were varied in a range between 0.1 and 3 s. This was done to identify the pulse duration necessary for depinning.

After each pulse, we measured the resistance between contacts 3 and 4 of the nanowire using the Keithley source-meter. The source current of 20 μ A used is sufficiently small to avoid breakdown or drive domain wall motion. Each measurement was taken in 0.2 s, after which another current pulse was sent across the wire. This was repeated was 20 pulses of increasing length.

3. Results

The measurements were attempted several times with several parameter changes. Three attempts are shown in Figures 3-5. Figure 3 shows the first attempt, which uses pulses varying from 0.1 to 1 μ s, and with a current density $j = 4.9 \times 10^{11}$ A/m², 1.0×10^{11} A/m² above j_t . The resistance of the sample was 94.950 +/- .012 Ω . Using $\Delta R_{DW} \geq 0.077\%$ we expect the drop in resistance to be at least .073 Ω . However, the difference between the maximum and minimum values of the resistance is only .014 Ω . This suggests that there was not ever a domain wall pulsed between the two contacts.

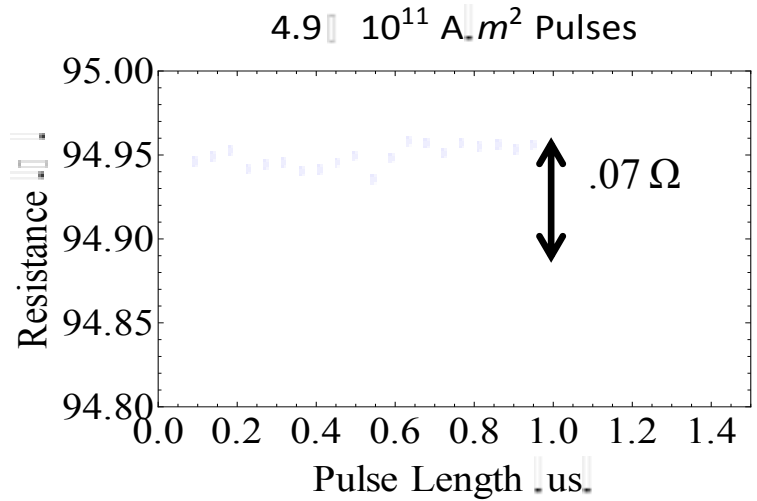


Figure 3: Resistance measurement of 500 nm wire after several pulses of 3.9×10^{11} A/m². The resistance varies by much less than the .07 Ω (represented by the arrow) suggested by the model, suggesting that no domain wall is present.

We also repeated these experiments at different values of the pulse current density. Figure 4 shows the results for a trial run using $j = 7.0 \times 10^{11}$ A/m². Pulse length was also varied; Figure 3 shows pulses varied between 1 and 3 μ s. However, none of the trials showed a drop in resistance as large as expected from calculations, or even larger than the uncertainty in measurement from the source meter. This suggests that the attempts to position a domain wall between the contacts were unsuccessful.

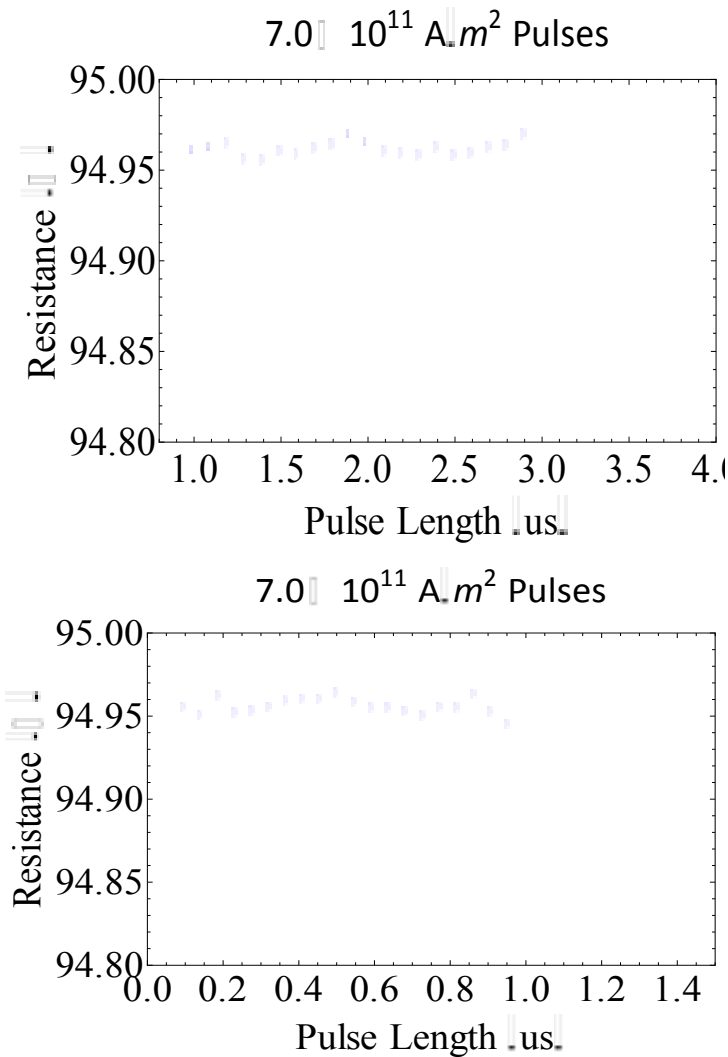


Figure 4-5: Resistance measurement of 500 nm wire at 7.0×10^{11} A/m². Figure 4 (bottom) shows pulses from 0.1 to 1.0 us, while Figure 5 (top) shows pulses varying from 1.0 to 2.5 us. No evidence of a domain wall is apparent in either.

4. Conclusion

In conclusion, a setup for low noise AMR measurements was successfully constructed. This allowed for electrical measurements of permalloy nanowires to search for domain walls. The attempts to prepare and locate these domain walls have so far been unsuccessful.

There are several potential reasons the domain wall was not successfully observed. One is that the domain wall was never formed in the first place. It is possible the magnetic moments in the wire did not relax as expected and a domain wall at the bend was not formed. This can be checked by observing the bend with a magnetic microscope after the magnetic ramping to search for a

wall. Another possibility is that the wall is formed, but that current pulses do not cause the wall to propagate as expected around the bend due to bend-induced changes in the wall geometry. Finally, it is possible that the AMR signal due to the domain wall is not actually as large as calculated making the domain wall signal unobservable relative to electrical noise. Using an amplifier or signal averaging could address this issue.

Despite initial lack of success, there are many ways to improve or alter the experiment that could make it work. Further studies with the microscope or improved models could suggest means of improvement that would make electrical measurement feasible.

5. Acknowledgements

I would first and foremost like to thank the Fuchs group for welcoming me this summer, and in particular thank Professor Greg Fuchs for providing an interesting and rewarding project, Jason Bartell and Darryl Ngai for their guidance and insights, and Austin Moehle for helping me construct the setup. I would also like to thank the National Science Foundation for their generosity. Lastly I would like to thank Cornell University and the Cornell Center for Materials Science for allowing me to work on this project and utilize their excellent facilities.

References

1. Beach, G.s.d., M. Tsoi, and J.I. Erskine. "Current-induced Domain Wall Motion." *Journal of Magnetism and Magnetic Materials* 320.7 (2008): 1272-281.
2. Yang, Shuqiang, and J. Erskine. "Spin-transfer-torque-driven Domain-wall Dynamics in Permalloy Nanowires." *Physical Review B* 75.22 (2007): n. pag.
3. Haazen, P. P. J., E. Murè, J. H. Franken, R. Lavrijsen, H. J. M. Swagten, and B. Koopmans. "Domain Wall Depinning Governed by the Spin Hall effect." *Nature Materials* 12.4 (2013): 299-303.
4. Pushp, Aakash, Timothy Phung, Charles Rettner, Brian P. Hughes, See-Hun Yang, Luc Thomas, and Stuart S. P. Parkin.

"Domain Wall Trajectory Determined by Its Fractional Topological Edge Defects." *Nature Physics* 9.8 (2013): 505-11.

5. Guimarães, Alberto Passos. *Principles of Nanomagnetism*. Heidelberg: Springer, 2009. 160.